Thermal Simulation of In-Space Additive Manufacturing

MSc. Thesis

Ulf Torsten Kemmsies



Delft University of Technology

TU Delft

This page is intentionally left blank.

Thermal Simulation of In-Space Additive Manufacturing

by

Ulf Torsten Kemmsies

to obtain the degree of Master of Science
at the Delft University of Technology,
to be defended publicly on Wednesday April 2, 2025 at 14:00.

Student number:	4794281	
Project duration:	June 1, 2024 – April 2, 2025	
Thesis committee:	Prof. dr. A. Cervone,	TU Delft, supervisor
	Dr. ir. M. Hermans,	TU Delft
	Dr. W. Ya,	RAMLAB

Cover: The Space Welder by Sergei Borisenko under CC BY-NC 2.0 (Modified)
Style: TU Delft Report Style, with modifications by Daan Zwaneveld

An electronic version of this thesis is available at `http://repository.tudelft.nl/`.

TU Delft

Preface

The story behind this thesis began almost exactly 10 years ago. I was struck by a lightning bolt of divine inspiration; an irresistible force commanding me to go to space whatever the cost. Honoring my calling, I moved across the Atlantic and began my journey in Delft, ten thousand kilometers away from all I knew before. The last 6 years have been transformative in uncountable ways, granting me knowledge and wisdom, but most of all humility. To struggle, fail, and persevere is the real lesson the gauntlet of elite education imparts. The central battle, however, is keeping the spark of youthful hubris and imagination alight in the face of the sobering realism one inevitably gains through experience.

It is this spark that led me to the topic of this thesis. Two and a half years ago, my passion for cislunar logistics, infrastructure, and manufacturing was teasing me from a corner of my mind. It was an unassuming conversation with my father that led me to taking a ridiculous question seriously: "Why can't we just 3D print massive structures in space?" It proved not to be so ridiculous after all. My mind was made, and nothing could budge the plan - this had to be investigated. I knew nothing about additive manufacturing at the time, but some say tenacity is the highest virtue.

My topic is unorthodox for the standards of this university. The near dozen professors I approached were wary of engaging in this intersection of fields, but I finally found the gracious Dr. Hermans at 3ME, who found it in him to take a student outside his faculty into his research group. I would like to thank José for helping me take my first steps in WAAM, and Remko for all of the help he offered in the lab over the last two years. Through the people at 3ME, I finally managed to meet the wonderful team at RAMLAB. They graciously took me in as an intern and taught me more about welding than I ever thought I could handle. I would like to thank everyone there, Johann, Remco, Aditiya, and Vincent, for their endless patience for my ignorance, and for giving me the freedom to pursue niche topics within their busy schedule. Most of all, I would like to thank Dr. Wei Ya for being possibly the best boss and mentor I will ever have. The man is a paragon of zen and a walking encyclopedia.

Shortly after, Dr. Cervone agreed to supervise me despite my then nebulous understanding of the problem. His courage to step outside his expertise was admirable, and I would like to thank him for taking a chance on me and keeping me on track to finish before my 30th birthday.

As far as I know, this is the first ever publication specifically performing macro-scale thermal modelling of metal additive manufacturing in orbit. This work is far from the scope I had initially dreamt up, but it is a small step in the right direction which I hope others can build on. Being at the edge is both terrifying and exhilarating, and I would never have survived this ordeal without the support of the those dearest to me. My friends - Silvio, Antonio, Neil, Anibal, Nathan, Bo, Jaap, Roman and Yessin, (and you who are reading this, you know who you are) - you kept me hopeful. My family - Liv, Björn, Dad, Ma, and Kurt, Geertrui, Tijs, and Iris - you kept me sane. And finally, my perennially patient, loving, and encouraging girlfriend Aster - who saw every late night, every weekend, and every holiday I sacrificed - you kept me alive.

Ulf Torsten Kemmsies
Delft, March 2025

Abstract

This thesis examines the thermal distribution and material behavior in in-space additive manufacturing (ISAM) using metal directed energy deposition (DED), addressing challenges of the orbital environment, including microgravity and vacuum. Experimental studies with a Scandium-modified Al-5183 alloy, conducted via Wire Are Additive Manufacturing, validated heat transfer coefficients and simulated ISAM thermal profiles. A finite element model, developed in Ansys Mechanical and calibrated with experimental data, accurately predicted overall thermal histories despite underestimating melt pool temperatures. Applied to orbital conditions, the model showed environmental healing effects were minimal for small components but significant for larger structures, supporting ISAM's potential for space infrastructure. Material analysis revealed enhanced mechanical properties due to Scandium addition, with refined grains and Al_3Sc precipitates. Integrating experiments, simulations, and characterization, this work advances ISAM thermal modeling, offering insights for future refinements in simulation accuracy and orbital testing.

Summary

This thesis investigated the thermal distribution and material behavior of in-space additive manufacturing (ISAM) processes through experimental and computational methods, with an emphasis on metal directed energy deposition (DED) techniques. The work explored the challenges posed by the unique thermal environment in orbit—such as microgravity, vacuum, and extreme temperature variations—and proposed methodologies to extend terrestrial manufacturing approaches to space applications.

The literature review covered the fundamental principles of additive manufacturing and DED processes, detailing the effects of different heat transfer mechanisms (conduction, convection, and radiation) under both Earth-based and orbital conditions. It identified key knowledge gaps in current models, particularly in capturing the intricate melt pool dynamics and their influence on microstructural evolution.

An Al-5183 alloy with 0.3% Scandium was systematically characterized for use in additive manufacturing in partnership with RAMLAB, a leading metal additive manufacturing research facility in the Netherlands. Wire Arc Additive Manufacturing (WAAM) was used in combination with DC^+ Panasonic Active Wire (AW-P) to perform two separate weld experiments with this alloy. The first validated convective heat coefficient boundary conditions for use in further modeling. The second used baseplate pre-heating to create high-temperature conditions with the objective of approximating the thermal profile during an ISAM deposition process.

A simplified thermal model was developed for a scaled-down space habitat module, simplified as a hollow thin-walled cylinder. The model was developed using Ansys Mechanical, which employed finite element analysis (FEA) to simulate the transient thermal behavior during a DED process. The model incorporated convective and radiative boundary conditions and was calibrated against experimental data obtained from the two weld experiments. Although the predicted melt pool temperatures were lower than expected, the model accurately replicated the overall thermal history of thermocouple measurements with mean errors on the order of $5°C$. The model was unable to accurately predict melt pool dynamics but was able to predict the overall thermal history of the workpiece.

This model was then applied with boundary conditions simulating the conditions in free-flying orbital vacuum, including vacuum and environmental heating from solar, albedo, and Earth IR flux. Three orbital heating cases were developed as boundary conditions for the ISAM simulation, and the model was used to predict the thermal history of the workpiece under each case. The results showed that the effect of environmental heating in orbit was negligible for small components but became significant for larger components. The stable thermal profiles predicted by the model demonstrated the feasibility of ISAM for large-scale space structures. The model also underestimated melt pool temperatures for ISAM conditions and should thus not be used for microstructural predictions.

Analysis of the deposited structures was performed to provide detailed material characterization (chemical composition, tensile strength, hardness, microstructural analysis via optical and scanning electron microscopy). The formation of desirable microstructural features, such as refined grains and the presence of Al_3Sc precipitates, was confirmed. Hardness and yield tests showed improved mechanical properties compared to experiments using similar deposition processes with the base alloy due to the addition of Scandium.

In conclusion, the integrated approach — combining thermal simulations, experimental validation, and material characterization — provided an initial foundation for advancing thermal modeling of ISAM. Limitations regarding computational efficiency and experimental replication of orbital conditions were acknowledged. Recommendations for future work included refining simulation fidelity, exploring alternative processes such as Electron Beam Welding and Laser Wire Directed Energy Deposition, applying testing conditions closer to those in orbit, and potential simplifications for modeling larger structures.

Contents

Preface i

Abstract ii

Summary iii

Nomenclature vi

1 Introduction 1
1.1 Background and Motivation . . . 1

2 Literature Review 3
2.1 Additive Manufacturing Overview . . . 3
2.1.1 Basic Concepts . . . 3
2.1.2 Metal Additive Manufacturing . . . 3
2.2 Wire Arc Additive Manufacturing . . . 7
2.2.1 WAAM Basic Concepts . . . 7
2.2.2 GMAW Based WAAM . . . 7
2.2.3 Aluminum deposition using WAAM . . . 9
2.3 Wire DED Physics . . . 9
2.3.1 Input Power, Heat Input, Travel Speed . . . 9
2.3.2 Melt Pool, Heat Affected Zone, and Weld Geometry . . . 10
2.3.3 Cooling Rate . . . 11
2.4 In-Space Additive Manufacturing . . . 13
2.4.1 ISAM Previous Research . . . 13
2.4.2 Structures of Interest . . . 14
2.4.3 Space Environment . . . 15
2.5 Thermal Simulation . . . 16
2.5.1 DED Modeling State of the Art . . . 16
2.5.2 ISAM Modeling State of the Art . . . 16
2.6 Research Objectives . . . 19
2.6.1 Research Plan and Investigation Workflow . . . 20
2.6.2 Thesis Structure . . . 20

3 Modeling and Simulation 21
3.1 Basic Simulation Tools and Concepts . . . 21
3.1.1 Simulation Package . . . 21
3.1.2 ANSYS Concepts . . . 21
3.2 Geometric Model and Mesh . . . 22
3.2.1 Structural Design . . . 22
3.2.2 Model Geometry and Dimensions . . . 24
3.2.3 Mesh Techniques and Size . . . 26
3.3 Thermal Modeling of ISAM . . . 27
3.3.1 Orbital Heat Inputs . . . 28
3.3.2 Thermal Modeling Physics and Equations . . . 37
3.3.3 Boundary Conditions and Assumptions . . . 38
3.3.4 Full-Scale Space Habitat Model . . . 42
3.4 Thermal Model Summary . . . 43
3.4.1 Implementation of the Model . . . 44
3.4.2 Capabilities and Usage . . . 44
3.4.3 Efficiency and Validation . . . 44

4 Material and Experiments **46**
4.1 Feedstock and Experimental Setup . . . 46
4.1.1 Material Properties . . . 46
4.1.2 Experimental Hardware . . . 47
4.1.3 Weldability, AM Feasibility, and Parameter Optimization Tests . . . 48
4.2 Model Validation Tests . . . 50
4.2.1 Toolpath Generation . . . 50
4.2.2 Convective Heat Transfer Coefficient Validation . . . 51
4.2.3 Large Cylinder Model Validation Test . . . 53
4.3 Material Characterization . . . 56
4.3.1 Metallurgical Analysis Equipment . . . 56
4.3.2 Etching Techniques . . . 56
4.3.3 Mechanical Testing . . . 56
4.3.4 Test Sample Design . . . 57

5 Results and Discussion **58**
5.1 Convective Heat Transfer Coefficient Validation . . . 58
5.2 Earth Conditions Model Validation . . . 60
5.3 Microstructure Results . . . 65
5.3.1 Microstructure for the Material . . . 65
5.3.2 Scanning Electron Microscopy (SEM) Results . . . 69
5.3.3 Hardness Results . . . 71
5.4 Mechanical Test Results . . . 72
5.5 Orbital Conditions Simulation Results . . . 75
5.5.1 Full-Scale Space Habitat Simulation . . . 79
5.6 Results Summary . . . 84

6 Conclusion and Recommendations **86**
6.1 Limitations . . . 87
6.2 Future Work . . . 88

A APDL Source Code **95**

B Orbital Heat Load Diagrams **96**

C Simulation Results **98**
C.1 Orbital Simulation Results . . . 98
C.1.1 Shielded Case . . . 98
C.1.2 Hot Case . . . 101
C.1.3 Cold Case . . . 103
C.2 Large Lab Simulation Results . . . 106

Nomenclature

Abbreviations

Abbreviation	Definition
AC	Alternating Current
AM	Additive Manufacturing
APDL	Ansys Parametric Design Language
AW-P	Panasonic Active Wire
ASTM	American Society for Testing and Materials
CAD	Computer-Aided Design
DC	Direct Current
DED	Directed Energy Deposition
EBF3	Electron Beam Freeform Fabrication
EM	Electromagnetic
ESA	European Space Agency
FEA	Finite Element Analysis
GCR	Galactic Cosmic Radiation
GMAW	Gas Metal Arc Welding
HPC	High-Performance Computing
ISA	International Standard Atmosphere
ISAM	In-Space Additive Manufacturing
ISM	In-Space Manufacturing
LEO	Low Earth Orbit
LWDED	Laser Wire Directed Energy Deposition
MAE	Mean Absolute Error
MEX	Material Extrusion
MJT	Material Jetting
MMOD	Micrometeoroid and Orbital Debris
NASA	National Aeronautics and Space Administration
OSAM	On-orbit Servicing, Assembly, and Manufacturing
PBF	Powder Bed Fusion
PAW	Plasma Arc Welding
SDAS	Secondary Dendritic Average Spacing
SEM	Scanning Electron Microscopy
S-AWP	Super Active Wire Feed Process
SPE	Solar Particle Events
SSP	Space-based Solar Power
TIG	Tungsten Inert Gas
TRL	Technology Readiness Level
WAAM	Wire Arc Additive Manufacturing

Symbols

Symbol	Definition	Unit
A	Cross-sectional area of the process	[mm^2]
a	Earth's albedo	[-]
a_{eff}	Effective area	[m^2]
d	Distance	[m]
d_p	Diameter of the projectile	[cm]
DT	Time of each load step	[s]
E	Heat input	[J/mm]
$F_{i-\text{Earth}}$	View factor between the component and the Earth	[-]
$F_{i-\text{Sun}}$	View factor between the component and the Sun	[-]
GL_{12}	Conductive coupling between two nodes	[-]
g	Acceleration due to gravity	[m/s^2]
h	Height	[m]
h_c	Convective heat transfer coefficient	[W/m^2K]
HB	Brinell hardness of the shield material	[BN]
I	Welding current	[A]
K	Effective thermal efficiency	[-]
L	Distance along which heat is being transferred	[mm]
m	Mass	[kg]
n	Number of cycles	[-]
P_d	Power density	[W/mm^2]
P_∞	Pressure exerted by the projectile upon impact	[Pa]
P_{in}	Input power	[W]
q	Heat transfer rate	[W]
r	Radius	[m]
$r_{A/P}$	Distance between the Earth and Sun at aphelion and perihelion	[AU]
SC	Solar Constant	[W/m^2]
s	Distance	[m]
t	Time	[s]
T	Temperature	[K]
U	Welding voltage	[V]
V_{impact}	Impact velocity	[km/s]
v	Travel speed	[mm/s]
w	Width	[m]
x	Variable	[unit]
α	Absorptivity	[-]
β	Beta angle	[degrees]
ϵ	Emissivity	[-]
$\varepsilon_{obliquity}$	Obliquity of the ecliptic	[degrees]
Γ	Ecliptic True Solar Longitude	[degrees]
ϕ	Angle at which the Earth is viewed from the satellite	[degrees]
ρ	Density	[kg/m^3]
$\rho_{projectile}$	Density of the projectile	[g/cm^3]
σ	Stefan-Boltzmann constant	[W/m^2K^4]
σ_{stress}	Stress	[Pa]
σ_θ	Hoop stress	[Pa]
σ_r	Radial stress	[Pa]
τ	Thickness	[mm]
θ_{impact}	Angle of impact	[degrees]
θ_{toe}	Toe angle	[degrees]
θ_{true}	True anomaly	[degrees]
θ_{entry}	Angle of entry	[degrees]

Symbol	Definition	Unit
θ_{exit}	Angle of exit	[degrees]
ξ	Density ratio coefficient	[-]

1 Introduction

Space exploration and infrastructure development face significant manufacturing challenges, as traditional Earth-based manufacturing and launch methods impose severe limitations on the size, cost, and complexity of space structures. In-space manufacturing (ISM), particularly in-space additive manufacturing (ISAM), offers potential solutions to these constraints by enabling direct fabrication in orbit, despite the unique challenges presented by the space environment, including microgravity effects, vacuum conditions, and extreme thermal variations. This thesis investigates the thermal dynamics and material behavior of metal additive manufacturing processes in orbital conditions, aiming to enhance understanding of ISAM processes and support their implementation in future space missions.

1.1. Background and Motivation

The concept of in-space manufacturing has gained significant traction in recent years, driven by the increasing demand for sustainable and cost-effective solutions for space exploration [1]. Traditional approaches to space infrastructure rely heavily on pre-fabricated components that are launched from Earth, a method that is both costly and limited by the constraints of launch vehicles. As we look to establish a permanent human presence in space [2], the need for a more sustainable, cost-effective and adaptable manufacturing technique becomes paramount.

In-space additive manufacturing offers a compelling alternative to achieve these goals. By enabling the production of components directly in orbit, ISAM can reduce the reliance on Earth-based manufacturing and launch capabilities. This is particularly relevant for the construction of large-scale structures, such as space habitats, solar power satellites, and orbital fuel depots, which are difficult or impossible to launch in their entirety from Earth. [3]

While extensive research [4, 5] exists on metal additive manufacturing processes for terrestrial applications, there is a notable absence of comprehensive thermal modeling studies for larger structures, particularly in orbital conditions [6]. This knowledge gap is critical, as thermal behavior significantly influences material properties and structural integrity of printed components. The unique thermal environment of space, characterized by extreme temperature cycles and limited heat dissipation pathways, presents unprecedented challenges that remain largely unexplored in the context of large-scale manufacturing.

The motivation for this research stems from two primary factors. First, the success of ISAM hinges on our ability to understand and control the unique conditions of the space environment. Microgravity, vacuum, and extreme thermal variations all play a critical role in the behavior of materials and the performance of manufacturing processes. Second, future mission designers require both a well-defined thermal design space for ISAM-printed components and robust modeling tools to conduct their own thermal analyses. This research aims to address these needs by developing and validating thermal modeling methodologies specifically for orbital manufacturing conditions.

Furthermore, the potential applications of ISAM extend beyond the construction of space infrastructure. The ability to manufacture components in space could enable on-demand repairs and maintenance, reducing the need for costly and risky extravehicular activities. This capability is particularly important for long-duration missions, where the ability to quickly and efficiently address mechanical failures could be the difference between mission success and failure.

All experimental work herein was conducted at RAMLAB, a company focused on Wire Arc Additive Manufacturing (WAAM), due to their long-standing expertise in the field of metal additive manufacturing

and close relationship to TU Delft. Thus, the process of interest in this work corresponds to their specialization.

2
Literature Review

This chapter presents a comprehensive review of the current state of knowledge regarding In-Space Additive Manufacturing (ISAM), with particular focus on Wire Arc Additive Manufacturing (WAAM) and its thermal aspects. The review begins with fundamental concepts of additive manufacturing, progresses through metal-specific processes, and examines the physics of wire-based Directed Energy Deposition (DED). Special attention is given to the space environment's unique challenges and their effects on manufacturing processes. The chapter concludes by identifying key knowledge gaps in the literature and formulating the research questions that guide this thesis.

2.1. Additive Manufacturing Overview

2.1.1. Basic Concepts

Additive Manufacturing (AM) is defined by the ISO/ASTM 52900 standard as a process that joins materials to create parts from 3D model data, typically in a layer-by-layer fashion. While most AM systems utilize 3D Cartesian motion architectures, other configurations like robotic arms, delta, and polar systems are also employed.

The main steps in an AM process are [6]:

- **3D model generation**: CAD models are converted to .stl/.amf files and processed by slicer software, which generates machine-readable commands such as G-code. The slicer specifies parameters including layer thickness, part orientation, location, scaling, and support structures.
- **Build preparation**: This step involves setting process parameters and physical setup, which includes machine cleaning, feedstock loading, calibration, and build settings.
- **Part building**: This is an automated, layer-based manufacturing process; however, manual supervision remains common despite advancements in process monitoring.
- **Post-processing (optional)**: This phase ranges from simple cleaning to complex treatments, such as heat treatments and CNC machining, which vary according to AM technology and part requirements.
- **Quality and analytics**: This encompasses both destructive methods (tensile, flexural, compression testing) and non-destructive methods (visual inspection, microscopy, structured light scanning, computed tomography).

2.1.2. Metal Additive Manufacturing

Metal AM encompasses several distinct process categories, as illustrated in Figure 2.1, which shows the nine main metal AM processes currently in use:

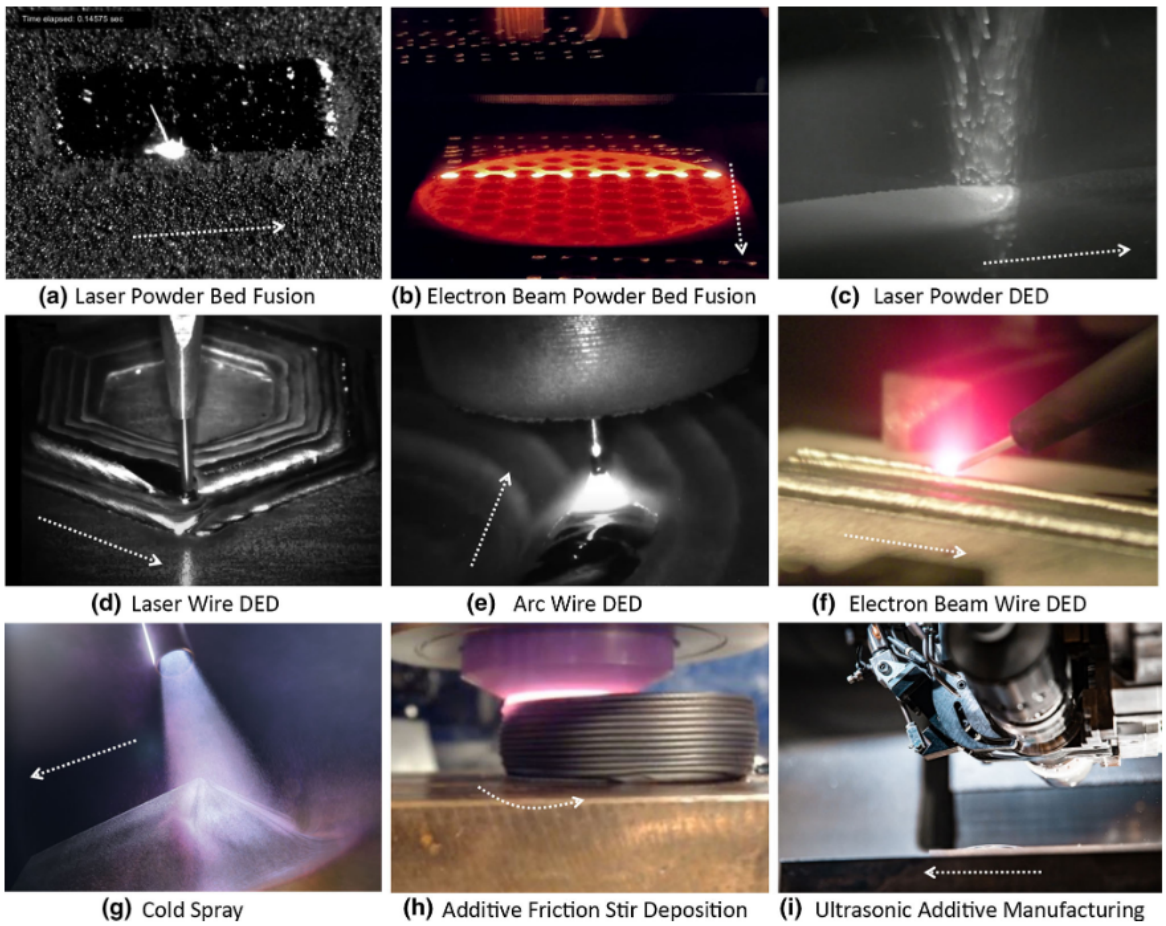


Figure 2.1: The nine main AM processes for metal [4]

- **Powder Bed Fusion (PBF)**: Uses a bed of powdered material selectively melted by laser or electron beam. Includes processes like Laser Powder Bed Fusion (LPBF) and Electron Beam Powder Bed Fusion (EB-PBF) [6].
- **Directed Energy Deposition (DED)**: Employs a high-energy heat source to create a melt pool for feedstock deposition. Includes variants like Laser Wire DED (LWDED), Electron Beam DED (EBF3), and Wire Arc Additive Manufacturing (WAAM) [7].
- **Other Processes**: Include Cold Spray (CS), Additive Friction Stir Deposition (AFS-D), and Ultrasonic Additive Manufacturing (UAM) [4].

The focus of this research on wire DED is due to several factors. The external constraint is the AM equipment available for research, but there are other reasons for choosing DED over other methods for ISAM.

Build volume in additive manufacturing is influenced by build speed, economic factors, and waste reduction, even with powder recycling. In L-PBF processes, the feedstock material must fill the build box to the highest point printed, surpassing the part's total volume. In contrast, solid-state and DED processes deposit material as needed during construction and are integrated with robotic or gantry systems, allowing for larger build volumes. As shown in Figure 2.2, the build volume of DED processes is not limited by the size of the build box, enabling the construction of large parts or multiple parts simultaneously [4]. For large space structures at several meter scales, DED processes are more suitable because of the lack of build volume constraints.

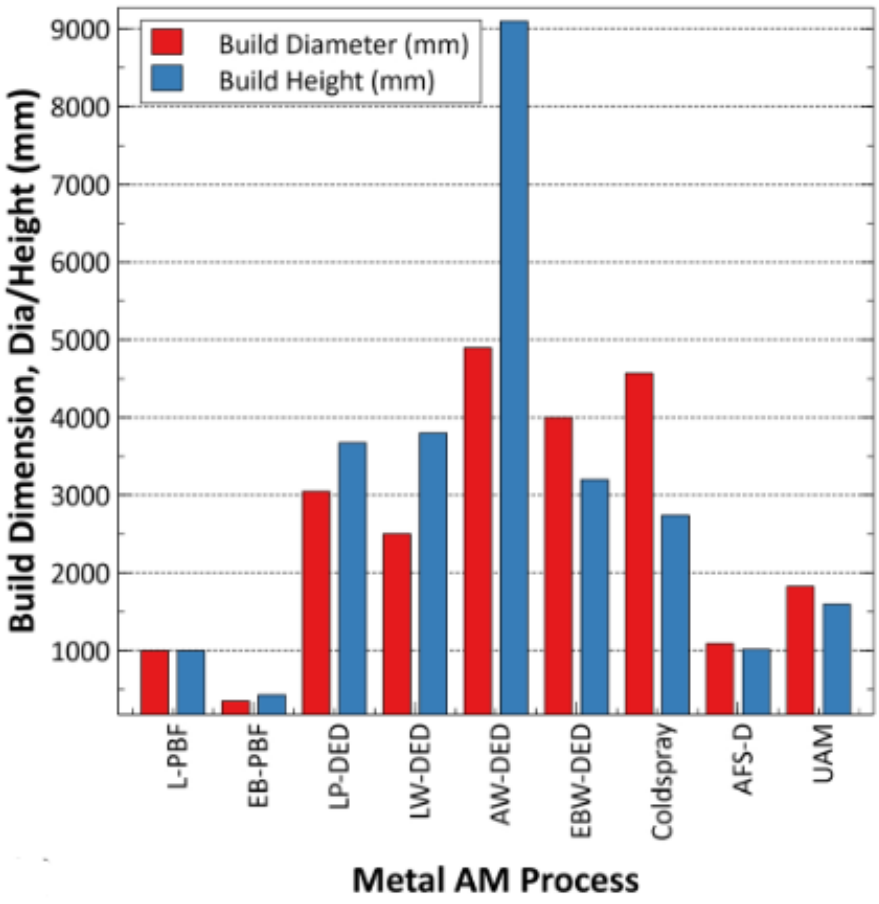


Figure 2.2: The commercially available build volumes for several metal AM processes [4]

Deposition rate is an important parameter for in-space manufacturing, specially if the total printed volume of the structure is large. This rate is roughly inversely correlated with **feature resolution**, as shown in Figure 2.3. DED processes like LP-DED and LWDED can utilize different spot sizes, while AW-DED can increase wire feedstock diameter to boost deposition rate, though this reduces feature resolution. Print speed is crucial for reducing manufacturing lead times but must be balanced against potential metallurgical consequences.

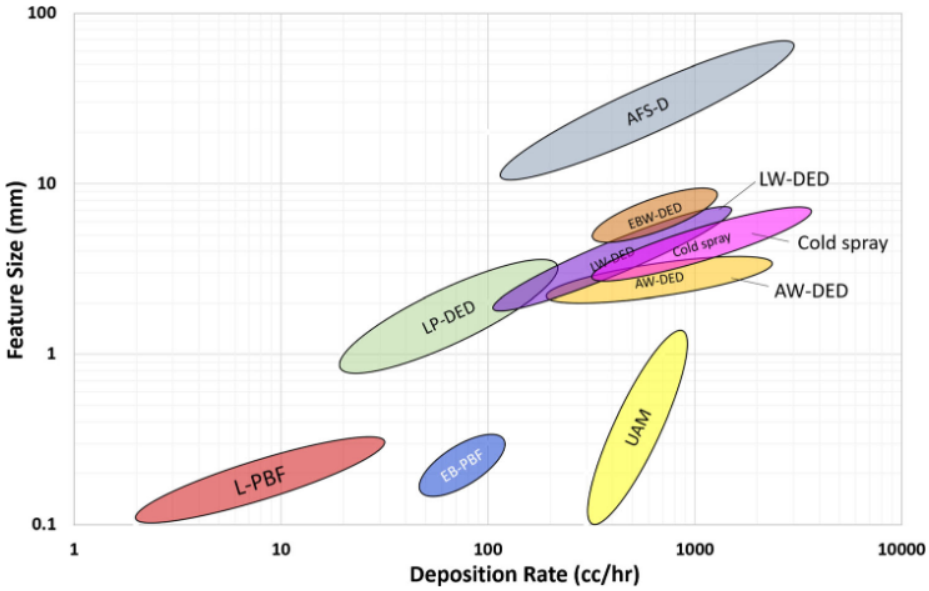


Figure 2.3: The deposition rates and feature resolution for several metal AM processes [4]

Another consideration is **post-processing requirements**, which tend to increase with decreasing feature resolution and increasing deposition rate, as shown in Figure 2.4. DED processes often require machining as a final step to achieve the desired surface finish and dimensional accuracy, which can be time-consuming and costly. However, the ability to deposit material at high rates can offset these costs by reducing overall manufacturing time.

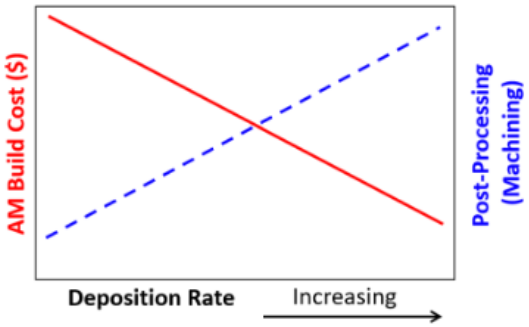


Figure 2.4: The typical relationship between deposition rate, build cost, and post-processing requirements [4]

L-PBF methods are the most mature in the aerospace industry [4], but are intrinsically unsuitable for ISAM because of microgravity conditions due to the need for keeping a stable powder bed, which is usually achieved through gravitational forces. However, some research has proposed and successfully tested L-PBF in microgravity using a patented "gas flow-assisted powder deposition" method [8] on parabolic flight tests, which only simulate microgravity for short durations.

Even with proven viability, powder-based systems face numerous challenges in reduced gravity environments. These include a disproportionately large system footprint relative to the build volume, significant power consumption, and metallic powders used in these systems pose toxicity and combustibility hazards, which are pertinent in closed manned environments like the ISS. [6].

DED processes, particularly wire-feedstock variants like WAAM, EBF3, and LWDED, are more suitable in microgravity conditions due to the active control of the feedstock feeding independent of gravity. The detachment of molten feedstock droplets in microgravity presents its own challenges, but has

experimentally been found to be feasible [9, 10], mostly due to auxiliary forces acting on the droplets, like the electric field generated by the arc in WAAM [11].

The ASTM 3413 also lists several additional benefits of DED processes: often better mechanical properties than L-PBF-printed parts. These include locally adjustable part characteristics, flexibility in printing local features, repairing, or coating existing parts, higher design freedom due to six-DOF robotic arms, non-horizontal surfaces can be printed, and the ability to print on large, immovable parts. [12]

The three wire-based DED methods, LWDED, EBF3, and WAAM, are currently the most promising for in-space manufacturing, and the three will be compared to understand their similarities.

EBF3 uses a focused electron beam in a vacuum to create and maintain a molten pool into which metal wire feedstock is introduced. Electrons are accelerated by strong magnetic fields in an electron gun. Magnetic lenses are then used to focus the beam into a narrow cone, increasing the density of the power transferred to the workpiece surface [13]. This technique has been demonstrated on aluminum and titanium alloys for aerospace applications, with plans to include nickel and ferrous-based alloys. Deposits from 2219 aluminum show varied grain morphologies based on deposition parameters and exhibit excellent tensile properties comparable to wrought plate products after heat treatment. [14]

Laser Wire Directed Energy Deposition (LWDED) involves the use of a high-power laser to melt metal wire as it is being deposited onto a substrate. The laser serves as a focused thermal energy source that selectively melts the wire feedstock, layer by layer, to build up the desired shape. LWDED is particularly advantageous for repairing components, fabricating large structures, and adding features to existing parts due to its ability to produce strong, accurate, and durable objects. [4]

2.2. Wire Arc Additive Manufacturing

Recent literature highlights the increasing demand for aluminum alloys produced by WAAM, particularly in industries such as automotive, marine, and energy sectors. The WAAM process is favored for its low investment cost, high deposition rates, and ability to create complex parts. [15]

2.2.1. WAAM Basic Concepts

Wire-Arc Additive Manufacturing (WAAM) employs direct feeding processes with electric sources, motion systems, and wire-based feedstock. Three primary heat sources are utilized in WAAM [5]:

- **Gas Metal Arc Welding (GMAW)**: This method uses a continuous wire feed as an electrode and an inert gas to shield the weld pool from contamination. GMAW is known for its high deposition rates and versatility, making it suitable for a wide range of materials, including aluminum and steel.
- **Tungsten Inert Gas (TIG)**: In this process, a non-consumable tungsten electrode generates the arc, while a separate filler wire is fed into the weld pool. TIG welding provides excellent control over the heat input and is ideal for producing high-quality welds in thin materials, although it typically has lower deposition rates compared to GMAW.
- **Plasma Arc Welding (PAW)**: PAW utilizes a constricted arc between a tungsten electrode and the workpiece, creating a high-temperature plasma that melts the filler material. This method allows for precise control of the heat input and is particularly effective for welding thin sections and achieving high-quality surface finishes.

2.2.2. GMAW Based WAAM

GMAW is recognized as the most prevalent heat source utilized in WAAM due to its efficient direct-feeding spool system, which facilitates a continuous supply of wire feedstock. This method encompasses several subcategories, each with distinct characteristics and applications [5]:

- **Metal Active Gas (MAG)**: This variant employs an active shielding gas that reacts with the molten weld pool, enhancing the welding process and improving penetration.
- **Dual-shield**: This approach combines both active and inert gases, providing a versatile solution that can adapt to various materials and environmental conditions.

- **Metal Inert Gas (MIG)**: In this method, inert gases are used to protect the weld pool from atmospheric contamination, resulting in high-quality welds with minimal defects.

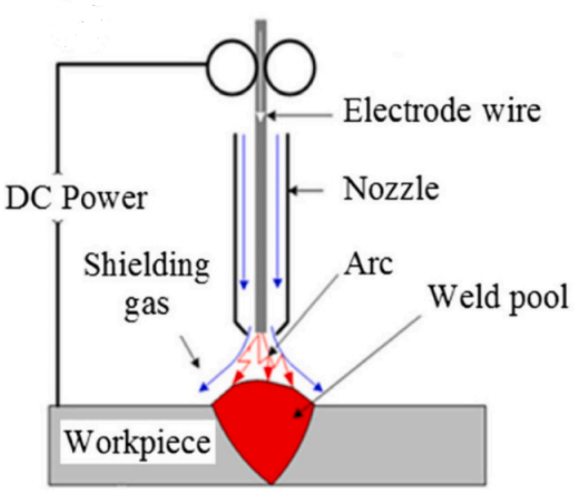


Figure 2.5: Schematic of the GMAW arc generation process [16]

The basic configuration of a GMAW system is illustrated in Figure 2.5, showing the key components including the wire feed mechanism, contact tip, and shielding gas delivery. All variants generate an electric arc between a consumable wire electrode and the workpiece. In MIG specifically, inert shielding gases like Argon or Helium are used, which do not actively react with the melt pool during welding [5].

The deposition of wire feedstock in WAAM occurs when the tip of the wire has reached its melting temperature due to the energy of the arc closed with the workpiece. The droplet forms at the tip of the wire, falls onto the partially melted substrate, and forms a temporary liquid bridge which closes the circuit and drops the voltage between the wire and workpiece that formed the arc initially. This process of droplet detachment, shown in Figure 2.6 occurs at a certain frequency, ranging from 25 to 300 Hz, increasing approximately logistically with arc powers between 1 and 6 kW [17].

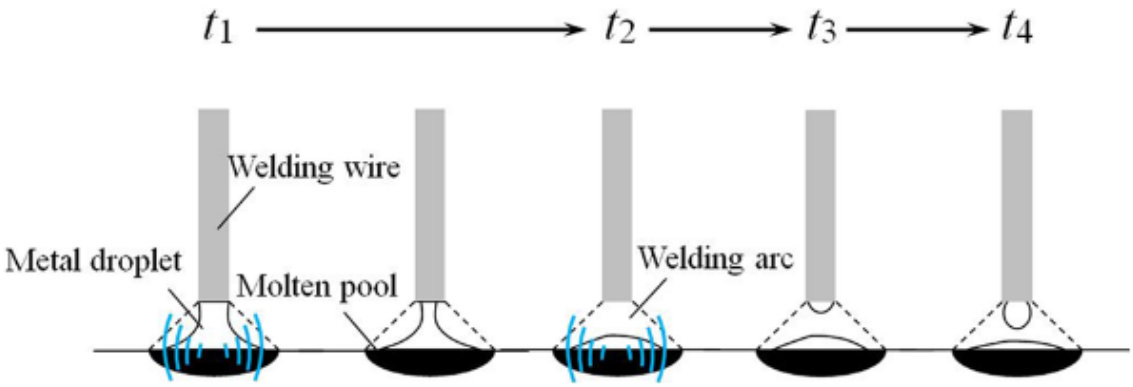


Figure 2.6: Schematic of droplet separation cycles for WAAM MIG short-circuit transfer mode [17]

However, droplet separation can also be influenced by active control of the distance between the wire tip and the workpiece, known as Contact Tip Workpiece Distance (CTWD). Fronius developed the Cold Metal Transfer (CMT) method, which thrusts the wire into the melt pool with a given waveform and frequency. This which controls the droplet detachment frequency, deposition rate, and required heat input (since less heat is needed to form a full droplet) [18]. The CMT method has been found to reduce

spatter, porosity, and oxidation, and increase deposition efficiency and weld quality [18]. Another method is the Active Wire Feed Process (AW-P) developed by Panasonic, which uses a wire feed pulses to control the droplet detachment frequency to reduce spatter by up to 96% for MIG welding [19]. The AW-P method has very little literature reported, but at the request of the partner company for this thesis, RAMLAB, it will be included in the experimental design.

2.2.3. Aluminum deposition using WAAM

Aluminum alloys, though weaker than titanium, are common in aerospace applications due to their favorable strength-to-weight ratio. Various aluminum alloys have been adapted for additive manufacturing, though they face challenges including poor elevated temperature capabilities, weld repair difficulties, and susceptibility to stress corrosion cracking [4].

The 2000-6000 series of aluminum alloys are particularly relevant for WAAM applications due to their high strength, corrosion resistance, and versatility. These series include [20]:

- **2000 Series**: Contains copper as the primary alloying element, notable for high strength and corrosion resistance. Common in aircraft structures and engine mounts (e.g., 2014, 2024, 2219). Research has shown that deposits from 2219 aluminum exhibit excellent tensile properties comparable to wrought plate products after heat treatment [14].
- **4000 Series**: Features silicon as the main alloying element, commonly used in welding filler materials and heat exchangers (e.g., 4043, 4145) [21].
- **5000 Series**: Incorporates magnesium as the primary alloying element, suitable for aircraft structures and engine mounts (e.g., 5050, 5083) [21].
- **6000 Series**: Combines magnesium and silicon, offering high strength, corrosion resistance, and weldability (e.g., 6061, 6063, 6082) [21].

Process control is particularly important when working with aluminum in WAAM. The control of droplet detachment and heat input is crucial for maintaining dimensional accuracy and preventing defects common in aluminum welding, such as porosity and oxidation. Methods such as Cold Metal Transfer (CMT) have shown effectiveness in reducing heat input and improving deposition quality for aluminum alloys [18].

From a process perspective, the use of aluminum in WAAM presents unique challenges and considerations. The high thermal conductivity of aluminum necessitates precise control of the heat input to avoid excessive distortion and ensure proper fusion between layers. Additionally, the susceptibility of aluminum alloys to hot cracking during the solidification process requires careful management of the cooling rates and interpass temperatures. [15]

Moreover, the selection of appropriate filler materials is critical, as the alloying elements can significantly influence the mechanical properties and microstructure of the final product. Filler materials in the wire are alloys added in the core of the feedstock to improve certain properties of the deposited material. The use of hybrid systems that combine WAAM with other processes, such as milling or surface treatments, has shown promise in mitigating defects and enhancing the overall performance of aluminum components. [15]

2.3. Wire DED Physics

WAAM is a viable process for in-space additive manufacturing, and understanding its process parameters and their relations to resulting material properties is essential.

2.3.1. Input Power, Heat Input, Travel Speed

For WAAM, the linear heat input E $[J/mm]$ is a function of the input power P_{in} $[W]$ and travel speed v $[mm/s]$. The input power is calculated using the current I $[A]$ and voltage U $[V]$ of the arc according to Equation 2.1, where the commonly accepted arc efficiency factor is 0.8 [22].

$$E = \frac{U \cdot I \cdot 0.8}{v} \tag{2.1}$$

The heat input for WAAM processes is typically in the range of 0.1-1 kJ/mm, with the most common values being 0.4-0.6 kJ/mm [23, 24, 25].

It has previously been found that welding speed inversely affects weld bead width, root width (the initial point of solidification), dendrite length, and dendritic spacing in the fusion zone. Dendrites are the elongated solidified material that form in the fusion zone, and their length and spacing are important for the mechanical properties of the part. Welding speed directly enhances tensile strength, ductility, hardness, and resistance to pitting corrosion. Conversely, increased heat input reduces tensile strength and enhances cracking during various welding processes [26]. Optimal mechanical properties in DED processes are significantly influenced by grain orientation and heat input, with higher heat inputs generally reducing mechanical properties due to increased grain size. While heat input is crucial, other factors such as process parameters, post-heat treatment, grain size, and pores also significantly impact mechanical properties, necessitating a comprehensive understanding of their correlations [22].

2.3.2. Melt Pool, Heat Affected Zone, and Weld Geometry

The melt pool is the region of the workpiece melted by the heat source in the immediate wake of the arc. The weld bead is the deposition of new feedstock on the current layer being processed. The weld bead has key parameters like width, height, the width/height ratio, cross-sectional area, as shown in Figure 2.7. The Heat Affected Zone (HAZ) is the region of the workpiece that has been heated by the heat source but not melted. The dimensions of the melt pool and weld bead have several effects on the quality of the final part, the thermal evolution of the deposition and cooling, and the mechanical properties of the part. [22]

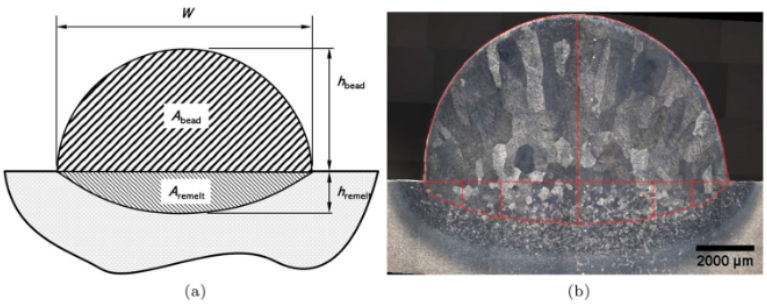


Figure 2.7: Weld bead and melt pool dimensions for a typical bead. [27] (a) Weld bead dimensions (b) Dimensions superimposed on a typical bead

Higher heat inputs result in larger melt pools, which can be varied by either changing input power or travel speeds. Higher wire feed rates will also increase melt pool sizes. The melt pool is particularly sensitive to instability and chemical interactions like oxidation and must thus be shielded for WAAM. A higher substrate temperature also increases the melt pool geometry and permanence before solidification. [22]

The cross-sectional area, length-to-depth ratio, and penetration depth are crucial for melt pool geometry control, since these parameters affect build quality and solidification morphology. The properties of the substrate and feedstock can also affect the melt pool due to differing melting temperatures and thermal conductivities.

The weld bead itself has key parameters like width, height, the width/height ratio, cross-sectional area, and toe angle θ, as shown in Figure 2.8. The toe angle is particularly important for the build strategy and stability, as it makes overlaps easier, while larger toe angles can also cause unwanted sloping of walls at the edges [28]. The spreading out of the weld bead is influenced by several factors, a chief one being the surface tension distribution in the melt pool. This can be affected by the thermal evolution of the pool (thus heat input), but also by the thermophysical properties of the feedstock like solid and liquid thermal conductivity, and emissivity of the deposited material. Another important factor is the deposition rate of the wire, since droplet radii decrease with increasing power and deposition rates [17], although independently increased wire feed rates will raise the deposited bead's cross-section. The type of shielding gas used will also influence the melt pool's cooling rate due to convective thermal

transport, since different gases have different convective constants, thermal conductivities, viscosities, and specific heats [11].

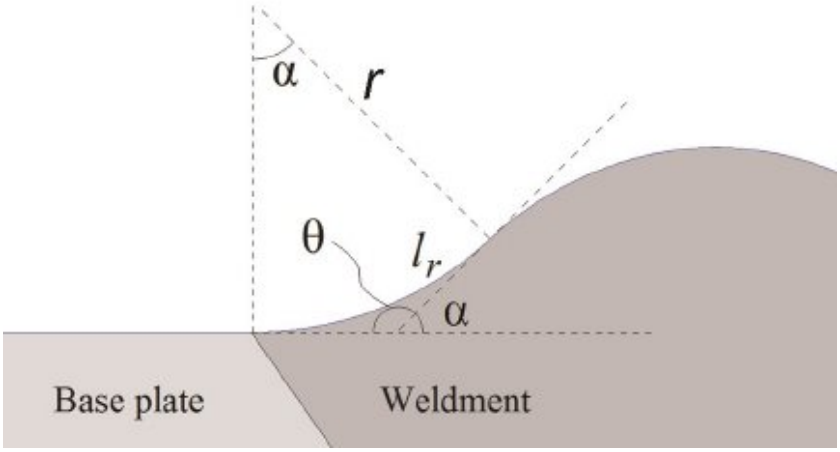


Figure 2.8: Diagram of the toe of a weld bead, showing the toe angle θ [28]

2.3.3. Cooling Rate

The cooling rate of a DED process is the rate at which the melt pool and weld bead cool down after the heat source has been removed. A supplementary definition is the time it takes the melt pool to cool from 800 to 300 °C, which has particular importance for the phase transformation of stainless steels [26]. The estimated cooling rates during solidification for WAAM is $10^1 - 10^3$ °C/s [29].

In WAAM, increases in the initially moderate cooling rate have been shown to alter the microstructure only moderately. Previous research has found that cooling rates are inversely proportional to heat input for DED processes, as shown in Figure 2.9, as are the hardness and grain size [26]. Distortions of the part have also been found to be reduced with slower cooling rates induced with preheat welding [30].

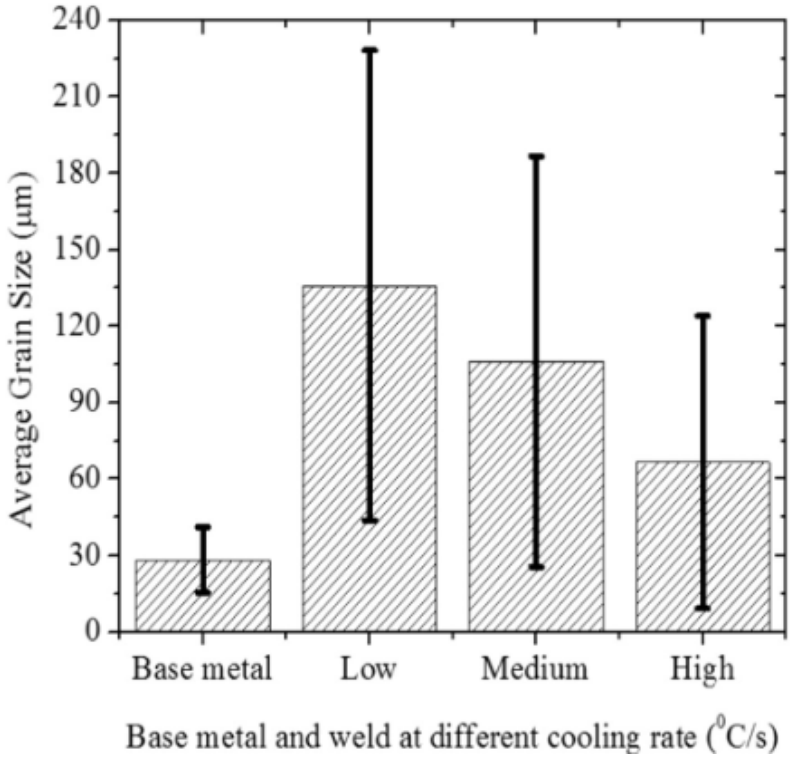


Figure 2.9: Experimentally found inverse relation between grain size and cooling rate for electron beam welding of AISI 304 stainless steel [26]

Cooling rates have also been found to affect the microstructure in specific ways, namely the prevalence of low-angle grain boundaries in stainless steels, due to increased thermal strain and dislocation density. The secondary dendritic average spacing (SDAS), shown in Figure 2.10, in stainless steels was also found to increase with heat input or decrease with cooling rate [26].

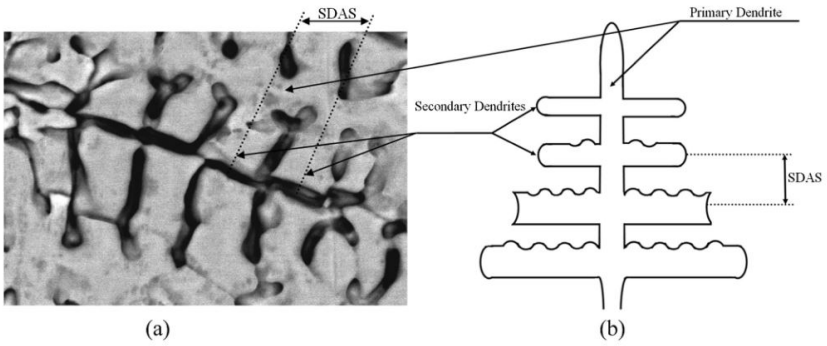
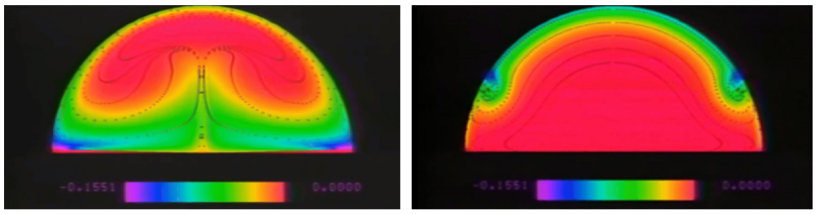


Figure 2.10: Secondary dendritic average spacing (SDAS) [26] (a) SEM image of dendrites in welded AISI 304 stainless steel (b) Graphical representation of primary and secondary dendrites

The cooling rate is intimately related to thermal diffusion in the fusion zone or melt pool, in part due to the greatly increased thermal conductivity of the liquefied metal, which at melting temperatures can be up to 5 to 20 times higher than in the solid phase[31].

The main mechanisms for heat transfer in the melt pool are conduction, convection, and radiation. For liquid flow, the main forces at play include the Marangoni, Lorentz, and buoyancy forces. The Marangoni effect is the flow of liquid due to surface tension gradients, which can be caused by temperature gradients in the melt pool. The Lorentz force is the force exerted on a moving charge in a magnetic field, which can be caused by the magnetic field of the arc. The buoyancy force is the force exerted on an object in

a fluid due to the difference in density between the object and the fluid, which can be caused by the temperature difference between the melt pool and the surrounding air [26]. Estimating heat transfer in microgravity is complicated by the lack of buoyancy forces, which can cause the Marangoni effect to dominate, as shown in Figure 2.11 [6]. However, even in normal gravity analyses of melt pool thermal transport, buoyancy convection has a significantly smaller impact than Marangoni convection [31].



(a) (b)

Figure 2.11: Marangoni convection in the melt pool [6] (a) Thermal convection in a droplet under gravity (b) Thermal convection in a droplet in microgravity

2.4. In-Space Additive Manufacturing

In-Space Additive Manufacturing (ISAM) is a subset of In-Space Manufacturing focusing on component and structure production using additive manufacturing techniques in orbit and on other celestial bodies. Current advancements face challenges related to quality, cost, and limited research platform access. Quality concerns include porosity, warping, delamination, mechanical properties, geometric accuracy, and repeatability [6].

2.4.1. ISAM Previous Research

Parabolic flight campaigns (PFCs) are commonly used but offer only short periods of microgravity and introduce hypergravity phases, making them inadequate for thorough statistical analysis [6]. The primary metal AM processes investigated in microgravity conditions are DED and PBF. Materials tested include aluminum alloys, alumina resin, regolith simulant, SS 316L, Ti-6Al-4V, and ULTEM 9085 [6].

DED technologies have demonstrated versatility in space applications. LWDED has successfully processed Lunar and Martian regolith simulants, while WAAM is being implemented through MIS's Vulcan for intravehicular ISM. Electron beam technologies, operating under vacuum conditions, show potential for external ISM applications. [6]

In 2007, PFCs were conducted to test the feasibility of EBF3 in microgravity (μg). The tests involved depositing aluminum wire onto aluminum substrates during the µg portions of flights. The results showed that EBF3 is feasible in µg, but precise control of the distance between the substrate and wire feeder is crucial. Deposits made in µg and 1g (ground) showed no visual differences, and microstructural analysis revealed similar columnar grains and heat-affected zones, with no porosity detected. The study confirmed that EBF3 can operate effectively in µg, with surface tension dominating the deposited geometry. [9]

Currently, two candidate processes have been identified by NASA MSFC for metal ISAM on the ISS by 2025: MIS's Vulcan, combining WAAM and CNC machining for aluminum, and Techshot Inc.'s FabLab, using FFF for titanium-polymer filaments requiring debinding and sintering [32]. Both systems must integrate subsystems within ISS EXPRESS Rack constraints. Vulcan includes machining and robotic automation but faces challenges with waste and thermal stresses, while FabLab faces challenges with nonuniform shrinkage during sintering and handling toxic binder substances.

ESA has contributed significantly, launching a stainless steel LWDED experiment to the ISS in February 2024. The system operates within a sealed nitrogen atmosphere box, with prints limited to four hours daily due to ISS noise regulations. The experiment, while still not fully reported, printed several dumbbell-shaped stainless steel samples, as shown in Figure 2.12[10].

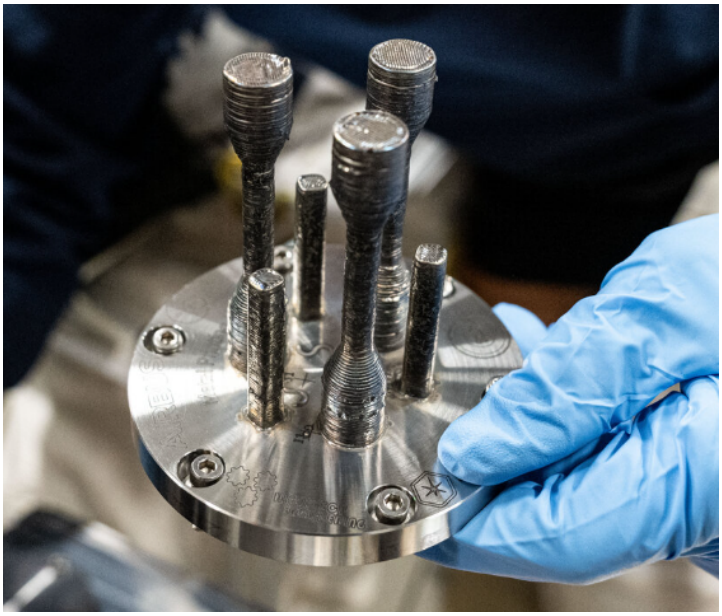


Figure 2.12: ESA's LWDED experiment on the ISS [10]

Gu and Li's computational fluid dynamic models studying microgravity effects on DED processing of 316L stainless steel wire revealed that: (1) microgravity leads to irregular deposition tracks due to surface tension dominance; (2) irregularities can be minimized by reducing wire volume per unit length; (3) material vaporization increases at lower pressures; and (4) reducing laser power or increasing scanning speed can prevent vaporization [33]. Xie et al. examined thermocapillary convection evolution (how melted metal flows due to changes in surface tension caused by temperature differences) in liquid bridges (the pools of molten metal that form as the wire melts and connects to the growing part) during laser wire DED of Ti-6Al-4V, finding that gravity significantly influences thermocapillary convection behavior [34].

In microgravity environments, the dynamics of welding and material processing are significantly altered due to the absence of buoyancy forces. This results in surface tension effects becoming more pronounced, leading to diffusion-dominated mass transfer that favors cellular growth over dendritic structures. The reduced convective mixing in such conditions contributes to slower cooling rates and promotes the formation of more ordered microstructures, while high segregation in welds is anticipated due to the dominance of diffusion. [35]

Heat transfer mechanisms in microgravity rely solely on conduction and radiation, which are less efficient than convection, resulting in prolonged cooling times and potential issues such as larger grain growth. Additionally, the behavior of thermocapillary flows is modified, with implications for fluid dynamics in the melt pool. The challenges posed by microgravity necessitate further research to understand the effects on material properties and processing techniques, particularly in the context of in-space additive manufacturing (ISAM). [35]

2.4.2. Structures of Interest

Large space structures manufactured in-orbit can be categorized by their primary expected benefits relative to traditional methods [36, 6]:

- Structurally Optimized Systems: Designed for orbital rather than launch loads, enabling mass reduction of up to 30% [3]
- Larger-than-Launcher Systems: Exceed payload fairing constraints while maintaining stowed volume efficiency
- Repairable Systems: Enable on-orbit maintenance, reducing redundancy requirements and extending operational lifespans

- On-Demand Manufactured Systems: Decrease logistics mass and resupply mission frequency, particularly crucial for deep space missions
- Recycling Systems: Utilize orbital debris as feedstock, estimated at 7.7 million kg as of 2018, representing potential value of $7.7 billion at $10,000/kg launch costs
- Accurately Tested Systems: Built and validated in actual space environment, eliminating launch-induced damage risks

Key architecture categories include, but are not limited to the following:

Space Solar Power: Large arrays provide significant spacecraft power, with current systems producing 10-20 kW at 60-178 W/kg and 10-40 kW/m3. Projects like SpiderFab and Archinaut aim to produce lightweight arrays, with potential for 300 kW systems through truss structure optimization [3].

Communications Platforms: Large antenna reflectors (>100m) enhance gain, sensitivity, and spatial resolution, enabling applications like continuous climate monitoring from geostationary orbit [37]. ISM offers nearly flat cost scaling with size compared to traditional methods [3].

Fuel Depots: Critical for cislunar refueling architectures, requiring complex pressure vessels and fluid transfer systems for cryogenic propellant storage and transfer in microgravity [38, 39].

In-Space Vehicles: Range from satellite to station scale, serving functions like refueling, de/re-orbiting, and OSAM operations. Critical structural components include main frames, propulsive systems, and large radiators [38, 40].

Space Stations: Historical designs emphasized truss structures [41], but modern commercial stations focus on pressurized modules. These modules are currently constrained by launch loads and fairing dimensions, making them ideal candidates for ISM optimization. Recent commercial developments by companies like Axiom Space, Vast, and Orbital Reef demonstrate increasing market interest in space station architectures [2].

This research will investigate the feasibility of manufacturing such pressurized vessels in-orbit, focusing on structural requirements and manufacturing processes that could enable larger, more efficient space station architectures while minimizing launch constraints.

2.4.3. Space Environment

The space environment presents unique challenges for metal AM processes. According to Naden et al. [35], microgravity significantly alters material processing:

- Surface tension effects dominate due to absent buoyancy forces
- Mass transfer is primarily diffusion-governed, promoting cellular over dendritic growth
- Reduced convective mixing leads to decreased growth rates and more ordered directional structures
- High segregation occurs in welds due to diffusion-dominated mass transfer
- Heat transfer relies solely on radiation and conduction, causing slower melt pool cooling

Environmental factors affecting ISAM include, but are not limited to the following:

Atomic Oxygen: Most abundant ion in LEO, created by UV radiation dissociating molecular oxygen. While highly reactive and damaging to polymers, metals remain largely unaffected due to protective oxide layer formation. NASA flight tests from the 1980s demonstrated no measurable weight loss in aluminum samples [42, 43].

Radiation: Comprises EM radiation, charged particles (protons, electrons, heavier ions), and neutrons, primarily from solar and galactic sources. In LEO, metals experience minimal ionization damage, with alterations in strength, ductility, and creep rate occurring only at doses exceeding LEO exposure [43]. However, non-ionizing damage from massive particles can cause lattice displacement and swelling. Metals exhibit reduced plasticity and increased hardness post-irradiation, with elastic moduli unaffected below neutron fluence of 10^{17} n/cm^2 [44].

Micrometeoroids and Orbital Debris: Micrometeoroids travel up to 60 km/s, while orbital debris averages 10 km/s. Impact severity varies with solar cycle, as increased solar activity raises atmospheric

drag on debris. While large debris can be tracked for avoidance, smaller impacts are unavoidable. A 1-cm object in LEO can penetrate 5-cm thick aluminum [42]. Protection typically relies on Whipple shields with multiple layers to disperse, fragment, and absorb debris.

Vacuum and Outgassing: Materials release trapped gases through three mechanisms: bulk desorption, surface desorption, and material evaporation. Outgassing rates depend on density, surface roughness, and volatility. While metals generally exhibit low outgassing rates, the effect cannot be mitigated through traditional pre-launch bake-out procedures for ISAM applications [42].

Thermal Environment: Heat sources in LEO include direct solar radiation, albedo heating from solar radiation reflected off of Earth, IR emissions from the Earth as a grey-body emitter, and any internal heat sources like heaters, welding processes, and electronics. The cosmic microwave background radiation in space is 2.73 K and acts as a heat sink. [42]

Spacecraft thermal balance depends on internal conduction, surface thermo-optical properties, and orbital position/orientation relative to heat sources and sinks.

2.5. Thermal Simulation

2.5.1. DED Modeling State of the Art

Thermal simulation of DED processes requires consideration of multiple physical phenomena across different scales. Heat transfer occurs through conduction, convection, and radiation, with the latter two being particularly significant in space environments [6, 35]. Material properties exhibit strong temperature dependencies, notably thermal conductivity and elastic modulus [45, 46, 47].

Four primary scales of physical phenomena are considered in DED simulation [48, 49]:

- Microscale: Focuses on microstructural changes, solidification, and phase transformations (nm to μ scale)
- Particle scale: Examines particle interactions and packing density (μm to mm scale)
- Mesoscale: Models heat transfers, fluid flow, and Marangoni effects (mm scale)
- Macroscale: Predicts thermal-mechanical behaviors and temperature distribution (mm to m scale)

Previous research has demonstrated that thermal cycling significantly impacts material performance [45, 50]. Aluminum alloys show fatigue life reductions of 25% at 150°C [50] and 44% at 225°C [51]. Thermal conductivity behavior varies by alloy composition, generally increasing with temperature until reaching a plateau [47, 45].

Three primary methods exist for tracking melt pool interfaces during simulation [48, 52]:

- Level Set Method: Effective for scenarios where surface tension effects are negligible [53, 54]
- Volume of Fluid (VOF) Method: Ideal for significant surface tension effects [33, 55]
- Moving Mesh Method: Suitable for scenarios without topology changes [56, 49]

From previous simulations and experiments, it is clear that microgravity conditions strongly increase the influence surface tension has over the solidification process in the abscence of gravity-gradient convection, making the VOF option the best choice if these effects are to be captured. Indeed, a good portion of previous orbital DED simulation attempts [52, 49, 54] use VOF. However, as this model is not intended to capture the thermal evolution of the melt pool, simple static meshes with discrete elements being activated and heated in sequence are used instead.

2.5.2. ISAM Modeling State of the Art

Luchinksy et al. [11] developed an analytical model of WAAM using Argon shielding gas in microgravity. The objective was to understand how shielding gas flow, droplet separation, and weld quality would develop under such conditions. The model is comprehensive, taking into account the two-phase gas and liquid flow of the shielding gas and droplets, mass and energy conservation, magnetohydrodynamics, and evaporation, among others, as shown in Figure 2.13.

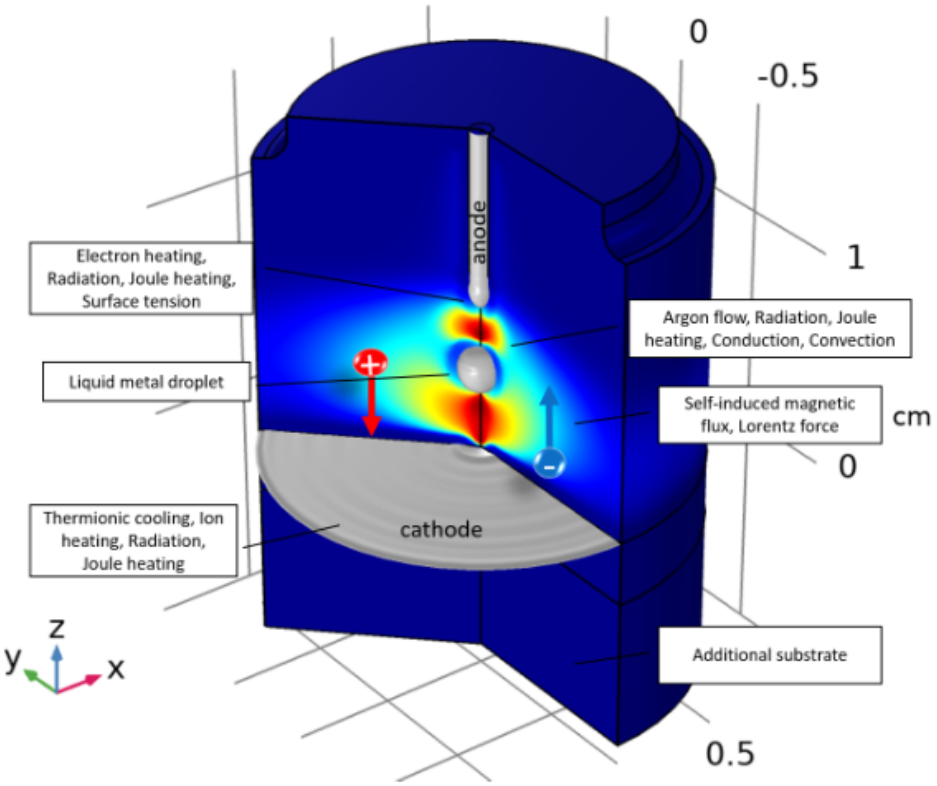


Figure 2.13: Simulation setup for WAAM in microgravity [11]

However, this work was limited by the time-intensive nature of the simulations, which were performed using COMSOL Multiphysics. The simulations were also limited to short timeframes, as the model was not designed to simulate the entire process.

Other attempts at simulating DED processes [57] have also faced similar tradeoffs between fidelity and solution scope, since an accurate representation of the weld pool dynamics often comes at the expense of representing the deposition process at the macro level.

Gu and Li [33] developed CFD transient models using ANSYS to study the impacts of gravity and pressure on the wire-based LMD process for space applications. Their model, which tracks the free surface using the VOF model, includes phenomena like the Marangoni effect, recoil pressure, surface tension, heat transfer, melting, and solidification. They found that in microgravity, surface tension significantly affects melt pool dynamics, causing irregular deposition tracks, as shown in Figure 2.14. This can be mitigated by adjusting wire deposition rates. Reduced pressure increases material vaporization, which is controllable by modifying laser power and scanning speed. Their findings, validated against Earth-based experiments, emphasize the need for precise parameter control in space manufacturing.

Another study [55] using the CFD method and Open Foam software explored laser DED with metal wire in space-like conditions. The authors showed that lower ambient pressure increases metal vaporization, affecting melt pool stability, while zero gravity changes melt pool behavior due to dominant surface tension forces. These results indicate that with proper process adjustments, laser DED can be viable for manufacturing metal parts in space, enhancing the self-sufficiency of long-term space missions.

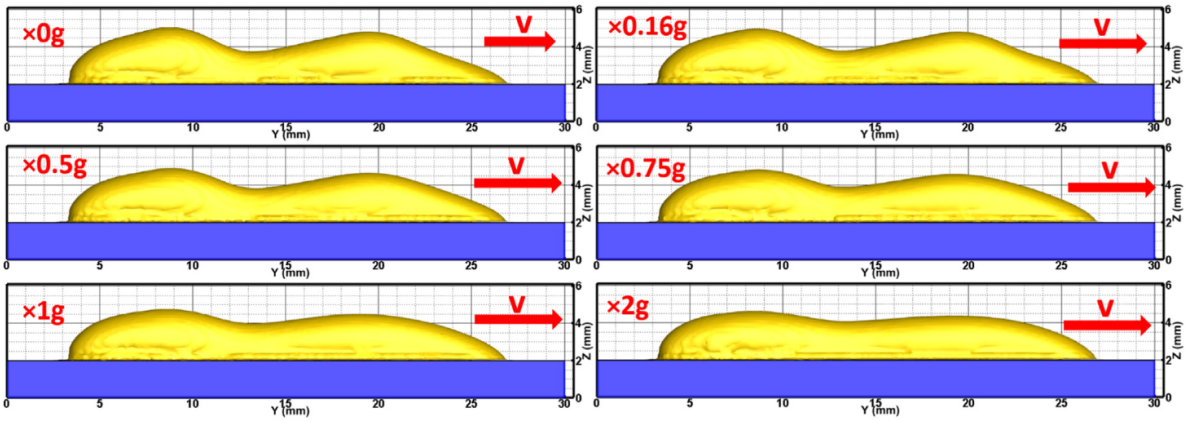


Figure 2.14: Irregular deposition tracks for laser wire DED for several gravitational conditions [33]

Taghizadeh et al. [48] reviewed the state of the art in numerical simulations of metal orbital DED processes with a focus on laser processes, identifying the main gaps in previous literature as being a lack of comprehensive models taking into account the main conditions of interest and mechanisms at play, like microgravity, vacuum, surface tension, and the Marangoni effect.

In macroscale simulations, the exact melt pool fluid dynamics can often be approximated by modelling the shape of the heat source using specific geometries. For example, Sikan et al. [58] modelled EBF3 with a Gaussian heat source as shown in Figure 2.15, which corresponds to the actual penetration patterns of electron beams in metals. Ding et al. [59] modelled WAAM using a double-ellipsoid heat source instead, also called the Goldak heat source model, as this shape better captures the effect of a moving heat source on the melt pool.

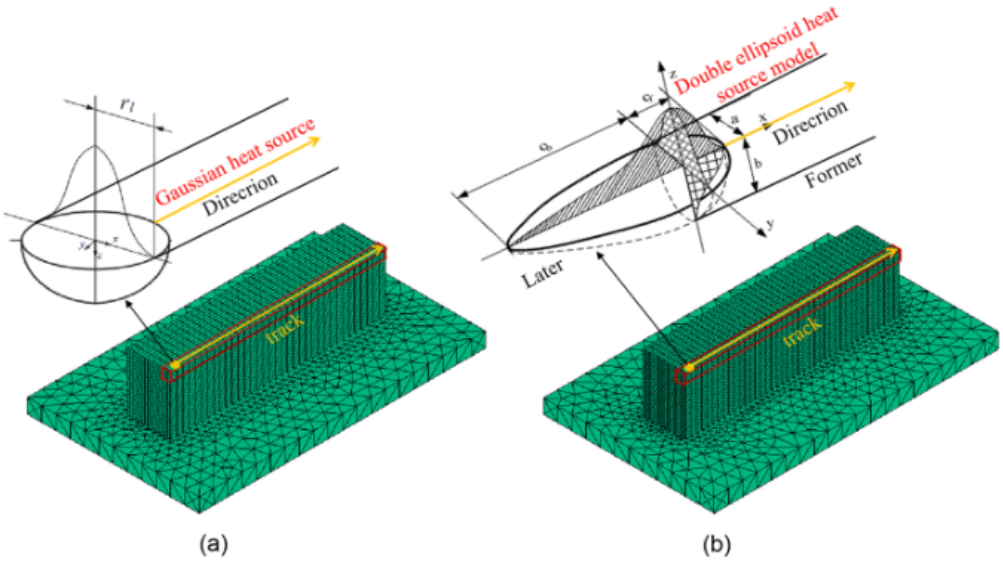


Figure 2.15: Gaussian and double-ellipsoid (Goldak) heat sources [59]

However, Ding et al. [59] only simulated the double-ellipsoid heat source to contrast it with their novel "well-distributed" heat source model. Their modelling approach to simulating deposited feedstock consists of meshing the workpiece into small domains, which are then activated and heated in sequence, as shown in Figure 2.16. The equation for this heat source is given by Equation 2.2, where I is the welding current, U is the welding voltage, K is the effective thermal efficiency representing the ratio of the energy delivered to the substrate, A is the cross-sectional area of the process, v is the printing speed, DT is the time of each load step. Here, the time of each load step is equal to the subsequent

solving single step time. This equation looks familiar to that of the heat input in welding, because it is essentially the same, but with the addition of the time of each load step.

This approach was contrasted with Gaussian and double-ellipsoid heat sources for accuracy and, more importantly, computational efficiency, showing that the well-distributed heat source model reduced computation times by more than 90% while maintaining considerable thermal evolution accuracy (within 20%) even with lower-resolution meshes.

$$\text{Heat Generated} = (\mathrm{K} * \mathrm{U} * \mathrm{I})/(\mathrm{A} * v * \mathrm{DT}) \tag{2.2}$$

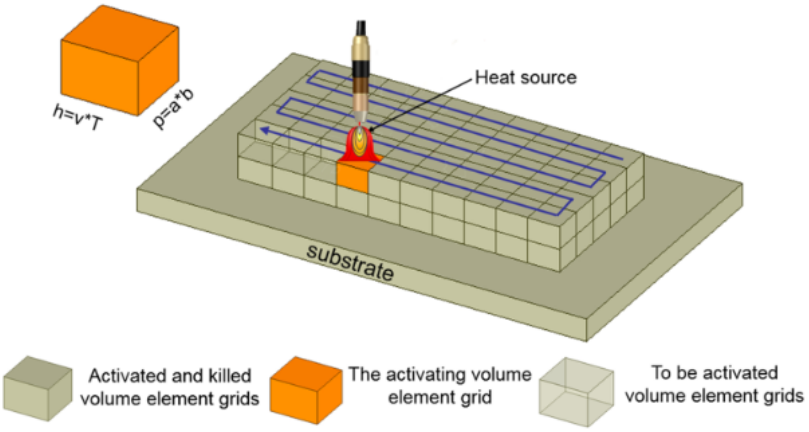


Figure 2.16: Meshing and activation of heat source domains [59]

The drawback of this method in lieu of modelling liquid flow in the melt pool and feedstock is that is does not capture the effects of surface tension or Marangoni convection, which are all significant in microgravity conditions. This also implies that micro-defects cannot be captured, since the geometry of the workpiece is fixed. However, Marangoni convection, which is the convection of liquids with high surface tension gradients (where higher surface tension results from lower temperatures) has been adequately approximated in other literature [60] by artificially raising the thermal conductivity of the liquid phase by a factor of 2.5.

2.6. Research Objectives

Based on the review of the existing literature, several clear conclusions can be drawn and knowledge gaps can be identified as follows:

- Metal Wire DED ISAM, while sparsely researched, has mostly been focused on EBF3 and LWDED, with WAAM being the least researched.
- Modeling DED processed in microgravity is still in its infancy, with most models attempting to capture the thermal dynamics of the melt pool.
- Systematically relating process parameters to material properties in ISAM is still lacking.
- Thermal modelling of WAAM for complex geometries at the macroscale is still underrepresented, with most of the macroscale models limiting themselves to simple bead geometries.
- Investigations of thermal profiles for complex structures printed in orbital vaccum do not exist at present.

Based on the identified knowledge gaps, the corresponding research questions are formulated along with a research plan to answer them:

1. How well can analogous terrestrial experiments in combination with computational simulations be used to predict ISAM performance?

2. What are the optimal process parameters for Wire Arc Additive Manufacturing (WAAM) in space-analogous conditions?
3. How do printing parameters (heat input, geometry, cooling times) affect thermal dynamics during ISAM?
4. What is the thermal design space for ISAM-printed components, and what thermal control strategies would be required for future mission designers?

By exploring the answers or partial answers to these questions, this research aims to build a theoretical model that is capable of simulating material responses to different conditions in orbit and in laboratory conditions. This thermal model is expected to be validated against experiments in space-analogous conditions to ensure that it is capable of predicting the thermal history of ISAM components.

2.6.1. Research Plan and Investigation Workflow

The initially planned and actual research plan's timelines are shown in Figure 2.17. In the original plan, after a literature review conducted in the first two months, modeling and experimental setup are followed by weld experiments designed to validate the thermal model, concluding with tests on the printed samples and writing. However, initial difficulties with development of the model and feedstock procurement caused timeline delays, pushing the main experimental tests 2 months back. In the process of developing the model, it was also found that continuous development would be needed instead.

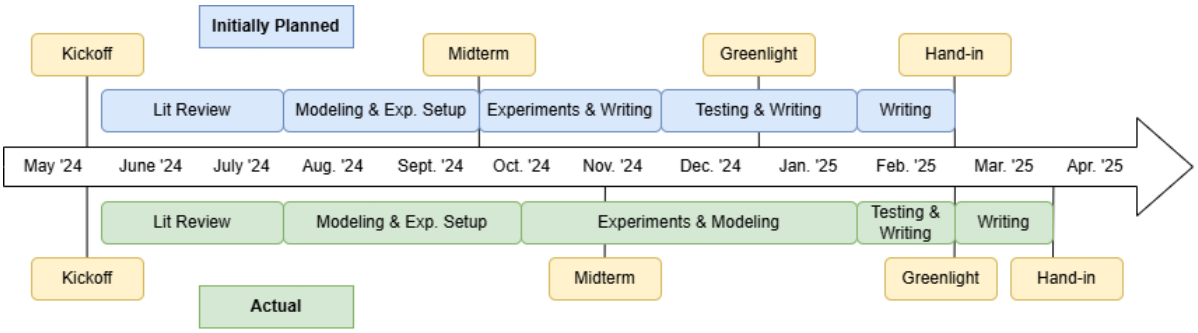


Figure 2.17: Initially planned and actual timelines for the research work

The main work of this research was conducted in the following order. The development of the thermal model progressed throughout all experimental work due to the signficant setup required for the required code. A feedstock wire was selected, characterized for weldability, and weld parameters optimized for additive manufacturing. A small test geometry was printed to validate convective heat transfer coefficients for simulations of later tests. A larger test geometry was then printed under high-temperature conditions to approximate orbital welding conditions, and recreated in thermal simulations. The resulting workpiece was then analysed for material properties and microstructure. Finally, thermal simulations for orbital conditions were performed and compared to the experimental results.

2.6.2. Thesis Structure

The current thesis was written in the following structure to present the research work performed aiming to guide the reader to have a general overview of this work. Chapter 2 concludes here with the review of the existing relevant literature. In Chapter 3, the thermal model and the supporting theory is presented, along with all simulations, their boundary conditions and assumptions. Chapter 4 outlines the materials used and their properties, the experimental setup, and all practical experiments conducted. In Chapter 5, the results of the experiments and simulations are contrasted and analysed, along with supporting material property and microstructure results. Chapter 6 concludes the thesis, summarizing the findings and providing recommendations for future research.

3
Modeling and Simulation

In order to answer the research questions posed in Chapter 2, a valid thermal model for structure-level thermal analysis during a WAAM process must be developed. This model must first be validated against experimental results, and then applied with relevant ISAM boundary conditions to predict the thermal history of ISAM components during deposition. This chapter covers the preliminary structural design of the component being modeled, the translation of this design into a geometric model, the development of a simplified model for heating conditions in orbit to be applied in simulations, and the setup of the different simulations performed. The development of the thermal model and experimental work occurred concurrently, but all the theory and development of the thermal model is presented first in order to build a foundation for the experimental work.

3.1. Basic Simulation Tools and Concepts

In this section, the software tools used for thermal modeling are introduced along with the thermal model being implemented in simulations. For thermal simulations, Ansys Mechanical was chosen as a solver due to its built-in capabilities for transient (time-dependent) thermal analysis, and its ability to handle complex geometries.

3.1.1. Simulation Package

Thermal simulations in Ansys utilize finite element analysis (FEA) to predict temperature distributions and heat transfer within a given model. The process begins with geometry definition, followed by material property assignment, meshing, boundary condition application, and simulation execution. The particular combination of tools used in this research is Ansys Mechanical for model definition, the Welding Toolbox extension to create the printing process, and the Mechanical Ansys Parametric Design Language (APDL) for more custom boundary condition definitions. All simulations were performed on the TU Delft Delftblue HPC cluster to parallelize the simulations.

3.1.2. ANSYS Concepts

APDL provides scripting capabilities for geometry, boundary conditions, and model logic description. Key concepts include:

- **Element birth and death**: Enables dynamic addition/removal of elements, representing incremental material addition. Deactivated elements have thermal conductivity set to 1×10^{-6}, but are still present in the model. [61]
- **Nodal constraints**: Required for 'floating' nodes not attached to active elements to prevent convergence errors. [62]
- **Surface effects**: Implemented via SURF152 elements for heat inputs, radiation, and convection, with extra nodes for ambient temperature modeling. [62]
- **Thermal contact elements**: CONTA170 and TARGE174 elementsdefine heat transfer and physical contact (bonding, sliding, etc.) between contacting parts. [62]
- **Welding Toolbox**: Process-agnostic Ansys 2024 R2 beta extension allowing simple control over part activation and heat input to mimic a discrete-element welding process. This extension was partially rewritten in APDL to allow for more control over the logic, detailed in Appendix A.

3.2. Geometric Model and Mesh

3.2.1. Structural Design

The structural model represents a space station habitat module pressure vessel, focusing on in-space manufacturing scenarios where launch forces can be eliminated. The design is based on the ISS Harmony module dimensions (length: 7.067m, diameter: 4.216m) [63], with quasi-elliptical end caps incorporating flat sections for International Docking System Standard (IDSS) ports (diameter: 1.255m) [64]. For laboratory testing purposes, the model was scaled to 1:24 as shown in Figure 3.1, yielding dimensions of 294.45 mm length and 179.92 mm diameter, with end cap height of 40.889 mm and cap diameter of 69.50 mm.

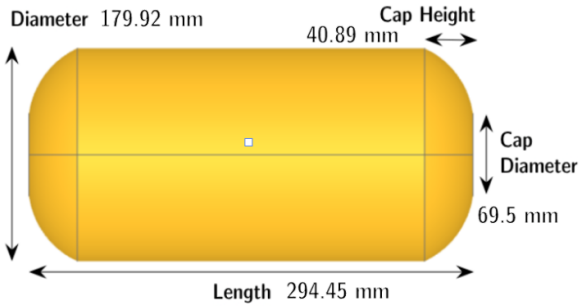


Figure 3.1: CAD model of the scaled down pressure vessel

Three primary structural requirements determine the vessel wall thickness:

1. Pressurization (1 atm internal pressure): The cylindrical pressure vessel experiences hoop and radial stresses [65]:

$$\sigma_\theta = \frac{pr}{\tau} \tag{3.1}$$

$$\sigma_r = \frac{pr}{2\tau} \tag{3.2}$$

   where p is the design pressure, r is the radius, and τ is the wall thickness. Evaluating these equations for a manned space station, which has an internal pressure of 101.325 kPa or 1 atmosphere, and a radius of 2.2 meters (using the real life dimensions of the ISS module), and an allowable stress of 176 MPa (for the chosen wire feedstock as detailed in Section 4.1), the minimum wall thickness is calculated to be 1.27 mm.

2. End cap stress concentrations: Additional stresses occur where the main cylinder meets the end caps. For dished heads, as shown in Figure 3.2a, the minimum wall thickness τ_{min} is given by [66]:

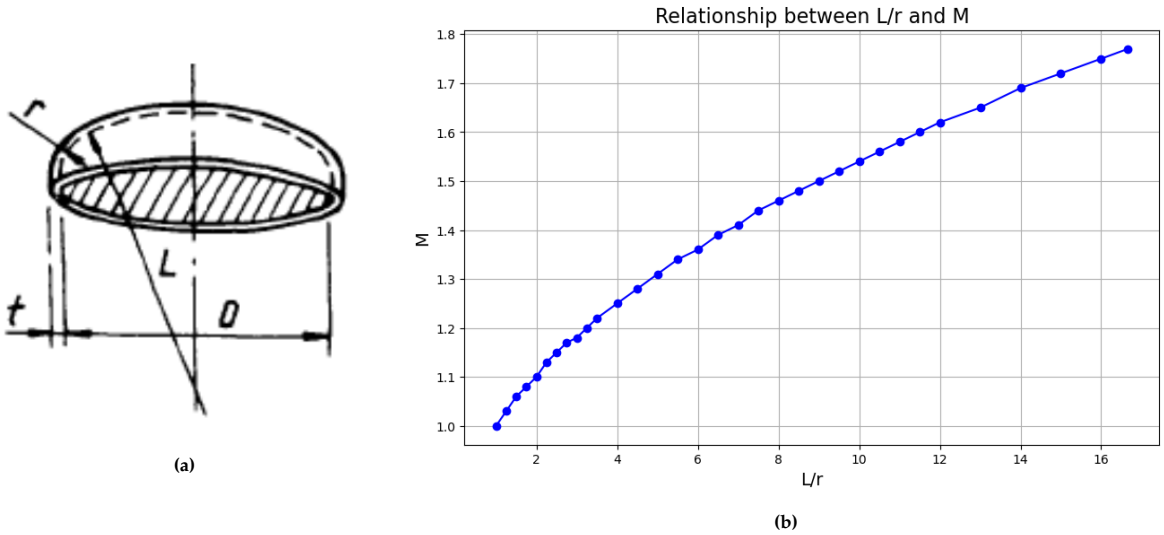


Figure 3.2: (a) Dished head pressure vessel [66], (b) Relationship between L/r ratio and M factor for dished heads [66]

$$\tau_{\min} = \frac{p \cdot L \cdot M}{2\sigma - 0.2p} \tag{3.3}$$

where p is the design pressure (psi), L is the inside length (inches), r is the inside radius (inches), M is a dimensionless parameter from the lookup table based on L/r as shown in Figure 3.2b, and σ is the allowable stress of the material (psi).

Evaluating this Equation 3.3 for our design conditions results in a minimum wall thickness of 2.49 mm, which is slightly larger than the result from the hoop stress analysis.

3. Micrometeoroid and orbital debris (MMOD) protection:

   In the context of space station habitats, micrometeoroid and orbital debris (MMOD) impact poses a significant risk due to the potential for structural damage to the printed part during the printing process. To address this concern, calculations were performed to determine the required thickness of the hull of the pressure vessel to prevent various forms of spallation or perforation. Incipient spallation refers to the initial stage of material failure characterized by the formation of small cracks, detached spallation involves the separation of material fragments from the surface, and perforation denotes the complete penetration of the material. These calculations are based on the work of Ryan et al. [67].

   The required shield thickness to prevent spallation or perforation is given by Equation 3.4, where k is a dimensionless parameter that depends on the type of spallation or perforation, and P_∞ is the impact pressure given by Equation 3.6, where the density ratio ξ is defined in Equation 3.5.

$$\tau_{\min} = k \cdot P_\infty \tag{3.4}$$

$$\xi = \begin{cases} 0.5 & \text{if } \frac{\rho_p}{\rho_s} < 1.5 \\ \frac{2}{3} & \text{otherwise} \end{cases} \tag{3.5}$$

$$P_\infty = 5.24 \cdot d_p^{\frac{19}{18}} \cdot HB^{-\frac{1}{4}} \cdot \left(\frac{\rho_p}{\rho_s}\right)^{\xi} \cdot \left(\frac{V \cdot \cos(\theta)}{C}\right)^{\frac{2}{3}} \tag{3.6}$$

where d_p is the diameter of the projectile, HB is the Brinell hardness of the shield material, ρ_p is the density of the projectile, ρ_s is the density of the shield material, V is the impact velocity, θ is the impact angle, and C is the speed of sound in the shield material.

The MMOD calculations are based on the following assumptions:

- Projectile diameter d_p: 0.3 cm
- Impact velocity V: 7 km/s
- Shield material: Aluminum (Brinell Hardness HB: 80 BN, Density ρ_s: 2.6 g/cm^3)
- Projectile density ρ_p: 2.7 g/cm^3
- Sound speed in shield C: 5 km/s
- Normal incidence impact ($\theta = 0°$)
- The projectile is treated as a rigid body impacting the shield at a specified velocity and angle.
- The shield's material properties are assumed to be uniform and isotropic.
- The effects of temperature and environmental conditions on material properties are disregarded.
- The projectile diameter is representative of typical micrometeoroids and orbital debris encountered at low Earth orbit (LEO) altitudes.
- The impact velocity of 7 km/s reflects the high-speed nature of projectiles in LEO, where relative velocities can exceed this threshold due to orbital mechanics.

Three impact damage thresholds were evaluated with the parameters above:

- Incipient Spallation: 18.809 mm (k=3.0)
- Detached Spallation: 13.793 mm (k=2.2)
- Perforation: 11.285 mm (k=1.8)

Table 3.1 summarizes the required skin thickness for various structural requirements, clearly showing that MMOD protection is the most critical requirement.

Structural Requirement	Required Thickness (mm)	Notes
Pressurization	1.27	Internal 1 atm pressurization
End Cap Pressure	2.49	End cap stress concentrations
Ballistic Impact	14	Prevent spallation from MMOD impact

Table 3.1: Summary of required skin thickness for various structural requirements.

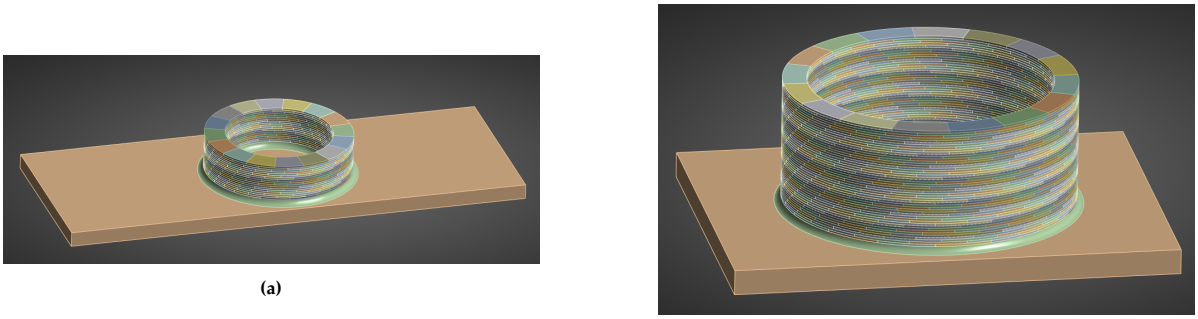
MMOD protection requires a 14 mm wall thickness to prevent detached spallation during the printing process, before the installation of additional protective shielding such as Whipple shields [68]. Detached spallation was chosen as the design condition to prevent detached particles from interfering with the printing process. While this thickness significantly exceeds pressurization requirements, it ensures structural integrity during manufacturing and contributes to operational durability.

Providing external shielding around the entire print volume during ISAM could effectively reduce the required wall thickness to 2.49 mm, resulting in a much lighter structure. Although the removal of launch cost constraints for ISAM structures diminishes the importance of minimizing structural mass, this factor still affects the fuel required for any future positioning or orbit altering maneuvers, and should thus still be considered.

3.2.2. Model Geometry and Dimensions

The pressure vessel geometry detailed in Section 3.2.1 was simplified to thin-walled cylinders to capture the primary thermal interactions, as during the majority of time spent during the printing process, this is the approximate shape of the structure. This simplification facilitates efficient thermal behavior analysis by reducing calculation complexity while reducing computational complexity (as the geometry of the end caps introduces more detailed thermal interactions at the baseplate interface). The Python library CadQuery was utilized for CAD modeling, allowing for the creation of parametric 3D models through a scripting interface.

Two geometries were developed: a small cylinder model and a large cylinder model, as shown in Figures 3.3a and 3.3b. The first one is a recreation of the experiment conducted to validate the convective heat transfer coefficients for the large lab model. The second geometry is the full geometry of the large lab model, which was also used for the space model for the purpose of comparison. Dimensions are specified in Table 3.2, and deviate from those of the scaled-down pressure vessel due to constraints on the maximum size of available baseplates. These cylinder geometries were used as inputs for the robot toolpath creation, and the corresponding Ansys models were designed to replicate the experimental conditions.



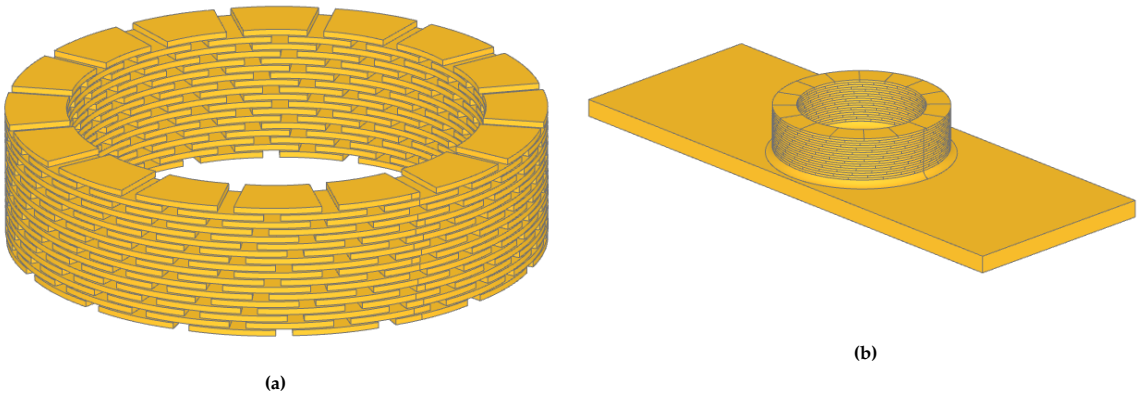
(a) (b)

Figure 3.3: Geometries of the small and large cylinder models. (a) Small cylinder model. (b) Large cylinder model.

Table 3.2: Dimensions of the Two Geometries

Dimension	Small Cylinder	Large Cylinder
Height (mm)	30	75
Radius (mm)	45	80
Thickness (mm)	14.25	14.25
Layer Height (mm)	1.44	1.44
Taper Height (mm)	4	4
Taper Thickness (mm)	22	22
Baseplate Length (mm)	330	200
Baseplate Width (mm)	124	266
Baseplate Thickness (mm)	10.5	15

Figures 3.4a and 3.4b show the slicing of the top part of the cylinder into layers and radial parts, and the final assembly of the cylinder and baseplate, respectively. Each layer has a phase angle of 23 degrees from the previous one to prevent the starting point of the weld bead from coinciding with the end of the previous bead. Each slice is then cut into 16 radial parts that constitute the discrete weld elements that are added in succession to the model during simulation.



(a) (b)

Figure 3.4: CAD representations of the cylinder slicing and final assembly. (a) Slicing of the top part of the cylinder into layers and radial parts. Parts are slightly exploded to show the layers and radial parts. (b) Final assembly of the cylinder and baseplate.

3.2.3. Mesh Techniques and Size

Meshing is essential in thermal simulation, requiring a balance between accuracy and computational efficiency. Mesh elements may be tetrahedral or hexahedral, with specific boundary conditions defined for various geometry parts.

- **Weld Parts:** The mesh for weld parts is regularized by defining subdivisions along certain edges, applicable to all instances due to uniform size, as shown in Figure 3.5. The mesh resolution was lowered in successive simulations until convergence errors began to occur, and the lower limit was found at 7x5x2 elements and per weld part for the large geometry, and 7x4x2 for the small one. The dimensions of the weld parts are 1.44 mm in height, 14.25 mm in width, and 28.6 mm in inner radius length, with the outer radius being 34.2 mm.

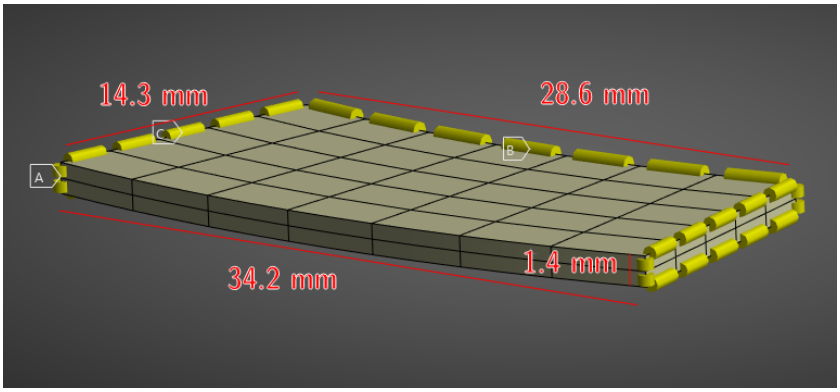


Figure 3.5: Mesh BCs for weld parts

- **Baseplate and Taper Region:** These regions are meshed with tetrahedral elements, with node matching conditions applied to ensure mesh quality at their interface, as depicted in Figure 3.6. The baseplate was meshed with 10 mm elements, while the taper region used 5 mm elements.

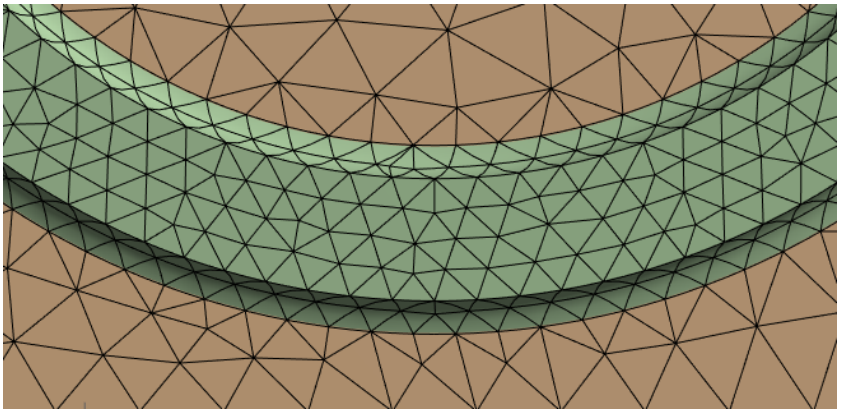
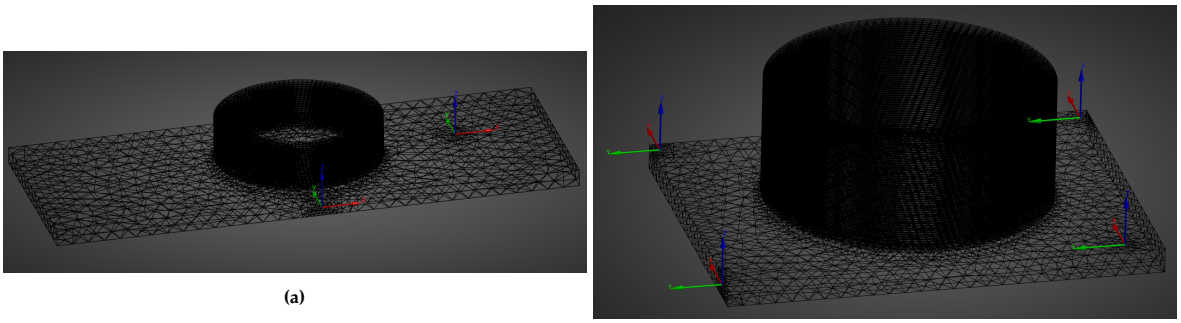


Figure 3.6: Mesh BCs for baseplate and taper region

- **Node Merging:** Coincident nodes from contact elements can cause convergence issues. The node merging feature resolves this by merging such nodes to prevent solver failure.
- **Mesh Refinement for Thermocouples:** Mesh refinement occurs around thermocouple locations to enhance measurement accuracy, utilizing a local refinement with a 10 mm influence radius, as shown in Figures 3.7.



(a)

(b)

Figure 3.7: Mesh refinement for thermocouples in different lab models. (a) Small lab model. (b) Large lab model.

The mesh statistics for the different geometries are shown in Table 3.3. No in-depth mesh convergence studies were performed due to time constraints, but initial simulations with a mesh resolution twice as high as those reported here showed no significant differences in results, leading to the conclusion that the given mesh resolution was sufficient. Several coarser meshes than the reported one were tested, but resulted in convergence errors. The space and lab geometries differ due to the extra mesh refinement at the thermocouple locations for the lab geometry.

Table 3.3: Mesh Statistics for Geometries

Geometry	Nodes	Elements
Small Lab Geometry	121,448	41,201
Large Lab Geometry	377,019	310,474
Large Space Geometry	374,824	308,261

3.3. Thermal Modeling of ISAM

This section outlines the thermal model being implemented in simulations, including the heat inputs in orbit, thermal equations being solved, and boundary conditions for different simulation cases.

3.3.1. Orbital Heat Inputs

During orbital printing operations, the workpiece will be exposed to a variety of heat loads affecting the thermal evolution of the printing process. Thermal control of the workpiece can be achieved using a number of methods, including shielding, active cooling or heating, or conducting the printing process inside a controlled environment in an orbital station. However, when considering the printing of large components (on the scale of space stations), this process must be conducted in the vacuum of space. In order to determine the need for shielding or thermal control, the environmental heat loads for several different cases must first be characterized to establish the extreme conditions that bound the thermal design space. Therefore, two orbital scenarios will be considered with no added thermal measures.

The three main heat sources in LEO are solar radiation, Earth's albedo and Earth's infrared radiation. The heat loads from these sources are dependent on the position of the satellite in orbit, the orientation of the satellite and the geometry of the satellite. Before any heat load calculations can take place, a mission orbit must be selected. A report written by Foster et al. in service of the US Space Force on the thermal modelling of a smallsat in LEO [69] was a fundamental source for this chapter, and many of the design decisions stem from its contents.

Since it is likely that any novel orbital DED operation would initially launch from the ISS, it is prudent to take the ISS's orbit as a baseline for the mission. Table 3.4 shows the main Keplerian orbital parameters of the ISS.

Table 3.4: ISS Keplerian Orbital Parameters

Inclination (°)	RAAN (°)	Eccentricity	Arg. of Periapsis (°)	Period (s)	Max. Altitude (km)
51.6431	217.0648	0.0002083	351.7161	5578	421.232

Taking this orbit and simplifying it to a circular orbit at 421 km altitude with the same inclination allows for some simple orbital cases to be defined to capture different extreme heating conditions. Some underlying concepts must first be defined the selected cases.

In orbital dynamics, the beta angle is the angle between the sun vector and the orbital plane [69]. It is defined as the angle between the sun vector and the projection of the satellite's position vector onto the orbital plane. The beta angle is a key parameter in determining the solar radiation incident on the satellite.

The beta angle can vary over the year, as it depends on several orbital parameters. The beta angle can be calculated using the following equation [69]:

$$\begin{aligned}\beta = \sin^{-1}(&\cos\Gamma \sin\Omega \sin i - \sin\Gamma \cos\varepsilon \cos\Omega \sin i \\ &+ \sin\Gamma \sin\varepsilon \cos i)\end{aligned} \tag{3.7}$$

Where Γ is the Ecliptic True Solar Longitude (which is 0 when Earth is at the vernal equinox), Ω is the right ascension of the ascending node (also called RAAN, it is the measure of angle between the x-axis at the point where the orbit cross the equatorial plane going from south to north), i is the inclination of the orbit (the angular tilt of the orbit from the Earth equatorial plane), and ε is the obliquity of the ecliptic (presently at 23.45°). These parameters are schematically shown in Figures 3.8a and 3.8b.

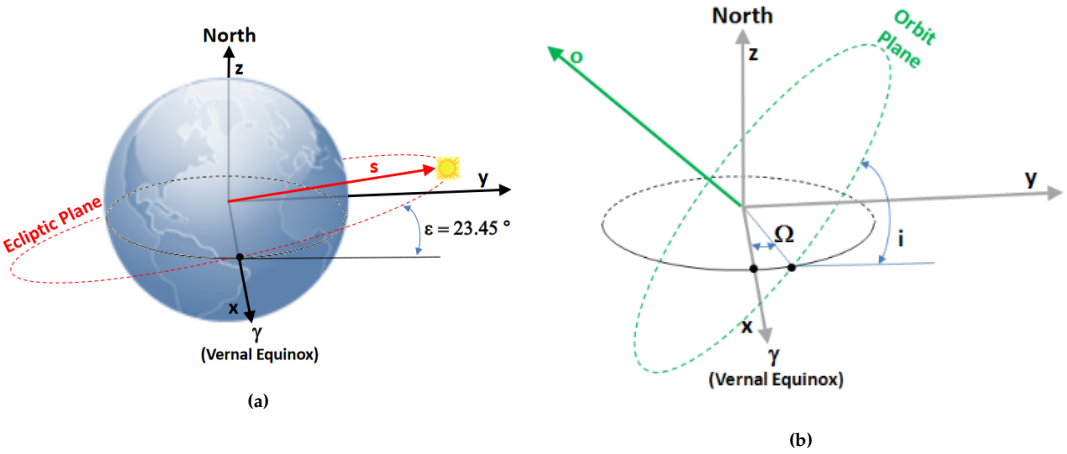


Figure 3.8: Ecliptic true solar longitude and Earth obliquity. (a) Illustration of ecliptic true solar longitude and Earth obliquity [70]. (b) An orbit's RAAN and inclination [70].

Both precession of the satellite's orbit (a shift in RAAN) due to Earth's oblateness and the seasonal variation of earth (a shift in Γ) will cause the beta angle to vary over the year, as shown in Figure 3.9.

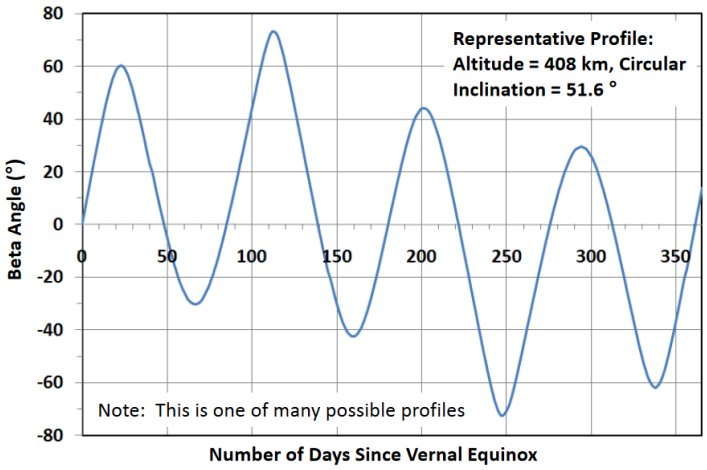


Figure 3.9: Oscillation of the beta angle of a ISS-type orbit over a year [70]

However, for printing periods shorter than a few days, the beta angle can be considered constant.

Modelling the most extreme heat loads for a given altitude allows the boundaries of the thermal design space to be established - these two scenarios are called the "hot" and "cold" cases.

Calculating the extreme β angles for an orbit requires the Equation 3.8,

$$\beta = \pm(\varepsilon + |i|) \tag{3.8}$$

which is a consequence of Equation 3.7. Since Earth's oblateness is 23.45° and the ISS's inclination is 51.6°, the maximum and minimum beta angles are 75° and 0° respectively.

The two orbits selected for the hot and cold cases, meaning the highest heat load that could be imparted on a satellite and the lowest, correspond to beta angles of 75° and 0°, respectively. These are shown in Figure 3.10.

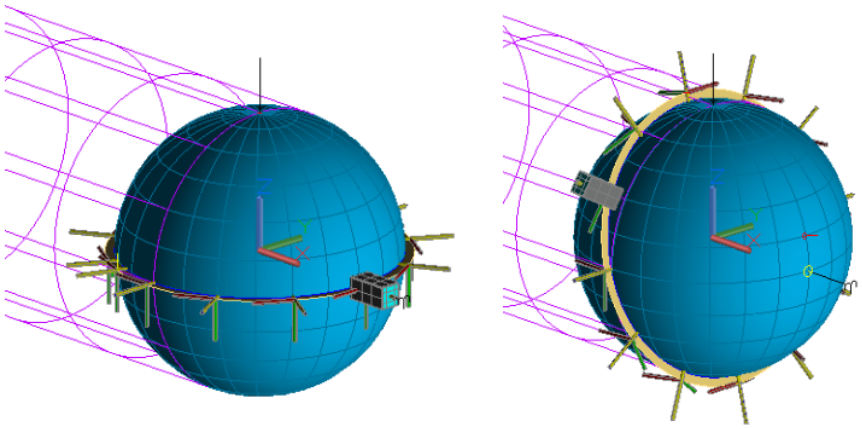


Figure 3.10: Cold (left) and hot (right) case orbits [69]

Earth's orbit around the Sun is slightly eccentric ($e = 0.0167$), and thus the solar flux at Earth varies according to Equation 3.9.

$$\left(\dot{q}_{sol}\right)_{r_{A/P}} = \frac{\left(\dot{q}_{sol}\right)_{r=1}}{r_{A/P}^2} = \frac{\left(\dot{q}_{sol}\right)_{r=1}}{(1 \pm e)^2} \tag{3.9}$$

where $r_{A/P}$ is the distance between the Earth and Sun at aphelion and perihelion, both shown (not to scale) in Figure 3.11.

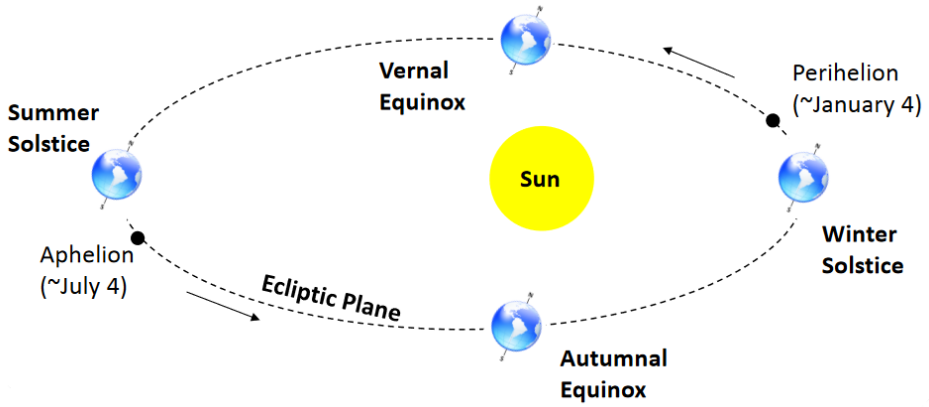


Figure 3.11: Illustration of Earth's changing distance from Sun [70]

Solving leads to maximum and minimum solar fluxes of 1414 W/m^2 and 1317 W/m^2 respectively, taking 1376 W/m^2 as an average solar constant.

Taking the Earth View Form Factor into account is important as it quantifies the fraction of thermal radiation received by a satellite from the Earth. A geometric form factor is a dimensionless quantity that represents the fraction of radiation leaving a surface that strikes another surface, as shown in Figure 3.12a. The form factor between the surface of a planet and the nadir-facing surface of a satellite is given by Equation3.10, the derivation for which can be found in [71], and the geometry of the logic is shown in Figure 3.12b.

$$FF_{\text{nadir}} = \left(\frac{r_e}{r_e + h}\right)^2 \tag{3.10}$$

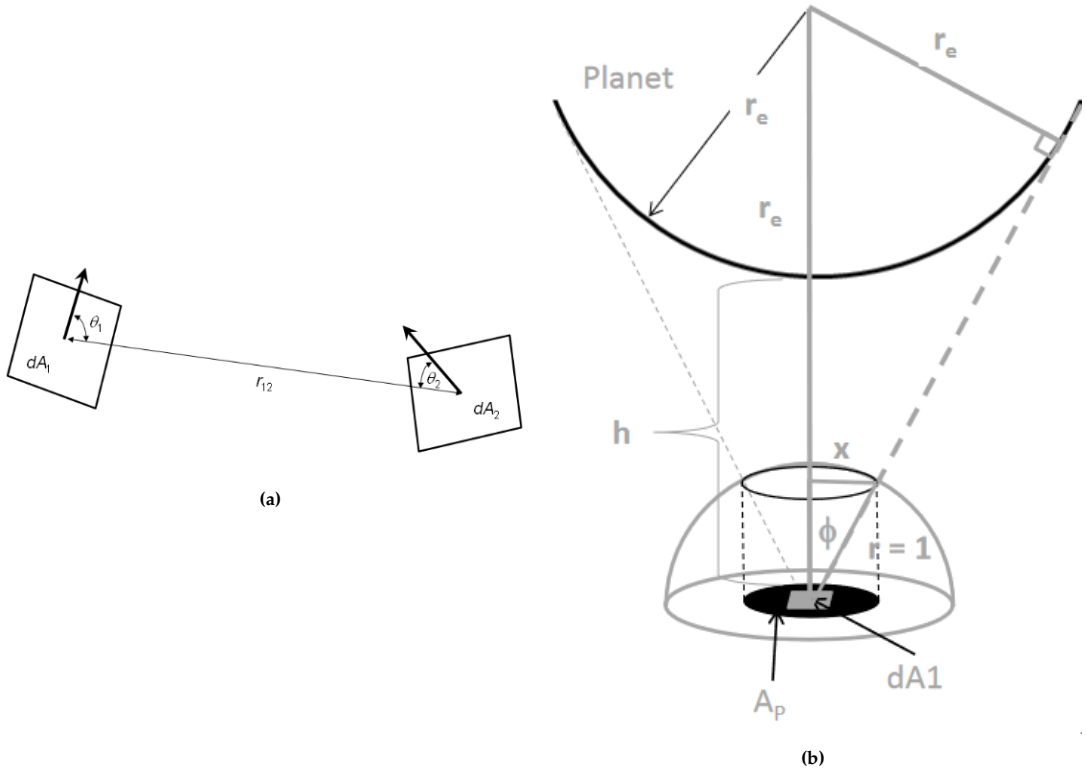


Figure 3.12: Geometric form factors [70]. (a) Generic geometric form factors. (b) Form factor derivation geometry between a nadir-facing surface and a planet.

The form factor for satellite surfaces perpendicular to the nadir-facing surface is given by Equation 3.11 and derivation can be found in [71].

$$FF_{\perp} = \left(\frac{1}{2\pi}\right)\left[\pi - 2\sin^{-1}\left(\sqrt{1-\left(\frac{r_e}{r_e+h}\right)^2}\right) - \sin\left(2\sin^{-1}\left(\sqrt{1-\left(\frac{r_e}{r_e+h}\right)^2}\right)\right)\right] \tag{3.11}$$

For the orbital parameters considered both both the hot and cold cases, the nadir-facing form factor was calculated to be 0.8799, while the perpendicular form factor was calculated to be 0.2839.

The consideration of albedo is crucial as it directly influences the amount of solar radiation reflected by the Earth's surface onto an orbiting satellite. The albedo radiation hitting the nadir-facing surface of a satellite is given by Equation 3.12, where θ is the true anomaly of the satellite, ρ is the albedo of Earth, and β is the beta angle, although the perpendicular form factor should be used for other surfaces.

$$\left(\dot{q}_{\text{alb}}\right)_n = \dot{q}_{\text{sol}}\,\rho\left(\frac{r_e}{r_e+h}\right)^2 \cos\theta\cos\beta \tag{3.12}$$

Earth's albedo varies significantly across the Earth's surface, being highest near high latitudes because of the reflectivity of ice and snow. An average albedo of 0.3 is chosen for the the high-latitude hot case, and 0.15 for the low-latitude cold case, as per [69].

Earth is irradiated by the Sun and emits IR radiation as a result. However, the IR frequency spectrum is largely absorbed by the Earth's atmosphere, and only 15-30% of the outgoing IR radiation is emitted into space, as shown in Figure 3.13. However, the atmosphere itself also emits IR radiation, albeit at a

lower temperature and thus frequency, partially increasing the total emitted IR flux. In satellite thermal modelling, it is customary to assume that the total emitted IR flux is 100% of the outgoing IR radiation [70] as a simplification.

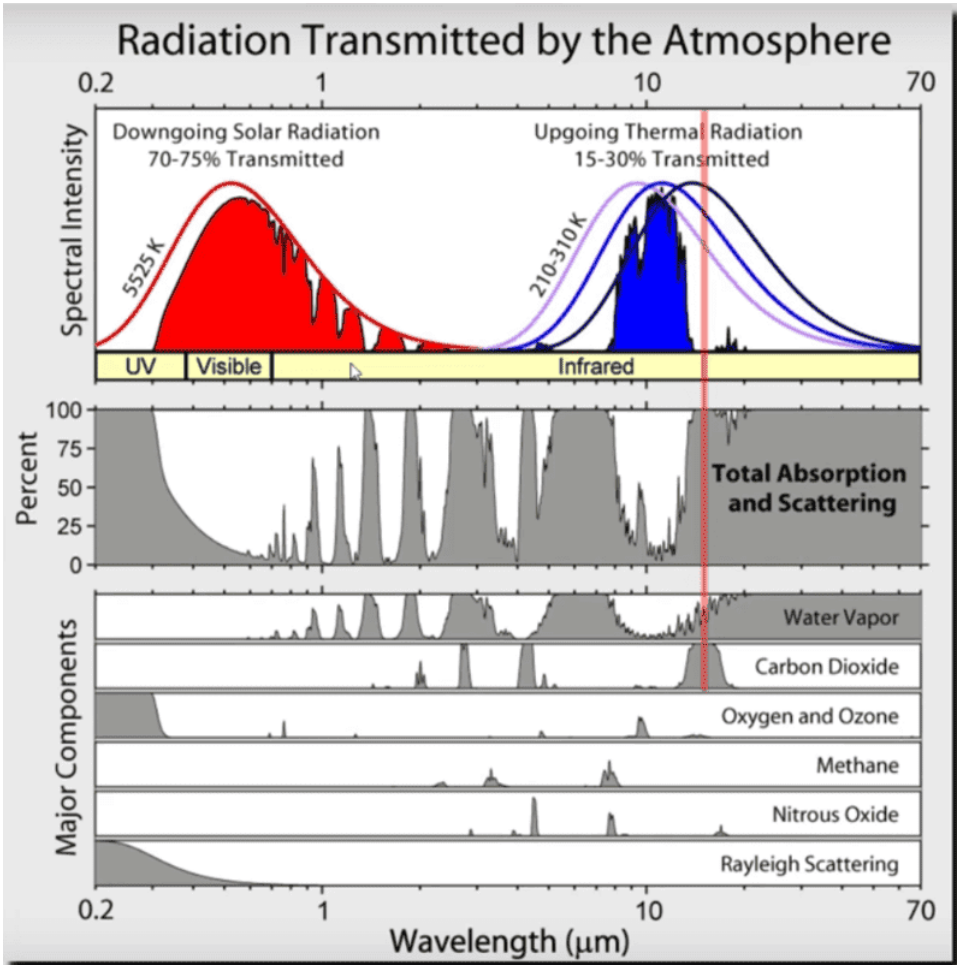


Figure 3.13: Atmospheric absorption bands [72]

The incoming irradiation on a sphere has the projected area of a circle with a radius equal to that of the planet. Setting up the thermal balance for Earth, we have:

$$\dot{q}_{\text{sol}} A_{\text{proj}} (1 - \rho) = 4\pi r_e^2 \varepsilon \sigma T^4 \tag{3.13}$$

Substituting in the value of the projected irradiation area allows us to isolate the outgoing IR $\dot{q}_{\text{pla}} = \pi r_e^2 \varepsilon \sigma T^4$ in terms of the solar flux:

$$\dot{q}_{pla} = \frac{\dot{q}_{sol}(1 - \rho)}{4} \tag{3.14}$$

Where ρ is the albedo of Earth. Solving this for the solar flux at the hot and cold cases, we get 265 W/m^2 and 227 W/m^2 respectively. Finding the flux incident on an orbiting satellite requires multiplying by the form factor of the surface in question.

The consideration of the time spent in eclipse is crucial as it significantly reduces the solar flux received by the satellite, and thus the total heat load. Solar flux hitting Earth's surface creates a conical shadow as shown in Figure 3.14.

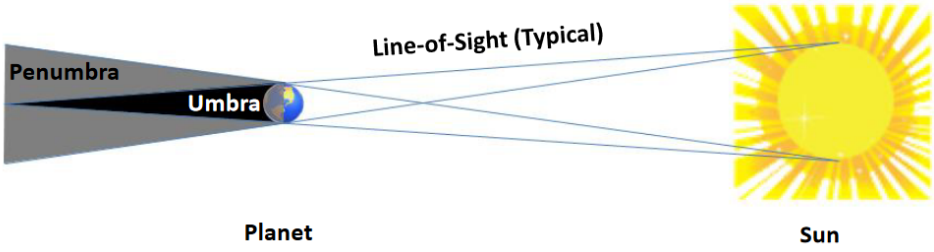


Figure 3.14: Illustration of conical shadow [70]

However, for modelling purposes, a cylindrical shadow model can be used, at the cost of some accuracy when entering and exiting eclipse. This is usually a reasonable approximation for a satellite in a low Earth orbit due to the little time spent in the penumbra. The true anomaly of the satellite at eclipse onset and offset depends on its altitude and beta angle, and is given by Equation 3.15, the derivation of which can be found in [70].

$$\sin\theta = \sqrt{\frac{1}{\cos^2\beta}\left[\left(\frac{r_e}{r_e+h}\right)^2 - \sin^2\beta\right]} \tag{3.15}$$

The total arc length spent in eclipse is then $2(\pi - \theta)$. Of note is that for an orbit at this altitude (421 km), there will be no eclipse above a beta angle of 71°, meaning the hot case satellite will always receive solar flux.

For the cold case, the satellite will enter eclipse at a true anomaly of 110.27° and exit at 249.72°, keeping it in sunlight for 61.2% of the orbit.

In order to simplify the heat load calculations, an orbiting satellite (or structure being printed) with complex geometry can be modelled as a cube enveloping the volume of the structure so that the thermal flux can be calculated for each face independently, as shown in Figure 3.15. This assumption serves only to simplify the heat fluxes arriving from each direction from the structure's perspective, with those directional fluxes then being applied to all faces facing the given direction in the real geometry. The figure shows the Earth-sun system in plane with the satellite's orbit from the side, perpendicular to the orbital plane. The face numbers correspond to the following faces:

1. Zenith: faces away from the planet
2. Nadir: faces the planet
3. Forward: velocity vector-facing
4. Aft: anti-velocity vector-facing
5. North: positive perpendicular to the orbital plane
6. South: negative perpendicular to the orbital plane

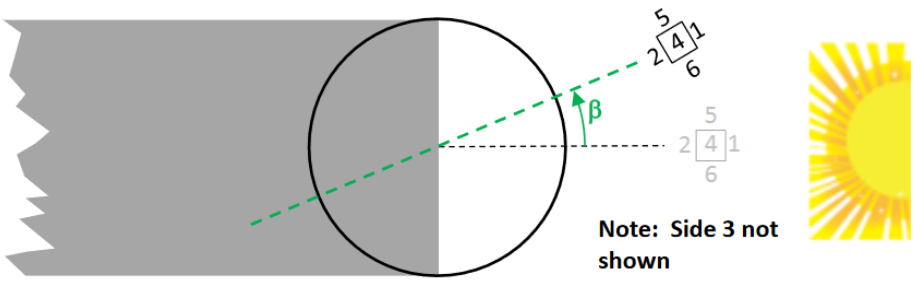


Figure 3.15: Illustration of the orbiting cube model [70]

The heat load calculations for the six faces of the satellite are based on the following equations for solar radiation, albedo, and planetary infrared (IR) heating. The eclipse condition in the equations refers to the following logic: $\theta_{\text{entry}} > \theta \vee \theta > \theta_{\text{exit}}$.

Zenith-Facing Side
Solar Heating:

$$q_{\text{sol, zenith}}(\theta) = q_{\text{sol}} \cdot \cos(\theta) \cdot \cos(\beta) \tag{3.16}$$

Planetary IR Heating:

$$q_{\text{pla, zenith}}(\theta) = 0 \tag{3.17}$$

Albedo Heating:

$$q_{\text{alb, zenith}}(\theta) = 0 \tag{3.18}$$

Nadir-Facing Side
Solar Heating:

$$q_{\text{sol, nadir}}(\theta) = \begin{cases} -q_{\text{sol, zenith}} & \text{if } (\theta < \theta_{\text{entry}} \wedge \theta > 90^\circ) \\ 0 & \text{if } (\theta > \theta_{\text{exit}} \wedge \theta < 270^\circ) \\ 0 & \text{otherwise} \end{cases} \tag{3.19}$$

Planetary IR Heating:

$$q_{\text{pla, nadir}}(\theta) = q_{\text{pla}} \cdot FF_{\text{nadir}} \tag{3.20}$$

Albedo Heating:

$$q_{\text{alb, nadir}}(\theta) = q_{\text{sol}}(\theta) \cdot \rho \cdot FF_{\text{nadir}} \cdot \cos(\theta) \cdot \cos(\beta) \tag{3.21}$$

North-Facing Side
Solar Heating:

$$q_{\text{sol, north}}(\theta) = \begin{cases} q_{\text{sol}} \cdot \cos(\beta + 90^\circ) & \text{if } \beta < 0 \wedge \text{eclipse} \\ 0 & \text{otherwise} \end{cases} \tag{3.22}$$

Planetary IR Heating:

$$q_{\text{pla, north}}(\theta) = q_{\text{pla, nadir}}(\theta) \cdot FF_{\perp} \tag{3.23}$$

Albedo Heating:

$$q_{\text{alb, north}}(\theta) = q_{\text{alb, nadir}}(\theta) \cdot FF_{\perp} \tag{3.24}$$

South-Facing Side
Solar Heating:

$$q_{\text{sol, south}}(\theta) = \begin{cases} q_{\text{sol}} \cdot \cos(\beta - 90^\circ) & \text{if } \beta > 0 \wedge \text{eclipse} \\ 0 & \text{otherwise} \end{cases} \tag{3.25}$$

Planetary IR Heating:

$$q_{\text{pla, south}}(\theta) = q_{\text{pla, nadir}}(\theta) \cdot FF_{\perp} \tag{3.26}$$

Albedo Heating:

$$q_{\text{alb, south}}(\theta) = q_{\text{alb, nadir}} \cdot FF_{\perp} \tag{3.27}$$

Forward-Facing Side
Solar Heating:

$$q_{\text{sol, forward}}(\theta) = q_{\text{sol, zenith}}(\theta - 90^\circ) \cdot \begin{cases} 0 & \text{if } \theta \leq \theta_{\text{exit}} \\ 1 & \text{otherwise} \end{cases} \tag{3.28}$$

Planetary IR Heating:

$$q_{\text{pla, forward}}(\theta) = q_{\text{pla, nadir}}(\theta) \cdot FF_{\perp} \tag{3.29}$$

Albedo Heating:

$$q_{\text{alb, forward}}(\theta) = q_{\text{alb, nadir}}(\theta) \cdot FF_{\perp} \tag{3.30}$$

Aft-Facing Side
Solar Heating:

$$q_{\text{sol, aft}}(\theta) = q_{\text{sol, zenith}}(\theta + 90^\circ) \cdot \begin{cases} 0 & \text{if } \theta \geq \theta_{\text{entry}} \\ 1 & \text{otherwise} \end{cases} \tag{3.31}$$

Planetary IR Heating:

$$q_{\text{pla, aft}}(\theta) = q_{\text{pla, nadir}}(\theta) \cdot FF_{\perp} \tag{3.32}$$

Albedo Heating:

$$q_{\text{alb, aft}}(\theta) = q_{\text{alb, nadir}}(\theta) \cdot FF_{\perp} \tag{3.33}$$

Using Equations 3.16 through 3.33, the heat flux on each face can be calculated. The parameters for the hot and cold cases are summarised in Table 3.5.

Table 3.5: Summary of Heat Flux and Parameters for Cold and Hot Cases

Case	q_{sol}	q_{pla}	ρ	β	FF_{nadir}	$FF_{\perp}$	θ_{entry}	θ_{exit}
Hot	1414	265	0.3	75	0.8799	0.2839	-	-
Cold	1317	227	0.1	0	0.8799	0.2839	110.27	249.72

The true anomaly is assumed to be 0 when the satellite is closest to the Sun. The orbiting cube is assumed not to rotate or point in any particular direction, so e.g. the nadir face will always be facing the Earth. This is a simplification that might not apply for an ISM system with adequate thermal control through pointing, but it is a starting condition to which additions like shields and attitude control can be applied. Figures 3.16 and 3.17 show the total heat load for each face for the hot and cold cases, respectively.

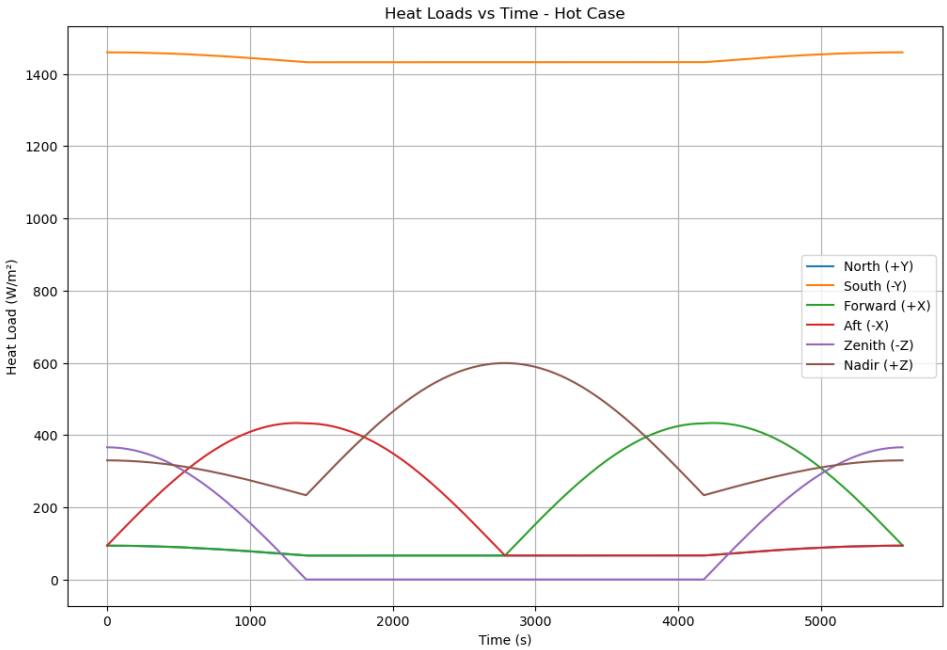


Figure 3.16: Heat loads on all faces for the hot orbital case

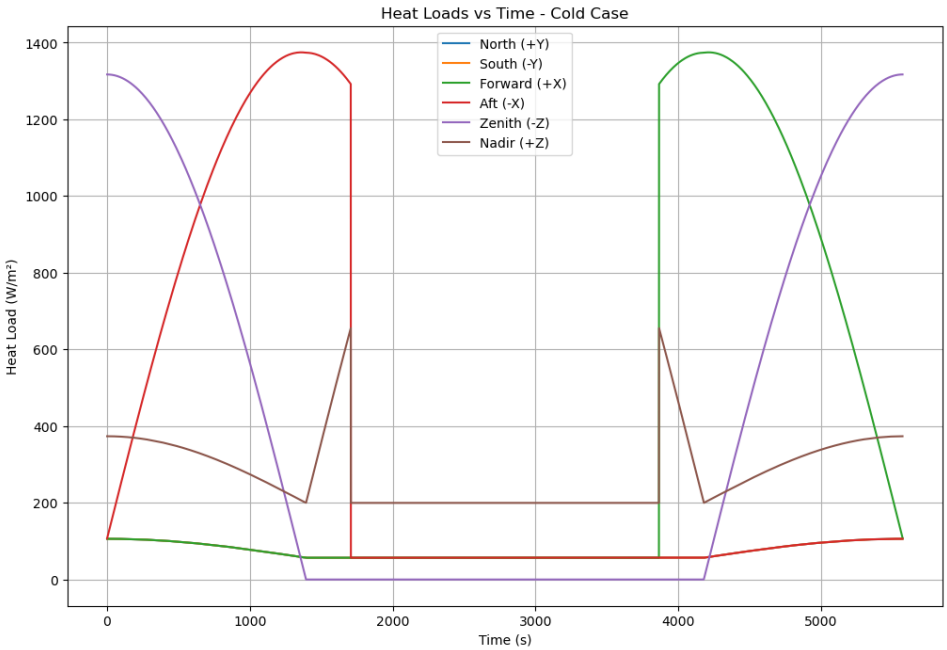


Figure 3.17: Heat loads on all faces for the cold orbital case

Of note is that the total incoming heat load for the hot case only varies by around 300 W/m^2 over the course of the orbit, while the cold case goes from 2550 at peak flux to 227 W/m^2 during eclipse. This makes sense, as during eclipse, the orbiting cube experiences neither direct solar heating nor albedo heating, only receiving IR radiation from the Earth.

Applying the calculated cube-face heat fluxes to the real geometry of the ISAM structure at any point in time is straightforward: all faces of the structure facing the direction of a given face experience the same heat flux as the cube face. This simplification can be refined further by taking incidence angles into account, but this would significantly complexify the model, and is left for future work.

The heat load diagrams for each face and flux type can be found in Appendix B.

3.3.2. Thermal Modeling Physics and Equations

The thermal model in Ansys Mechanical incorporates three fundamental heat transfer modes: conduction, radiation, and convection. The theory in this section is based on Lienhard et al. [**ahtt6e**].

Conduction through direct material contact is governed by Fourier's Law:

$$\frac{\partial^2 T}{\partial x^2} + \frac{\partial^2 T}{\partial y^2} + \frac{\partial^2 T}{\partial z^2} + \frac{\dot{e}_{\text{gen}}}{k} = \frac{1}{\alpha}\frac{\partial T}{\partial t} \tag{3.34}$$

where $\alpha = \frac{k}{\rho c}$ is the thermal diffusivity, k is thermal conductivity, ρ is density, c is specific heat capacity, and $\dot{e}_{\text{gen}}$ is the heat generation rate. For most materials, $\dot{e}_{\text{gen}} = 0$, which simplifies to the Laplace equation:

$$\frac{\partial^2 T}{\partial x^2} + \frac{\partial^2 T}{\partial y^2} + \frac{\partial^2 T}{\partial z^2} = 0 \tag{3.35}$$

The conductive coupling between nodes is given by Equation 3.36 and is based on the thermal conductivity of the material and the geometry of the nodes.

$$GL_{12} = \frac{k_{12}A}{L_{12}} \tag{3.36}$$

Radiation heat transfer through electromagnetic radiation follows the Stefan-Boltzmann Law:

$$q = \sigma \varepsilon A(T^4_{\text{surface}} - T^4_{\text{ambient}}) \tag{3.37}$$

where $\sigma = 5.67 \times 10^{-8}$ W/m^{2}K^4, A is the surface area, T_{surface} is the temperature of the surface, T_{ambient} is the ambient temperature, and ε is the emissivity of the surface. The radiative coupling between surfaces 1 and 2 incorporates view factors F_{12}:

$$GR_{12} = \varepsilon_1 F_{12} A_1 \tag{3.38}$$

where GR_{12} is the radiative coupling between surfaces 1 and 2, leading to the radiative heat exchange between the two surfaces, as given in Equation 3.39.

$$q_{\text{rad}} = \sigma GR_{12}(T_1^4 - T_2^4) \tag{3.39}$$

Radiative heat transfer does not only depend on the temperature of the object, but also on its emissivity ϵ. Emissivity is a measure of how well an object emits radiation, and is a value between 0 and 1. A blackbody has an emissivity of 1, while a perfect reflector has an emissivity of 0. The emissivity is also frequency-dependent, and thus is best expressed as a spectral value, while also being temperature-dependent.

The emissivity of an object can be calculated using Kirchhoff's Law, which states that the emissivity of an object is equal to its absorptivity α. The absorptivity of an object is the fraction of radiation that is absorbed by the object, and is also a value between 0 and 1. All materials also have a transmittance τ and reflectance ρ, which are the fractions of radiation that pass through the material and are reflected by the material, respectively. The absorptance, transmittance, and reflectance of an object are related by Equation 3.40.

$$\alpha + \tau + \rho = 1 \tag{3.40}$$

In the space industry, the EM spectrum is divided broadly into two wavelength bands for thermal exhchange purposes. The absorptivity is generally refers to that quantity in the visible and ultraviolet spectrum, while the emissivity is generally that in the infrared spectrum. Kirchoff's law states that at any given frequency, the absorptivity and emissivity must be equal, but because of these shorthand conventions, they are different, since they refer to different spectral bands.

Convection is due to the cyclic movement of fluids along the surface of a material, as given in Equation 3.41.

$$q_{\text{conv}} = hA(T_{\text{surface}} - T_{\text{ambient}}) \tag{3.41}$$

where q_{conv} is the rate of heat transfer by convection, h is the convective heat transfer coefficient, A is the surface area, T_{surface} is the temperature of the surface, and T_{ambient} is the ambient temperature.

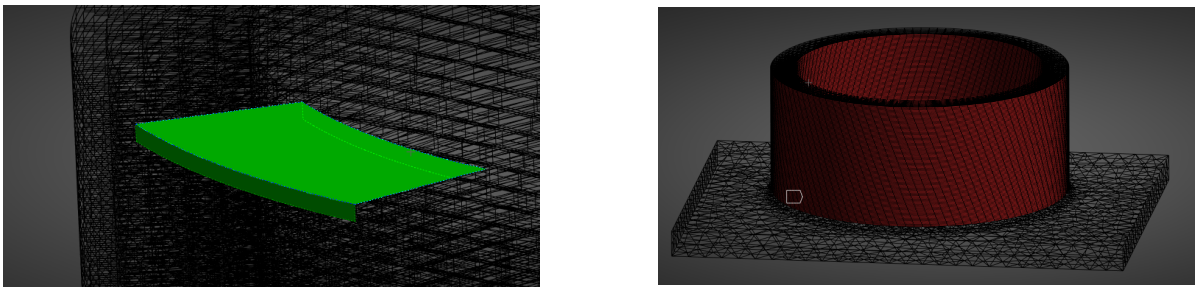
3.3.3. Boundary Conditions and Assumptions

Three different models were created:

1. Small Lab Model: validates the convective heat transfer coefficients for the large lab model
2. Large Lab Model: validates the feedstock initial temperatures and convective heat transfer coefficients for the space model
3. Orbital Model: simulates ISAM for three different heat input cases: hot orbit, cold orbit and shielded (no environmental heat input)

For all three models, some global assumptions were made:

- The welding process is simplified by discretizing each weld layer into a series of weld parts, each with a defined welding time and energy input. Weld parts are initially deactivated and activated sequentially after each welding and cooling step. The energy input, determined by current, voltage and arc energy transfer efficiency, is distributed evenly across the nodes of the added part, with the heat generation rate expressed in watts per cubic millimeter.
- Surface effect elements must be added before simulation. Elements that remain active throughout the simulation can be added via the GUI, while those for weld parts require addition through APDL code. Side and top elements are added separately, as illustrated in Figures 3.18a and 3.18b.



(a) (b)

Figure 3.18: Surface effect elements for the large lab model. (a) Surface elements for a weld part. (b) Side faces of the surface effect elements for the whole model.

To prevent top surface elements from remaining active when a new weld part is placed above, these elements are deactivated prior to each timestep.

- The view factor between all surface elements and the ambient is set to 1, and radiative heat transfer between surfaces in the model is not considered to save computational resources.
- The material properties used for all models are given in Subsection 4.1.1. Where the temperature of the material exceeds the bounds of the given values, the material properties stay constant beyond the bounds.

- The initial two layers of the workpiece (taper region) are not included in the welding logic, but are included in the thermal model with the same initial temperature as the baseplate.
- The discrete weld parts, once added to the model, have an initial temperature. They are then heated according to the welding heat input. This temperature can influence the thermal profile of the simulation. More heat will be added to the weld parts if they are initially hotter.

  According to [73], around 50% of the energy of the arc is used to melt the wire, with the remainder entering the workpiece directly. The following lumped-element thermal balance is used to determine the initial temperature of the weld parts:

$$\left(U \cdot I \cdot \eta \cdot \Delta t\right) \cdot 0.5 = c_p(T) \cdot m \cdot \Delta T + H \cdot m \tag{3.42}$$

  Where U is the voltage, I is the current, Δt is the time interval, η is the arc efficiency, $c_p(T)$ is the specific heat of the wire at temperature T, m is the mass of the weld part, ΔT is the temperature difference between the initial and final temperature of the weld part, and H is the latent heat of fusion of the feedstock. The simplified values used for these parameters are shown in Table 3.6.

Table 3.6: Discrete Element Welding Parameters

Parameter	Value
Latent Heat of Fusion (H)	397×10^3 J/kg
Specific Heat Capacity (C)	950 J/kgK
Voltage (U)	19.59 V
Current (I)	105.38 A
Arc Efficiency (η)	0.8
Mass (m)	1.7×10^{-3} kg
Time Interval (Δt)	4.33 s

  Solving Equation 3.42 for ΔT gives a value of 1790 °C. Experimentally, the melt pool usually reaches temperatures of 1500 °C [74]. However, that heat is immediately transferred to the workpiece, and in a discrete element thermal model, it can be assumed that the maximum temperatures reached by the melt pool will be lower than the theoretical values. The initial temperatures of the weld parts are by default 600 °C, which is the melting temperature of the aluminum alloys, and iterated on in specific models. The logic here is not capturing the exact thermal dynamics of the welding process, but is a simplification concerning the boundary conditions of the lumped-element thermal heating model. Further work must be done to better approximate the thermal dynamics of the welding process in the initial temperatures of the weld parts.
- The models are in a thermally constant ambient environment, and thermally isolated in conduction from the support structures.
- The temperatures of the surface element nodes are constrained at the initial feedstock temperature while they are inactive in order to prevent convergence errors.
- All models have radiative heat transfer between particular surfaces and the ambient, using the thermo-optical properties listed in Table 4.7. These properties are assumed constant with temperature in the solid and liquid phases, which is a simplification that may not be representative of the actual behavior of the materials.

Furthermore, three particular sets of boundary conditions and assumptions were made for each model:

1. Small Lab Model (16 simulations):

Table 3.7: Boundary Condition Parameters for Small Lab Model

Parameter	Value
Initial Baseplate/Taper Temperature	17 °C
Initial Feedstock Temperature	600 °C
Ambient Temperature	17 °C
Interlayer Cooling Time	Non-uniform due to machine process

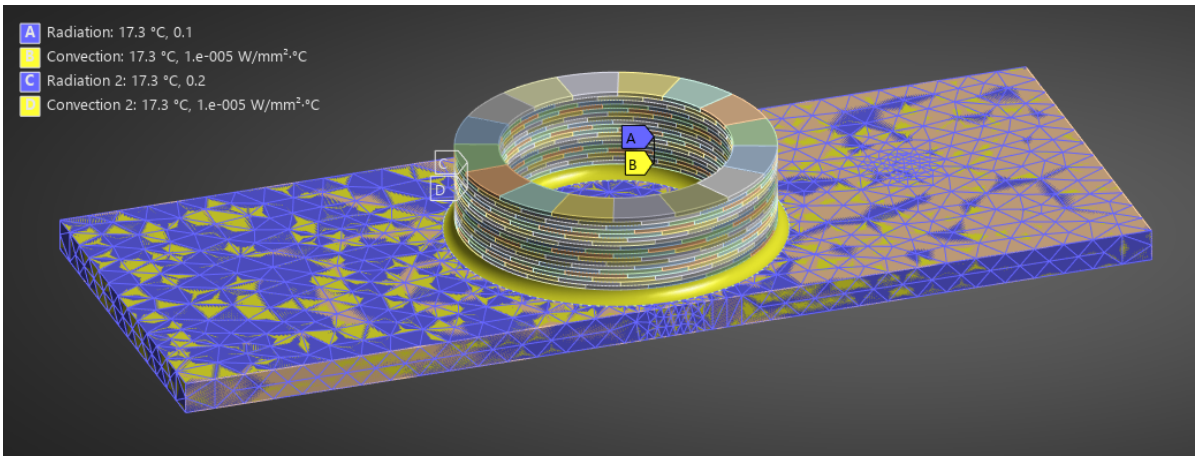


Figure 3.19: Baseplate boundary conditions for the small lab model. The visual irregularities of the blue and yellow surfaces are due to Ansys rendering issues, and indicate that both boundary conditions are applied to the same surface.

As shown in Figure 3.19, the baseplate and taper regions have convection and radiation surface effects applied to them. As specified in Table 3.7, the initial temperature of the model is the same as that of the ambient environment at 17 °C, with weld parts added at 600 °C. Three different convection values are applied to the baseplate, the weld parts, and the top of the currently active weld part. This is done to model the different levels of convection due to the interaction with the flow of the shielding gas. The convective heat transfer coefficients for the weld parts are defined as a range of values, as shown in Table 3.8, and a total of 16 simulations were run to determine the values that best matched the experimental results.

Table 3.8: Convection Coefficients for the Small Lab Model

Parameter	Value
Weld Parts Convection	[8, 15.33, 22.67, 30] W/m^2 C
Baseplate Convection	[8, 13.67, 19.33, 25] W/m^2 C
Active Weld Part Top Convection	40 W/m^2 C

2. Large Lab Model (6 simulations):

Table 3.9: Boundary Condition Parameters for Large Lab Model

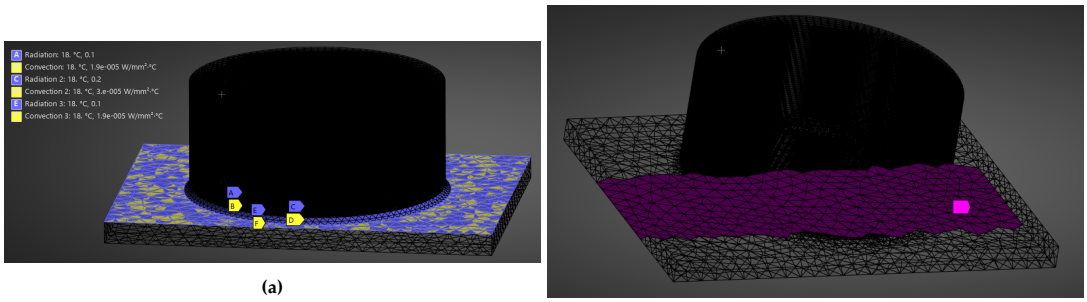
Parameter	Value
Initial Baseplate and Taper Region Temperature	300 °C
Initial Feedstock Temperature	[300, 600] °C
Ambient Temperature	18 °C
Convection	Dependent on small simulation results
Interlayer Cooling Time	62.4 s
Heater Temperature	250 °C

In the large laboratory model, the thermal surface effects are again specified, including the region

of surface effect application, as shown in Figure 3.20. As a heater was also used for this experiment, the region of applied heat is also specified, as shown in Figure 3.20b. The values for the convective heat transfer coefficients are dependent on the validation model results, but further iterated on to capture the added conductive heat loss from the support structures, as shown in Table 3.10. The sides and bottom of the baseplate are assumed to be thermally insulated from the ambient environment and support structures.

Table 3.10: Convection Coefficients for the Large Lab Model

Parameter	Value
Weld Parts Convection	30 W/m^2 C
Baseplate Convection	[19, 22.8, 28.5] W/m^2 C
Active Weld Part Top Convection	40 W/m^2 C



(a) **(b)**

Figure 3.20: Boundary conditions for the large lab model. (a) Baseplate boundary conditions for the large lab model. The visual irregularities of the blue and yellow surfaces are due to Ansys rendering issues, and indicate that both boundary conditions are applied to the same surface. (b) Heater region for the large lab model (seen from below)

Pre-heating of the baseplate is also included in the model through the use of a heater. The addition of the heater to the model is done by setting a constant temperature of 250 °C to the heater region shown in Figure 3.20b, and the initial temperature of 300 °C of the baseplate and taper regions reflects this pre-heating.

3. Orbital Model (15 simulations):

Table 3.11: Boundary Condition Parameters for Space Model

Parameter	Value
Initial Baseplate and Taper Region Temperature	200 °C
Initial Feedstock Temperature	600 °C
Ambient Temperature	4 °K
Interlayer Cooling Time	[60, 120, 180, 240, 300] s
Environmental Heat Input	[Hot, Cold, Shielded]
Liquid Phase (600 °C) Thermal Conductivity	151 W/(m·K)

The boundary conditions for the orbital model are designed to reflect the unique thermal environment of space, as given in Table 3.11. The thermal surface effects are defined, including the region of surface effect application, as shown in Figure 3.21. The thermal conductivity of the feedstock in the liquid phase is set 2.5 times higher than for the lab models, at 151 W/(m·K) to account for the effects of Marangoni flow.

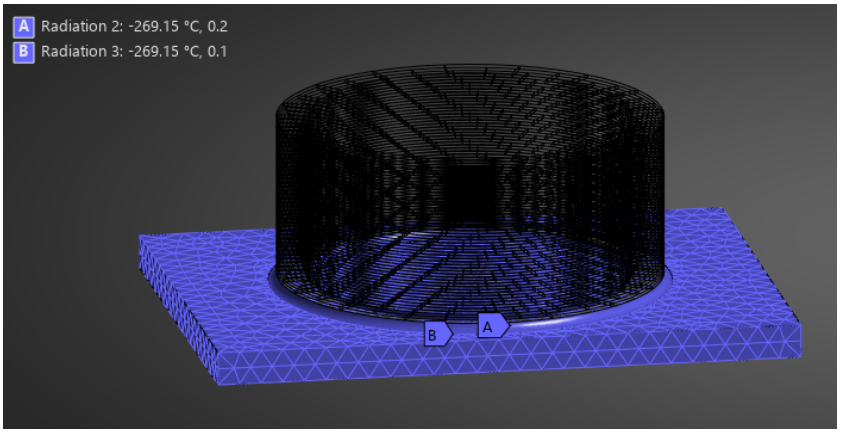
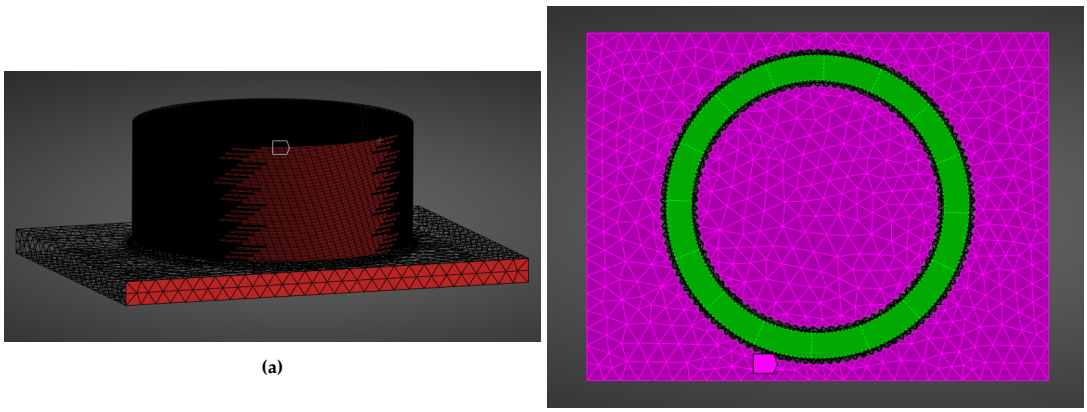


Figure 3.21: Radiation boundary conditions for the space model

Additionally, the exact regions for the application of environmental heat input are specified, as shown in Figure 3.22a. These are defined in the GUI to approximately reflect the regions of the model corresponding to the different faces of the orbiting cube model discussed in Subsection 3.3.1. The top surfaces of the model (facing the positive z-axis) are shown in Figure 3.22b, and corresponds to the top of the baseplate along with the currently exposed tops of the weld parts. This is also assumed to be the zenith-facing side, with the forward-facing side oriented in Y+ direction, and the south-facing side in X+ direction. The heat fluxes applied are given in Figures 3.17 and 3.16, and since these are independent of surface area, the actual heat flow on each direction of the model corresponding to a cube face is calculated by multiplying the heat flux by the surface area of the corresponding face of the orbiting cube model at a given time.



(a)

(b)

Figure 3.22: Heat-receiving surfaces of the model in the space environment. (a) One example of heat-receiving side surfaces of the model. (b) Top heat-receiving surface of the model (both pink and green included)

The two parameters that were iterated over to create a design space for this model were the interlayer cooling time and the environmental heat input. The interlayer cooling time was varied from 60 s to 300 s, and the environmental heat input was either according to the hot orbital case, the cold orbital case, or the shielded case, where no heat input was applied.

3.3.4. Full-Scale Space Habitat Model

In order to apply some of the results from the scaled-down FEM models to the full-scale space habitat, a simplified thermal model was created using Python. While similar estimations could have been made for the scaled-down models, the objective of this work was to develop a model that could be arbitrarily scaled to any size and geometry, and used for any deposition process. Full-scale modeling using FEM was infeasible due to the vast increase in computational resources required.

The three estimated quantities of interest are the environmental heat flows and the equilibrium temperature of the structure over the course of the deposition process. Using the habitat dimensions stated in Section 3.2.1, a baseplate at the bottom of the habitat is assumed with the dimension given in Table 3.12. The X and Y dimensions are designed to give the initial deposition a 10% margin at the edges of the baseplate.

Parameter	Value	Formula
Length	4,855 mm	$(2R + \tau) \cdot 1.1$
Width	4,855 mm	$(2R + \tau) \cdot 1.1$
Thickness	20 mm	

Table 3.12: Baseplate Dimensions

The surface area of each face of the structure over time (again using the orbiting cube simplification explained in Section 3.3.1) is calculated by assuming a constant rate of area increase over the course of each layer.

$$\frac{dA}{dt} = \frac{A_{\text{layer}}}{t_{\text{layer}}} \tag{3.43}$$

Where A_{layer} is the external ring surface area of each layer, and t_{layer} is the time it takes to deposit a single layer.

A_{layer} is found simply by taking the circumference of of the ring and multiplying by the height of the layer.

$$A_{\text{layer}} = 2\pi R \cdot h_{\text{layer}} \tag{3.44}$$

The heat flows for each of the six faces of the orbiting cube model are then calculated by multiplying the surface area by the heat flux and absorptivity, as given in Equation 3.45.

$$Q_{\text{face}}(t) = A_{\text{face}}(t) \cdot q_{\text{face}}(t) \cdot \alpha \tag{3.45}$$

Where $Q_{\text{face}}(t)$ is the heat flow for a given face at a given time, $A_{\text{face}}(t)$ is the surface area of the face at a given time, $q_{\text{face}}(t)$ is the heat flux for a given face at a given time, and α is the absorptivity of the material. $q_{\text{face}}(t)$ was calcuated in Section 3.3.1 and is given in Figures 3.17 and 3.16.

The equilibrium temperatures of the structure are then found by iteratively solving the nonlinear radiative heat balance equation for each face of the structure, as given in Equation 3.46.

$$Q_{\text{total}}(t) \cdot (A_{\text{cylinder}}(t) + A_{\text{baseplate}}) = \sigma \cdot \epsilon \cdot (2 \cdot A_{\text{cylinder}}(t) + A_{\text{baseplate}}) \cdot (T_{\text{structure}}(t)^4 - T_{\text{ambient}}^4) \tag{3.46}$$

Where σ is the Stefan-Boltzmann constant, ϵ is the emissivity of the material, $A_{\text{cylinder}}(t)$ and $A_{\text{baseplate}}$ are the external surface area of the structure and the baseplate, $T_{\text{structure}}(t)$ is the temperature of the structure at a given time, and T_{ambient} is the ambient temperature of space. The cylinder area is doubled for the emitting surfaces, as both the inside and outside surfaces are radiating heat.

3.4. Thermal Model Summary

The model presented in this chapter is a discrete element thermal model that simulates the thermal behavior of a WAAM process, and more generalizably, any wire DED process. This model includes total freedom of thermal boundary condition definition, allowing for laboratory, space, and other conditions. The novelty in this approach is not the thermal model itself, which has been extensively validated in previous works, but the application of orbital conditions to a wire DED process.

3.4.1. Implementation of the Model

Currently, the implementation of this model is still cumbersome and requires several different software tools in combination. All definition of geometry is done during CAD preparation, and this geometry is imported into Ansys Mechanical. The calculation of orbital heating parameters is currently done in a local Python environment, and the results thereof have to be translated to tables in APDL code. The definition of material properties, baseplate boundary conditions, welding sequence, and named selections (groups of elements, surfaces, or nodes) is done in Ansys Mechanical through the GUI. This model is then exported to a solver input file, which is then edited to include the custom code that implements the surface effect elements, along with contact element activation. This solver input file can then be run by invoking Ansys APDL from the command line in any cloud or local environment. The thermal transport equations defined in Subsection 3.3.2 are solved within Ansys and do not have to be implemented by the user.

3.4.2. Capabilities and Usage

The model accommodates various manufacturing methods (WAAM, EBF3, LWDED) through process-agnostic energy input and duration definitions. The heat input can be defined either indirectly using voltage, current, and energy transfer efficiency, or directly using a heat source term. It enables complete control over convection, radiation, and ambient temperature settings, as well as the regions affected by these boundary conditions. Additional boundary conditions like active thermal control and support structures can also be added. Generalizing this model to more complex geometries is possible, and only requires more careful preparation of the CAD model and the correct numbering of the weld parts so their order reflects their position in the weld sequence. The custom APDL code can also accommodate more complex geometries with slight changes to how heating of the weld parts is calculated.

At present, the model implementation workflow is optimized for hollow thin-walled cylinders of any dimensions in standard atmosphere laboratory conditions and in orbit.

Post-processing of the simulation results requires an additional Ansys job to be run, mostly due to the large size of the result files, which are often larger than 200 GB, and the proprietary file extension of the result files. Extraction of temperature histories from specific parts of the model must be defined in the post-processor APDL code, and the results are saved to CSV files for further analysis.

3.4.3. Efficiency and Validation

The model is at present not optimized for computational efficiency, with preliminary results showing that a simulation of 8000 seconds takes more than 24 hours to complete on 64 CPU cores. This is likely due to the addition of surface thermal effects like convection and radiation, which require a significant amount of computational power to calculate. Preliminary experiments showed that a minimum element size of 5x3x0.7 mm for the weld part elements was required to avoid convergence errors, although an improvement in the definition of nodal temperature constraint logic could remove this lower bound for solver speed. It must be noted that an increase in geometry (and thus mesh) size increases the computational time more than linearly, requiring a significant increase in computational power or solver time for even modest increases in geometry size. Figure 3.23 shows how the time taken per step increases with the active geometry during solution.

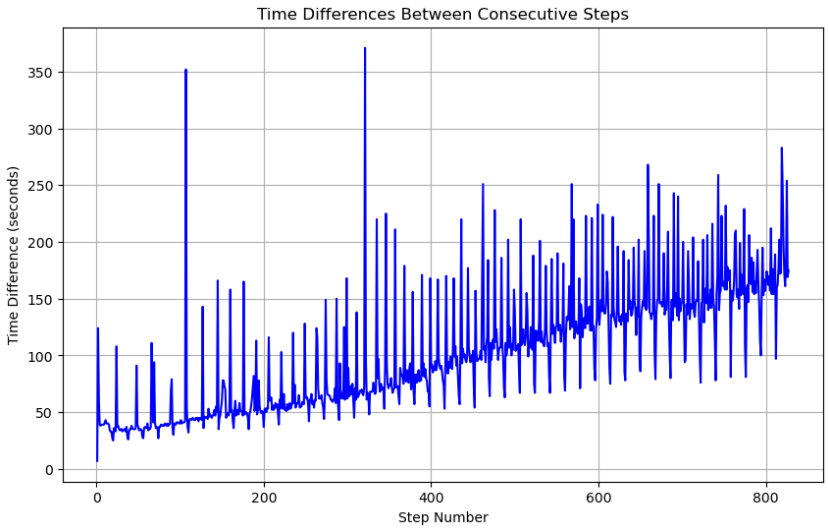


Figure 3.23: Sample solution speed for a large lab model simulation on 64 CPU cores

Validation involves comparing simulation results with experimental data, particularly for convective heat transfer coefficients. With this in mind, several laboratory experiments are defined in the following chapter to validate the model using the corresponding boundary conditions, as defined in Subsection 3.3.3. Once validated, the model can be used to predict thermal histories for orbital conditions.

4
Material and Experiments

4.1. Feedstock and Experimental Setup

5 different welding experiments were conducted over the course of this research with the aim of progressively characterizing the feedstock, the process applying the feedstock, and the thermal properties of deposited parts to use for further simulations.

These five tests are:

1. Initial weldability tests
2. Additive manufacturing feasibility tests
3. Weld parameter optimization tests
4. Convective heat transfer coefficient validation
5. Large geometry (representative for orbital applications) with pre-heating

These tests will be discussed in this chapter, along the methods used to characterize the deposited workpieces with microscopy and mechanical testing.

4.1.1. Material Properties

A 1.2 mm diameter Al 5183+0.3% Sc solid wire from Hunan Oriental Scandium was selected as welding feedstock due to its availability and potential space applications [75]. The composition of the wire is given in Table 4.1.

Table 4.1: Chemical composition of the selected Al-5183+0.3% Sc alloy - Al wt. % is balanced to 100%

Element	wt. %	Element	wt. %
Mg	4.73	Fe	0.0057
Mn	0.65	Si	0.040
Sc	0.30	Cu	0.0037
Ti	0.041	Zn	0.0057
Cr	0.077	Be	0.0049

Certain material properties at evaluated temperatures were supplied by Hunan Oriental Scandium, and are given in Table 4.2. The values of the thermal conductivity in the liquid phase past 600 °C were estimated using similar values for Al-5182 from the literature [76].

Table 4.2: Mean thermal properties of the selected material at various temperatures

Temperature °C	**Conductivity (W/(m K))**	**C_p (J/(kg K))**
25.3	83.039	827
100.0	98.163	900
300.0	121.267	971
500.0	131.625	1001
600.0	60.5	1001

The small lab experiment used a Al-6082 baseplate, while the large experiment used a Al-6060 baseplate. The material properties of Al-6082 are given in Table 4.3 and Table 4.3, while the material properties of Al-6060 are given in Table 4.4 and Table 4.6.

Table 4.3: Chemical composition of Al-6082 - Al wt. % is balanced to 100%

Element	wt. %	**Element**	wt. %
Silicon (Si)	0.7 - 1.3	Iron (Fe)	0.0 - 0.5
Copper (Cu)	0.0 - 0.1	Manganese (Mn)	0.4 - 1.0
Magnesium (Mg)	0.6 - 1.2	Chromium (Cr)	0.0 - 0.25
Zinc (Zn)	0.0 - 0.2	Titanium (Ti)	0.0 - 0.1

Table 4.4: Chemical composition of Al-6060 - Al wt. % is balanced to 100%

Element	wt. %	**Element**	wt. %
Silicon (Si)	0.2 - 0.6	Iron (Fe)	0.1 - 0.5
Copper (Cu)	0.1 - 0.3	Manganese (Mn)	0.1 - 0.5
Magnesium (Mg)	0.45 - 0.9	Chromium (Cr)	0.05 - 0.25
Zinc (Zn)	0.1 - 0.2	Titanium (Ti)	0.1 max
Others	Each 0.05 max, total 0.15 max		

The thermal properties of Al-6082 and Al-6060 are given in Table 4.5 and Table 4.5, and Table 4.4 and Table 4.6, respectively. These values were obtained partially from the Ansys material library, and partially from the literature [76] by estimating Al-6060 values from Al-6061-T6 data.

Table 4.5: Material properties of Al-6082

Property	**23°C**
Density (kg/m^3)	2700
Thermal Conductivity (W/(m·C))	172
Specific Heat (J/(kg·C))	899.8

Table 4.6: Material properties of Al-6060

Property	**23°C**	**100°C**	**200°C**	**300°C**	**400°C**	**500°C**	**600°C**
Density (kg/m^3)	2713	2713	2713	2713	2713	2713	2713
Thermal Conductivity (W/(m·C))	190	195	203	211	212	225	200
Specific Heat (J/(kg·C))	924.3	987.8	1035	1078.7	1118	1168	1190

The thermo-optical properties of the selected materials are given in Table 4.7, based on the literature [77]. The emissivity of the deposited feedstock was multiplied by 0.2 to account for the higher surface roughness and increased surface area.

Table 4.7: Thermo-optical properties of the selected materials

Material	**Emissivity**	**Absorptivity**
Feedstock	0.2	0.2
Al-6082	0.1	0.2
Al-6060	0.1	0.2

4.1.2. Experimental Hardware

All experimental work was conducted at RAMLAB, an additive manufacturing research company in the Netherlands. The robots used were Panasonic TAWERS® TM-1400 WGIII 6 DOF robotic arms with an

attached welding torch, while the support structures for the tests were a 3 DOF manipulator and a static welding table. All weld experiments used Alumaxx Plus ® (30 % Helium in Argon) as a shielding gas, delivered at a flow rate of 20 liters per minute.

The welding power sources employed Panasonic's Active Wire (AW-P) method [19], which operates using direct current (DC) welding. AW-P is a pulsed welding method where the wire is moved toward and away from the melt pool at a high frequency by alternating the wire feed speed, as shown in Figure 4.1, creating a periodic contact arc and reducing the total required heat input. In general for MIG welding of Aluminium, an AC welding power source needs to be used [17]. AC welding provides a natural cleaning action due to the alternating polarity. This helps to remove the Aluminium oxide layer that forms on the surface of Aluminium, which can inhibit proper fusion during welding. For this research, a DC^+ power source was used to enable the use of AW-P, the combination of which is at present not reported in the literature.

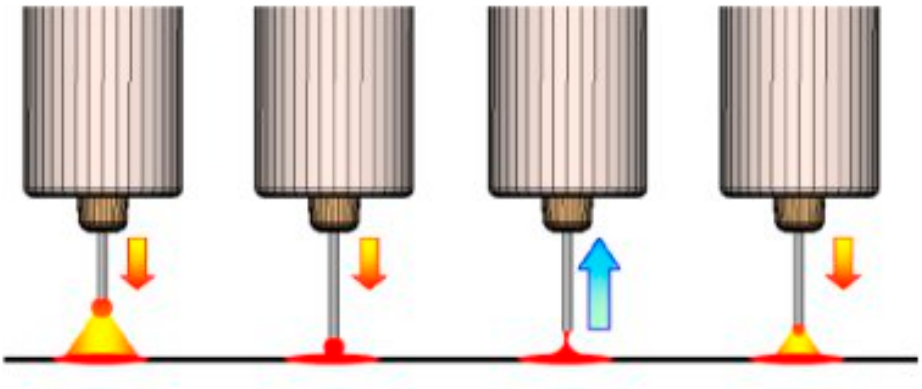


Figure 4.1: Panasonic AW-P welding power source wire movement pattern [19]

4.1.3. Weldability, AM Feasibility, and Parameter Optimization Tests

The weldability of the chosen feedstock must first be investigated with these new welding conditions using single bead-on-plate deposition. To further test if this welding program is suitable for additive manufacturing, subsequent overlapping and overlapping layers were deposited.

This process was conducted using a small Al-6060 baseplate, which served as the substrate for the welding tests.

The welding conditions used for this initial test are given in Table 4.8. The current and voltage are given as averages, since the actual measured values fluctuate due to the pulsed contact of the wire with the substrate which AW-P creates. The wire feed speed was not retrievable from the welding power source as it is set programmatically by the welding controller.

Table 4.8: Initial welding parameters

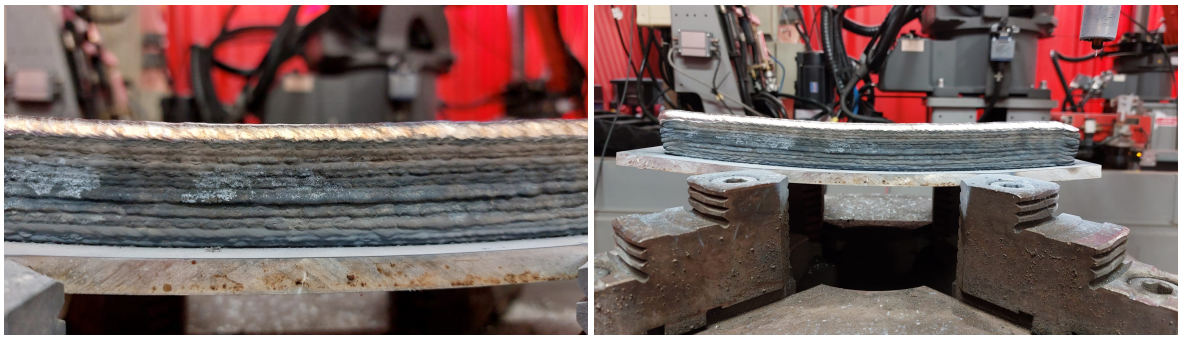
Parameter	Value
Average Current (A)	145
Average Voltage (V)	17.8
Travel Speed (m/min)	0.48
CTWD (mm)	15
Crater Current (A)	60
Crater Voltage (V)	12.9
Crater Time (s)	0.3

The single bead and overlap bead test results are given in Figure 4.2a, while the overlap bead wall test results are given in Figure 4.2b, and the single bead wall test results are given in Figure 4.3a. The stepover distance was 5 mm, and the step up distance was 2 mm.



(a) (b)

Figure 4.2: Initial results of weldability tests. (a) Initial single and overlap bead tests. (b) Initial overlap bead wall tests.



(a) (b)

Figure 4.3: Initial single bead wall test results. (a) Initial single bead wall depositions. (b) Initial single bead wall baseplate deformation.

The accumulated stresses in the baseplate, which was only secured by two clamps in the XY plane, causing deformation are clearly visible in Figure 4.3b. It is a interesting aspect for further research, however it is not the focus of the current work, hence only observations were made here.

The weldability experiments show that it is possible to weld this material using DC^+ AW-P. The criteria for evaluating weldability are: a stable weld bead deposition (no interruptions in the bead), adequate and complete fusion with the substrate (no microcracking at the baseplate interface), and a consistent weld bead shape.

For additive manufacturing, however, a more optimized bead shape is required, so further optimization of the welding parameters was conducted. The "weaving" weld tip movement pattern, also used in these tests, refers to the movement of the welding torch in both lateral (side-to-side) and longitudinal (backward-and-forward) directions while progressing along the weld path.

The initial test beads produced during the optimization process are illustrated in Figure 4.4, which depicts the progression of the welding parameters from right to left. The optimal process conditions were found and listed in Table 4.9. These conditions were used for all subsequent weld experiments.

The optimality of the weld bead in these tests was evaluated by the ratio of the bead width and height, which should be between 4 and 5 [18]. This is because wider beads ensure good layer adhesion and prevent defects, since if beads are too high and narrow, this may introduce imperfect fusion and gaps, as well as concentrating the heat from the bead in a narrower region. The parameters that were iterated on were the current, voltage, and travel speed to control the amount of feedstock deposited per travelled unit length and linear heat input. Higher heat input causes more bead spreading, while more material deposited per unit length causes a higher bead height [18]. Additionally, the weaving pattern lateral travel distance was gradually increased, as it directly affects the bead width.



Figure 4.4: Initial test beads for weld parameter optimization, progressing from right to left

Table 4.9: Final optimized welding parameters

Parameter	Value
Current (A)	125
Voltage (V)	19.8
Travel Speed (m/min)	0.45
Stickout (mm)	15
Crater Current (A)	80
Crater Voltage (V)	15.5
Crater Time (s)	0.3
Weaving Frequency (Hz)	2
Weaving Motion Distribution	25% front, 75% back
Lateral Travel (mm)	4

4.2. Model Validation Tests

Two welding tests were conducted to validate the thermal simulation model. The first test was a small cylinder model, which was used to validate the convective heat transfer coefficients, and the second was a large cylinder model, which was used to validate other initial conditions for the simulation. Welding and thermal simulation thereof have dozens of degrees of freedom, so progressively removing uncertainty for given parameters was the rationale for this approach.

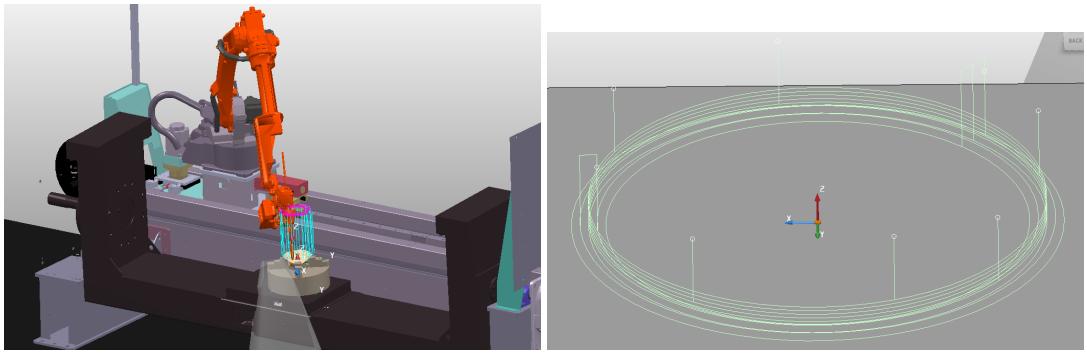
4.2.1. Toolpath Generation

The geometries described in Subsection 3.2.2 were used as inputs for the robot toolpath creation.

The described workflow is particular to RAMLAB and may not apply to all metal 3D printing setups. The exported STEP file is first imported into Autodesk Powershape, where the workpiece is placed on a different conceptual "layer" of the assembly as the baseplate. This segmented geometry is then exported to Autodesk Powermill for toolpath generation.

Autodesk Powermill is a CAM software package that can generate toolpaths from geometries specifically designed for additive manufacturing. Instead of manually defining the toolpaths, the shape of the workpiece is sliced into layers, and the toolpaths are generated for each layer, which is necessary for complex geometries. In this case, the geometry is quite simple, allowing for a more manual approach. The thin walls of the cylinder are assumed to be thick enough to require only a single weld bead, while the tapered region at the baseplate interface is defined two modified layers, where the first one is a

3-bead overlap, and the second a 2-bead overlap coinciding with the gaps between the first layer's beads. The rest of the geometry is then printed on top of this tapered region.



(a) (b)

Figure 4.5: Toolpath generation in Powermill. (a) RAMLAB welding robot setup in Powermill. (b) Sample of the initial layers of a representative toolpath generated in Powermill.

The robot being used for the experiment needs to be 3D modeled (although this work was already done by the RAMLAB team), and imported into the simulation to simulate all the joint movements during printing. During the simulation, the software checks for collisions between the robot and the workpiece and joint singularities, and the toolpaths are adjusted to avoid these collisions. The resulting joint movements are then exported to the robot controller, which executes the toolpaths.

4.2.2. Convective Heat Transfer Coefficient Validation

In order to validate the convective heat transfer coefficients for the larger thermal model, an initial experiment was performed to test these assumptions against thermocouple thermal results. This test also served the purpose of evaluating the feedstock's performance given more complex geometries and single bead walls.

The sequence of layers deposited did not have a consistent inter-layer cooling period because RAMLAB's Max-Q thermal analysis and 3D geometry scanning was used. Two thermocouples were attached to the base plate using spot welding, as shown in Figure 4.6, in order to capture the thermal profile of the baseplate further and closer to the weld heat source. Taking the center of the ring at the baseplate as the origin, the thermocouples were placed at (0,-59,-5.25) and (101.5,11,0) mm. The thermocouples were connected to a PicoLog data collector, which was then connected to a laptop recording the data. The base plate was clamped to the manipulator with four clamps acting in the XY plane only. The welding parameters were taken from the optimized weld parameters described in Table 4.9. The toolpath created for this geometry included the use of a tapered region near the bottom of the weld, which spread out the thermal stresses on the base plate.

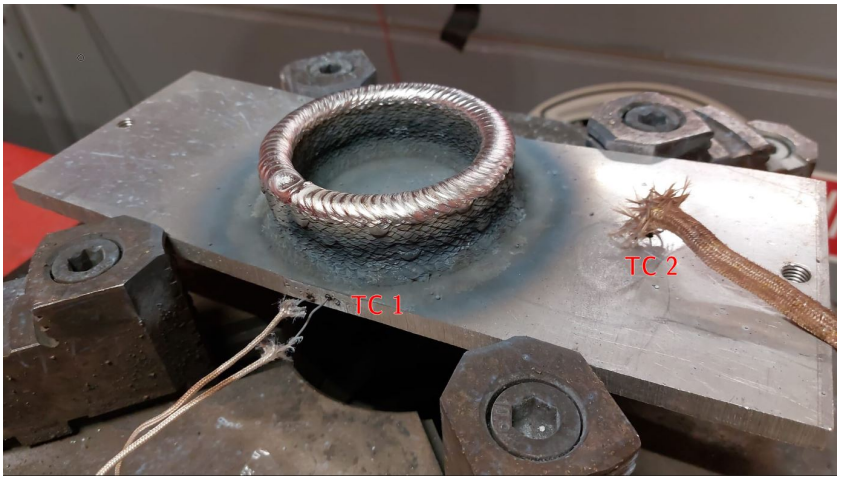


Figure 4.6: Final printed geometry of the validation experiment

As can be seen in Figure 4.6, the deposition of this geometry was successful without any major distortions, failures or irregular features: no clear gaps in the weld beads were present, the surface of the walls had uniform features, and the thickness of the walls along the circumference of the cylinder was consistent. The final dimensions of the printed geometry, as shown in Table 4.10, was a roughly good match to the dimensions of the expected toolpath used in Powermill to model the geometry, with the thickness of the walls slightly exceeding the expectations set by the initial single bead wall tests (Figure 4.3a), which had a thickness of 11.25 mm. This was expected, as this previous test was not using the optimized welding parameters or the weaving deposition pattern, which increased the bead width.

Table 4.10: Dimensions of the printed convection test geometry

Thickness	**14.25 mm**
Radius	**45 mm**
Height	**30 mm**
Average Layer Height	**1.44 mm**

Figure 4.7 shows the surface features of the printed part, which can be seen to be quite wavy and rough, increasing the apparent surface area of the workpiece significantly. This is partly a result of the weaving method used during welding, which can cause feedstock to flow over the top of the previous layer, creating a wavy surface. Whether this poses an issue for the intended orbital application is yet unknown due to the possibility of such overflows not occurring in microgravity conditions, which should be investigated in future work. Surface roughness for a final ISAM structure would likely be undesirable due to interfaces with other layers added to the exterior and interior of the pressure vessel, and such features would need to be machined down to a smooth finish.

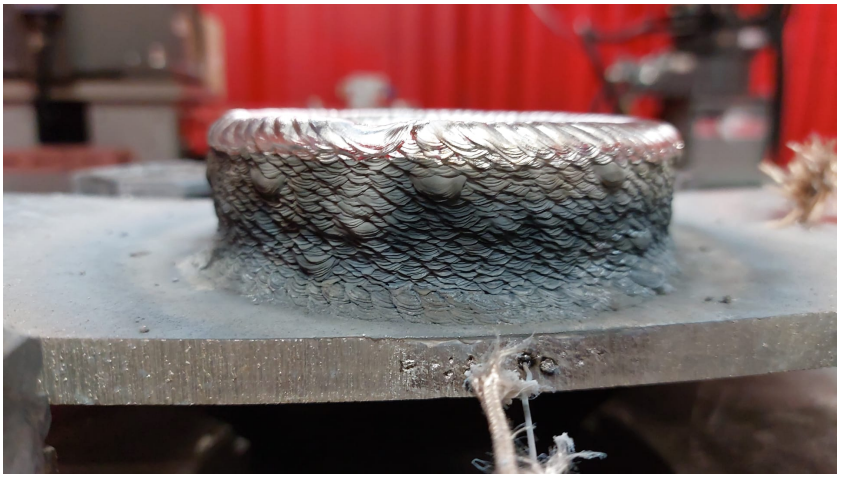


Figure 4.7: Surface features of the printed part

Although the reduction method through tapering the geometry at the workpiece-baseplate interface was used, there was still a noticeable deformation of the baseplate in the Z direction, as shown in Figure 4.8. This was due to the clamping only occurring in the XY plane and allowing the baseplate to deform in the Z direction relatively freely through frictional sliding. The effects of this deformation on the welding process, which could be negatively affected due to the change in stick-out distance between the welding tip and the workpiece, was mitigated by the use of 3D geometry scanning between layers, which corrected the toolpath and projected it onto the currently existing geometry, thus avoiding deformations and geometric mistakes.



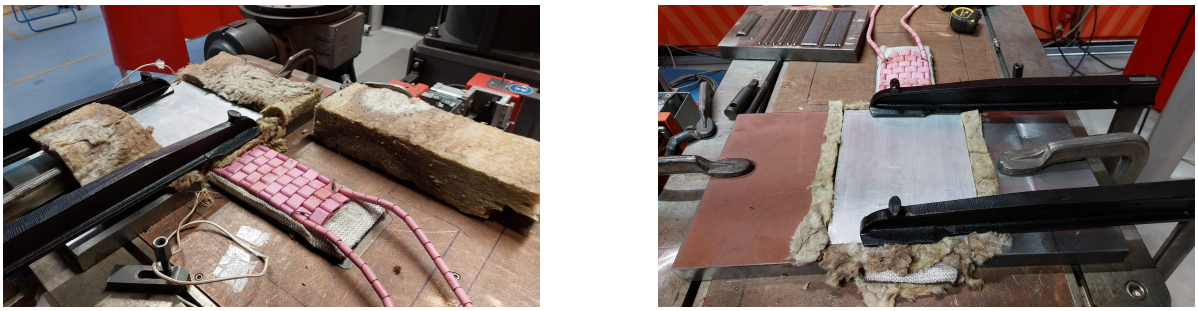
Figure 4.8: Deformation of the baseplate in the Z direction

4.2.3. Large Cylinder Model Validation Test

For this test, the large geometry shown in Figure 3.3b and detailed in Table 3.2 was printed. This was the main experiment of the research, attempting to approximate the thermal profile of ISAM conditions by using pre-heating and thermal insulation to raise the average temperature of the workpiece during printing. The choice of these high-temperature conditions was based on the assumption that the workpiece would be hotter during printing in orbit than under normal Earth conditions due to the lower heat loss rates.

The baseplate utilized was composed of Al-6060-T6 and was positioned on two steel base plates, as illustrated in Figure 4.9b. These two base plates were clamped to a fixed table, along with the main baseplate. This configuration elevated the main baseplate to accommodate the heater, as shown in

Figure 4.9a, which was a 60V Globeheat FIP3 Flexible Insulated Preheater using ceramic beads as heating elements with a power rating of 2.7 kW and a maximum temperature of 250 °C. The heating unit was a Globeheat 10.5 kW Inverter Power Source.



(a) (b)

Figure 4.9: Large welding test experimental setup. (a) Placement of heater under baseplate. (b) Baseplate support structure.

Fiberwool insulation was placed under the baseplate beside the heater, as well as along the sides of the main baseplate and, to the extent possible, covering most of the supporting structures in order to avoid heat loss through conduction, as shown in Figure 4.10a. Four thermocouples were placed on the main baseplate as shown in Figure 4.10a, along with a 5th one connected to the heating unit in order to stop heating once the maximum temperature was achieved. These thermocouples were added to measure the temperature of the baseplate in several different locations in order to find a likely average for the entire baseplate.

Figure 4.10b shows the entire data collection setup, including connection to the PicoLog thermocouple data logger. This figure also shows the setup in the preheating phase, during which the baseplate and accompanying support structures were preheated to 250 °C for a total of 4 hours.



(a) (b)

Figure 4.10: Large welding test setup. (a) Fiber wool insulation and thermocouple placement. (b) Thermocouple data collection setup in preheating phase

During the printing process, the same weld parameters as before were used, as described in Table 4.9. The printing program created used 60 seconds between layers at 250 °C preheating temperature. This was done in order to get the hottest possible print without causing defects. Additionally, there were intermediary steps between layers that the robot had to conduct which took around 40 seconds, creating a lower limit on the possible interlayer time.

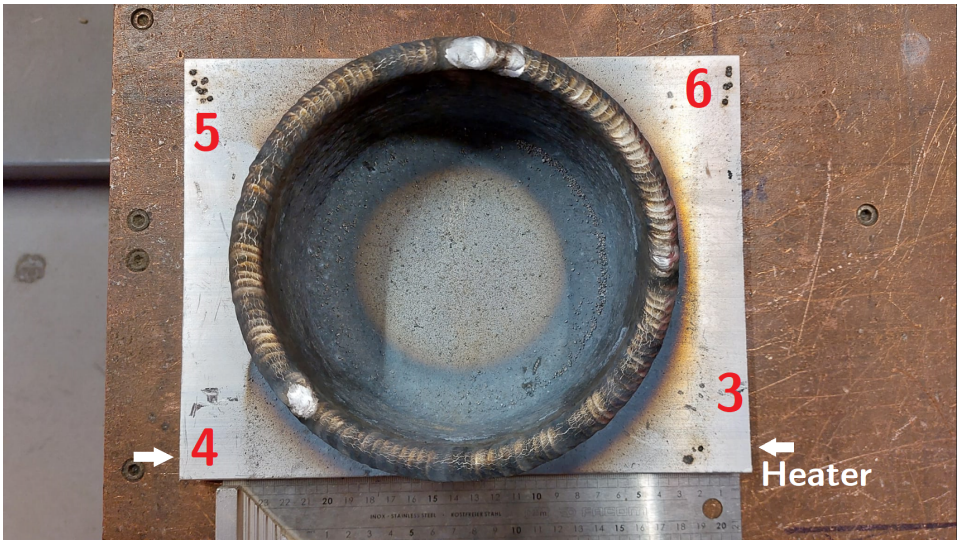


Figure 4.11: Final printed cylinder dimensions and thermocouple placement

The final printed cylinder is shown in Figure 4.11, with an added ruler for scale, with the dimensions shown in Table 4.11. These dimensions were measured using a caliper accurate to 0.01 mm. Also visible are the numbers of the thermocouples used, from 3 to 6, along with the position of the heater control thermocouple on the bottom right (on the side of the baseplate).

Table 4.11: Dimensions of the printed large cylinder

Parameter	Value
Cylinder height	70.1 mm
Layers deposited	52
Layer height	1.346 mm
Cylinder radius	79.8 mm
Wall thickness	14.25 mm

As can be seen in Figure 4.12a, the surface of the workpiece is quite rough and wavy, which is likely due to the weaving method used during welding. This method causes the feedstock to flow over the top of the previous layer, creating a wavy surface. Figure 4.12b shows the surface of the workpiece with a close-up of the cracks in the soot layer on the top of the bead. These cracks are likely due to the high thermal gradients at the top of the current weld bead, which causes the soot on the surface to crack and peel off. This soot is easily removed with a metal brush, and would thus require extra post-processing for the final ISAM structure.



(a) **(b)**

Figure 4.12: Surface characteristics of the printed cylinder. (a) Rough and wavy wall surface. (b) Surface deposition cracks on bead top

The workpiece was then allowed to cool slowly to room temperature, and the insulation was removed after an entire night of cooling.

4.3. Material Characterization

Concluding the welding portion of the research, the printed workpiece from the large cylinder validation test was analysed using several different techniques to understand the material properties and microstructure of parts printed under high-temperature conditions. These techniques included optical and scanning electron microscopy and yield strength analysis.

With this analysis, the question to be answered is how the properties of orbital structures printed under comparable conditions to those in the lab are affected by the high-temperature conditions.

4.3.1. Metallurgical Analysis Equipment

After printing, the workpiece was cut into sections, and a sample was cut from the top of the wall for microscopy analysis. The surface sample was mounted in a cylinder of conductive resin, and progressively sanded from a grit coarseness of 180 microns to 10 microns, after which it was polished with an emulsion of 3 and 1 micron diamond particles in order to remove any rough finishing and remaining scratches that could affect the image quality from microscopy.

Optical microscopy was performed using a VHX-7100 microscope with a range of magnification lenses, with the objective of finding any cracks, defects, and grain boundaries in the microstructure of the material. To complement the optical microscopy analysis, scanning electron microscopy (SEM) was performed on the sample using a JSM-IT100 microscope, with the objective of performing Energy Dispersive X-ray spectroscopy (EDS) to identify the presence of different elements in the sample in different regions. Understanding the spatial distribution of alloying element concentrations would assist in identifying the presence of different phases in the material, which is important for understanding the material properties and microstructure of the workpiece.

4.3.2. Etching Techniques

Etching, in the context of metallographic microscopy, is the process of chemically removing the top layer of a sample to reveal the underlying layers. This is done to reveal the microstructure of the sample, and to remove any surface layers that may have been affected by the polishing process.

The main reference used for this process was the book "Metallographic Etching" by Günter Petzow [78].

An appropriate etchant for 5000-series Al-Mg alloys, specifically meant to reveal grain boundaries in alloys susceptible to intercrystalline corrosion and reveal Al-Mg intermetallic phases, was found: a 8.2% solution of phosphoric acid in distilled water, applied for 30 minutes at 20 ° C. Initial attempts at following the prescribed procedure did not reveal enough of the grain boundaries to be useful even after 1.5 hours of etching, and so the concentration of the phosphoric acid was doubled to 16.4%. Even at these higher concentrations, significant etching time was required to reveal the grain boundaries, and so the etchant was left to sit on the sample for a total of 2 hours.

Considering this deviation from expected outcomes, it is possible that for the specific alloy used in this research, given the inclusion of 0.3% Scandium, another etchant may have been more appropriate, which should be investigated in future work.

4.3.3. Mechanical Testing

Yield tensile tests were performed by Element Materials Technology Inc., a testing laboratory services provider. The yield test was performed according to ISO 6892-1 (A224) [79], which specifies the procedure for tensile testing of metallic materials at room temperature. The testing equipment used was a Zwick Z100 Allround table top together with a MultiXtens extensometer.

Hardness tests were performed using a Struers Durascan hardness tester. The sample used was the same one as for the microscopy analysis, polished to 3 μm. HV0.2 was measure along the build direction in a zigzag pattern shown in Figure 4.13. The y-axis distance between points was 0.1 mm, while the distance between the lines was 0.5 mm.

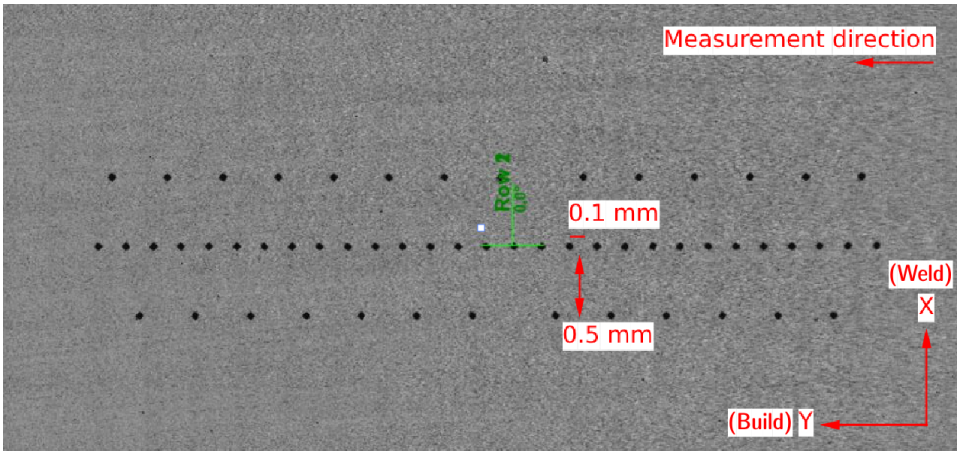


Figure 4.13: Position of the hardness test point zigzag pattern

4.3.4. Test Sample Design

ISO 6892-1 (A224) [79] specifies the design of the test samples for various different cases and geometries. The particular sample geometry used in this test is shown in Figure 4.14. The diameters of the test samples were set to 6 mm in order to allow the samples to be extracted from the printed workpiece in both longitudinal (Z axis) and transverse (XY planes) directions, with the other dimensions of the samples being shown in Table 4.12.

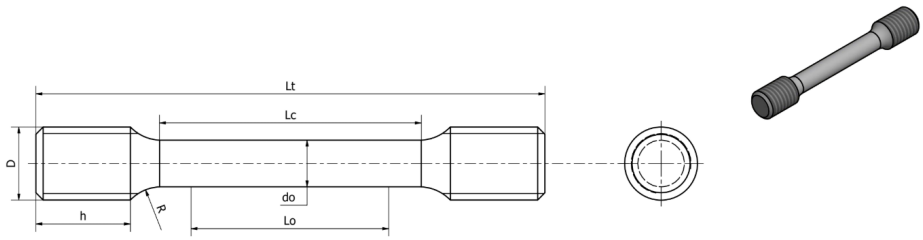


Figure 4.14: Drawing of the geometry for threaded round cross-section yield test samples according to ISO 6892-1 (A224), along with design rules to apply

Table 4.12: Table of the dimensions and tolerances for the test sample geometry (mm)

do	D	h	R (min)	Lt (approximate)	Lc (min)	Lo	Tolerance on nominal dimensions	Tolerance on shape
6	M 10	15	4,5	73	33,04	30,04	$\pm 0,02$	0

5
Results and Discussion

This chapter presents and analyzes the experimental and computational results obtained through this investigation. The validation of convective heat transfer coefficients is first examined, followed by a detailed analysis of the microstructural evolution and mechanical properties of the deposited material. Thermal modeling results under both terrestrial and orbital conditions are presented, with particular emphasis on their implications for In-Space Additive Manufacturing (ISAM). The chapter concludes with a comprehensive discussion of the thermal behavior of full-scale space habitats and proposes strategies for thermal management during manufacturing.

5.1. Convective Heat Transfer Coefficient Validation

As explained in Chapter 3, an Ansys geometry matching the experiment described in Section 4.2.2, as well as the final resulting welding profile and the correct interlayer cooling times, was created. A total of 16 different experiments using different convective heat transfer coefficients for the base plate and the workpiece were simulated. As shown in Figure 5.2, the simulation results showed a wide range of thermal profiles. The temperatures of the thermocouples were sampled from the thermal elements shown in Figure 5.1.

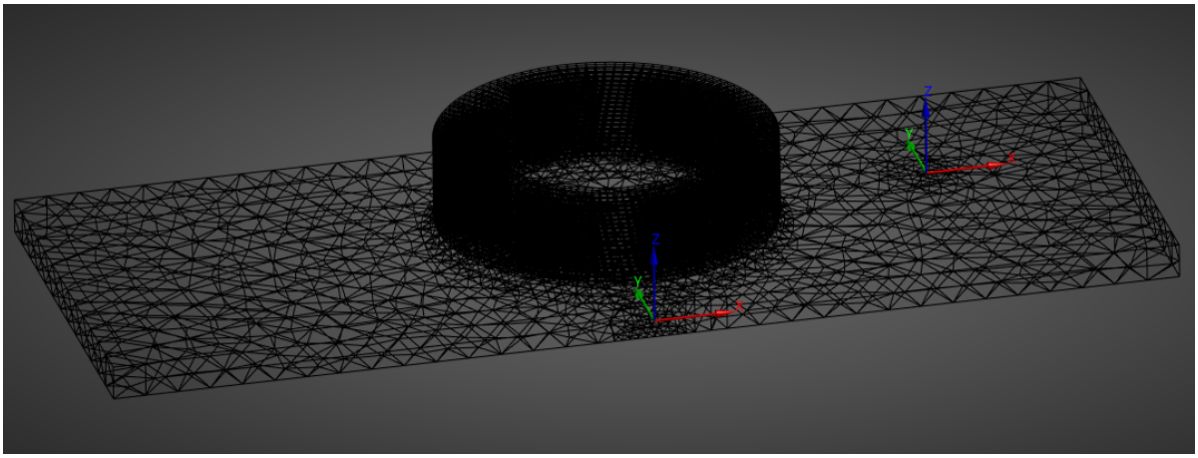


Figure 5.1: Thermocouple locations in the ANSYS model for the validation experiment

The mean absolute errors of the different trials, as well as the convective heat transfer coefficients and the ratio between the weld and baseplate convective coefficients are shown in Table 5.1. The mean absolute errors (MAE) of each trial was calculated as the average of the absolute differences between the simulated and measured thermocouple temperatures over the length of the solution.

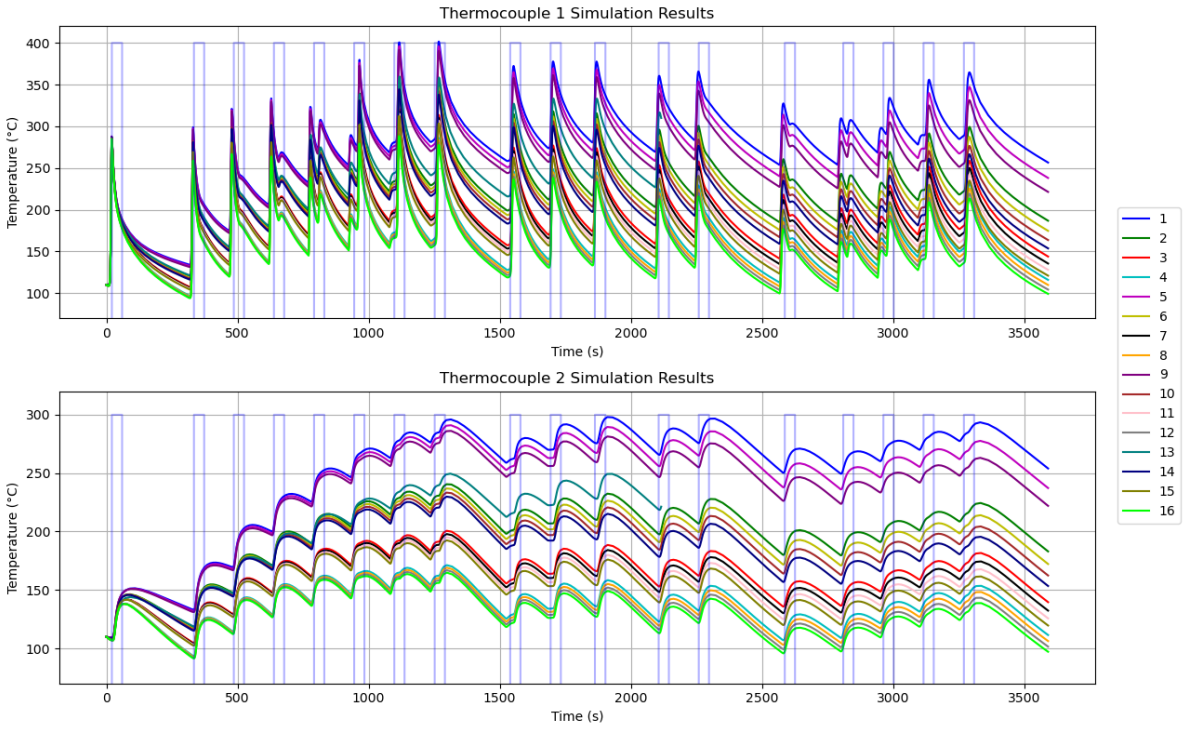


Figure 5.2: Simulation results for the validation experiment, details for each trial are shown in Table 5.1. Welding periods are shown in the light blue blocks.

Table 5.1: Mean Absolute Errors and Convective Coefficients (in W/m^2 K) for each trial in the validation experiment

Trial	MAE TC1	MAE TC2	Basplate h_c	Weld h_c	Weld/BP h_c
1	93.50	108.75	8	8	1.0000
2	44.28	57.43	13.7	8	0.5854
3	10.68	22.64	19.3	8	0.4138
4	13.05	1.74	25	8	0.3200
5	85.34	101.58	8	15.3	1.9167
6	38.51	52.50	13.7	15.3	1.1219
7	6.45	19.16	19.3	15.3	0.7931
8	16.27	4.31	25	15.3	0.6133
9	77.63	94.80	8	22.7	2.8333
10	33.05	47.84	13.7	22.7	1.6585
11	2.45	15.86	19.3	22.7	1.1724
12	19.33	6.75	25	22.7	0.9067
13	50.78	58.52	8	30	3.7500
14	27.91	43.45	13.7	30	2.1951
15	**1.33**	**12.73**	**19.3**	**30**	**1.5517**
16	22.24	9.07	25	30	1.2000

In order to select the combination of heat transfer coefficients that best models reality, two criteria were chosen. First, the lowest mean average errors for both thermocouples were preferred, but additionally a ratio of the weld-to-baseplate coefficients of around 2 was chosen as ideal in order to model the difference in apparent surface area for the workpiece. Trial 15 was chosen as the best result due to the combination of matching both of these criteria the best, with a very small error of 1.33 °C for the first thermocouple and 12.73 °C for the second thermocouple. The full thermal curve of this simulation is shown in Figure 5.3. As a note, it is important to add that in the literature, modeling thermal processes for welding usually accept a MAE of less than 50 °C to be sufficient for capturing the process accurately. Of note in the time series data is that for the first thermocouple, there was a slight phase difference in

the peaks of the curves, leading to small spikes in the local errors, which were still judged to be minimal and not affecting the descriptive power of the model.

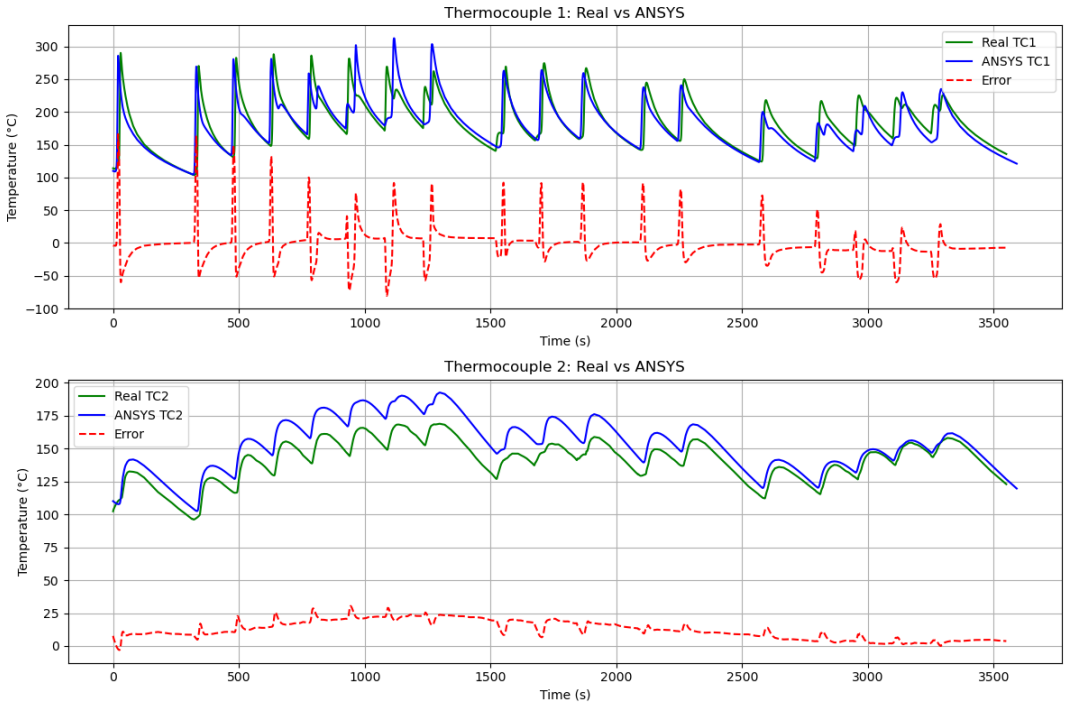


Figure 5.3: Temperature time series for the best performing simulation, Trial 15

5.2. Earth Conditions Model Validation

The thermocouple data is shown in Figure 5.4. The data is shown for the thermocouples from 3 to 6, as they were numbered in PicoLog, from the beginning of the first weld layer after the taper region was deposited (so the first two overlap layers). The average of all thermocouples is also shown, as well as a rolling average of the average thermocouple temperature to give a rough indication of the temperature of the baseplate. As can be seen, the temperature of the baseplate steadily declines from around 300 °C to 250 °C, likely due to the increasing distance between the deposited feedstock and the baseplate. However, it must be noted that the decline is relatively slow, likely due to the insulation used and the still-hot heating unit touching the bottom of the baseplate.

The average current and voltage for the process were slightly different than the weld parameters set for the experiment, at 111.41 A and 18.31 V, respectively. This might in part be due to the slight changes in CTWD between layers, but the difference in heat is small enough to be considered negligible. The average time between welds was 62.4 seconds.

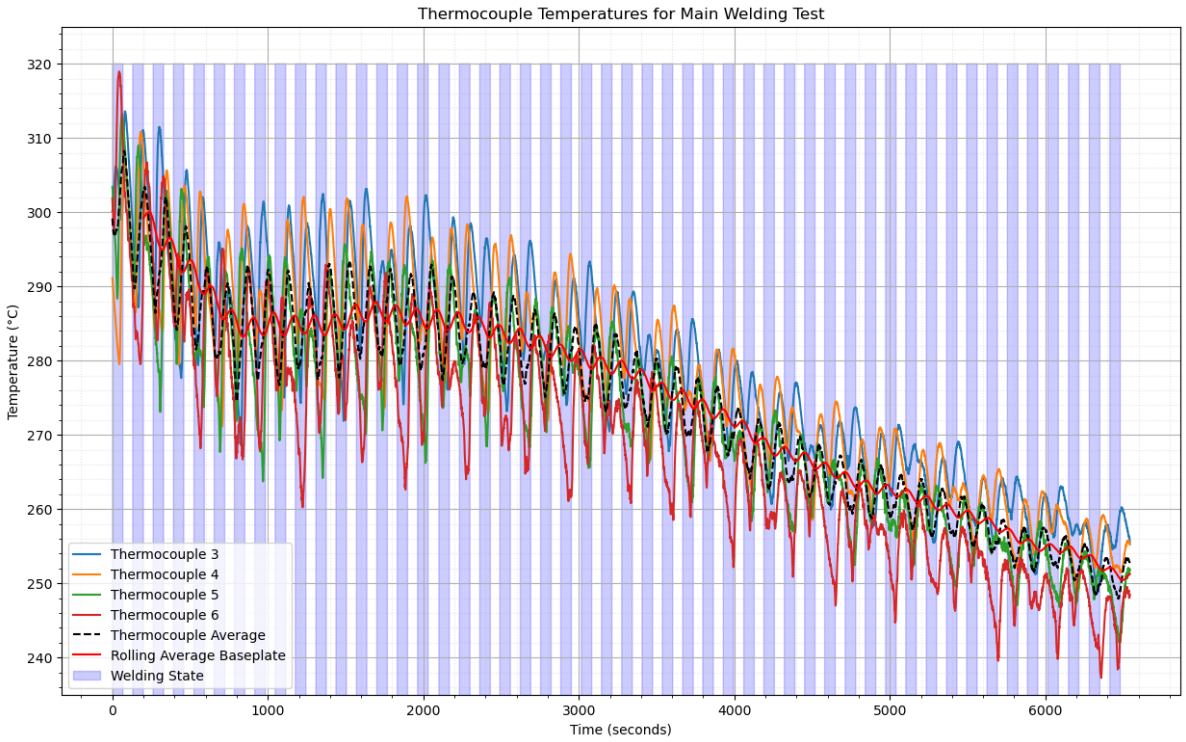


Figure 5.4: Thermocouple temperatures for the large welding test as a function of printing time

Figure 5.5 shows the results of the 6 different simulations replicating this experiment along with the root mean square errors (RMSE) for each simulation trial. The average of the measured thermocouple temperatures is plotted alongside the averages of the simulated thermocouple temperatures for each trial. Table 5.2 shows the conditions used for each trial. Trials 2 and 5 increased the convection of the baseplate by 20%, and trials 3 and 6 increased the convection of the baseplate by 50% in an attempt to capture the extra heat loss the baseplate experienced due to imperfect insulation and conduction to the support structures. Trial 6 has the lowest RMSE over the length of the solution, and thus the best fit. The timeseries of the simulated results are differeing lengths due to a limitation of simulation time, causing the data to be cut off at different times for each trial.

Table 5.2: Boundary Conditions and RMSE for different simulation trials for the large welding test

Trial	Feedstock Initial Temperature (°C)	Baseplate h_c (W/m^{2}K)	TC Average RMSE (°C)
1	300	19	16.3
2	300	22.8	18.34
3	300	28.5	16.3
4	600	19	8.38
5	600	22.8	6.78
6	600	28.5	4.78

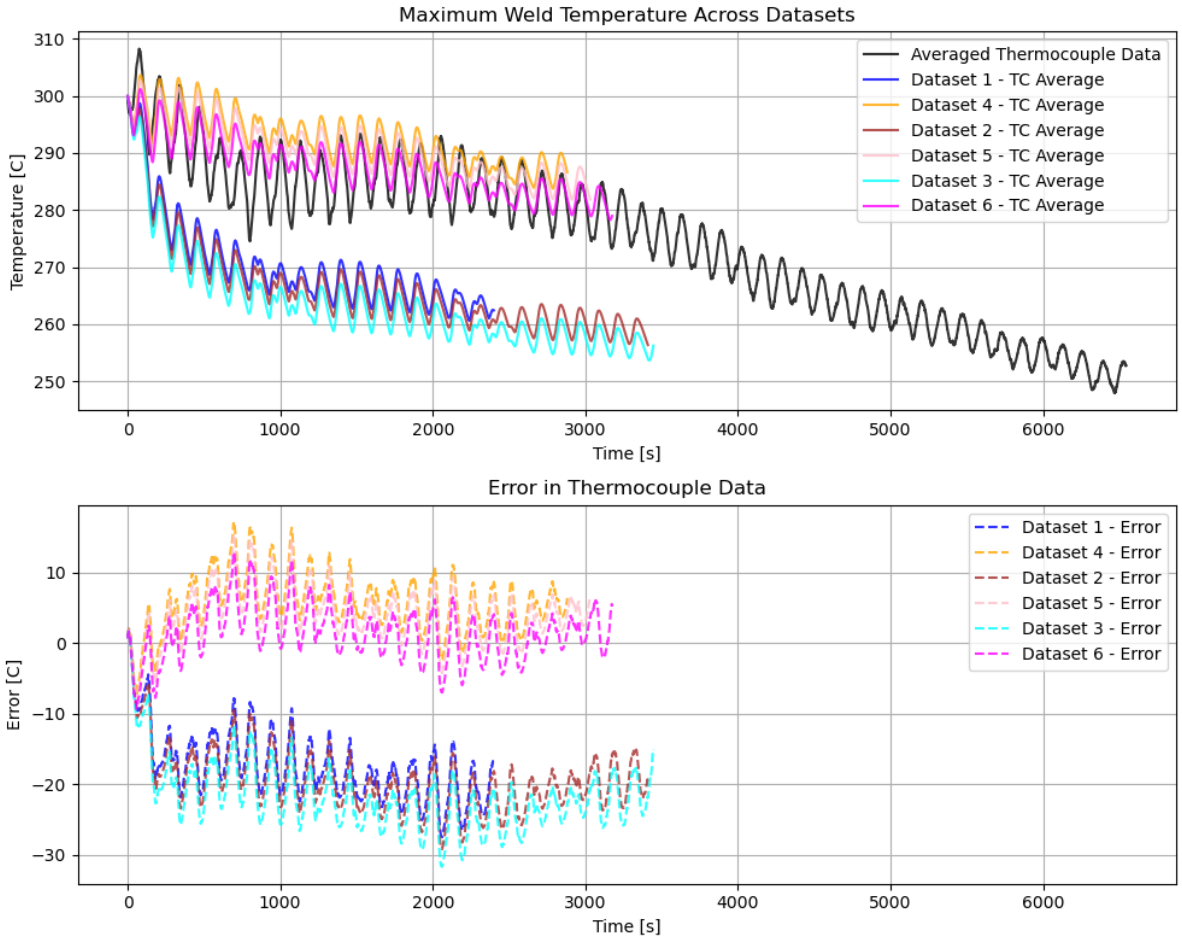


Figure 5.5: Simulation results for the large welding test

From the simulation results, it can be seen that trials 4, 5 and 6 were able to capture the general trend of the thermocouple temperatures, staying within an error bound of approximately 10 °C over the length of the solution. The feedstock temperature of these is also preferable due to the assumption of the molten wire starting contact with the workpiece at least at its melting temperature.

Figures 5.6 show the comparison of the individual real and simulated thermocouple temperatures. The simulated thermocouple temperatures were generated by sampling the average temperature of single thermal elements as closely located to the position of the thermocouples, as shown in Figure 5.7. It is apparent that thermocouples 5 and 6 show a larger thermal range between welding periods, while thermocouples 3 and 4 show much less thermal oscillation, although the average of these simulated results is in the correct range of the measured results. It is possible that the chosen thermal elements to sample the temperature from, for thermocouples 3 and 4, were too large or improperly placed, resulting in too much smoothing of the thermal curve. The average temperatures of these smoothed signals are not expected to vary significantly from the true values due to the close proximity of the simulated thermocouple elements to the actual thermocouple positions.

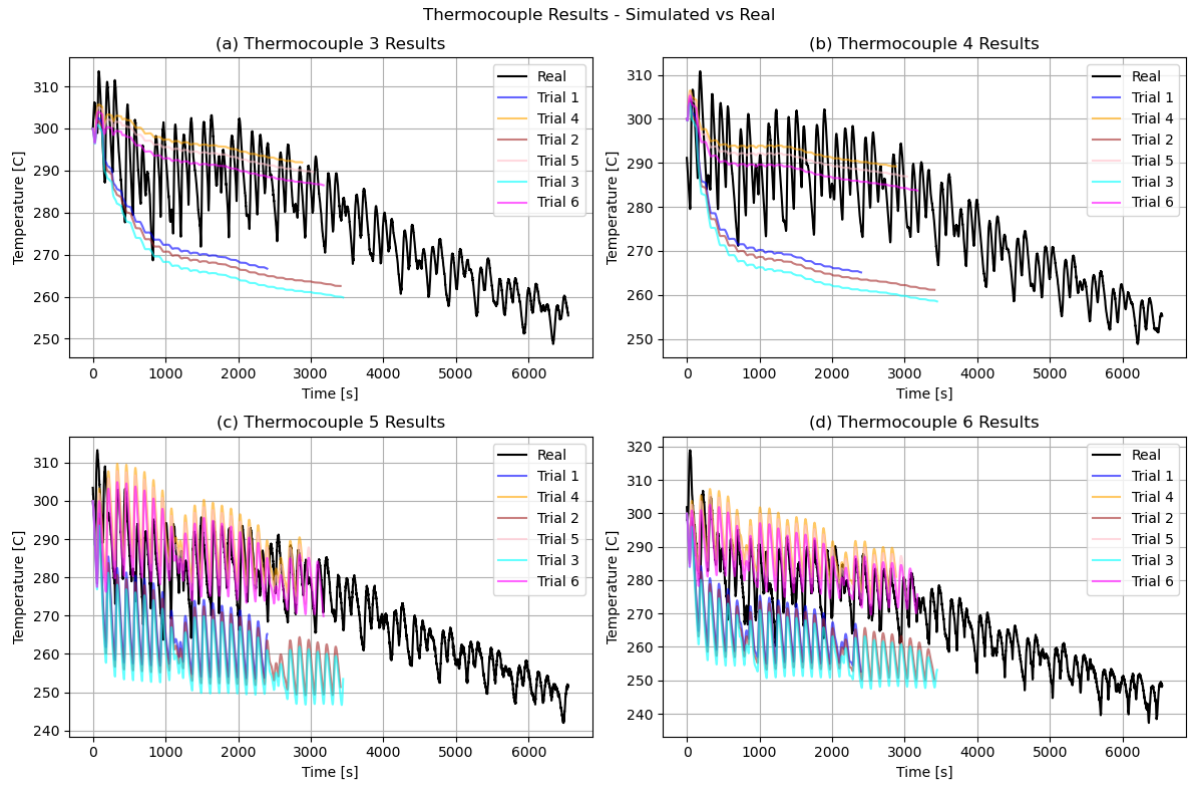


Figure 5.6: Thermocouple temperatures for thermocouples 3-6 (a-d) - comparison of measured and simulated results for the large welding test, thermocouple locations indicated in Figure 5.7

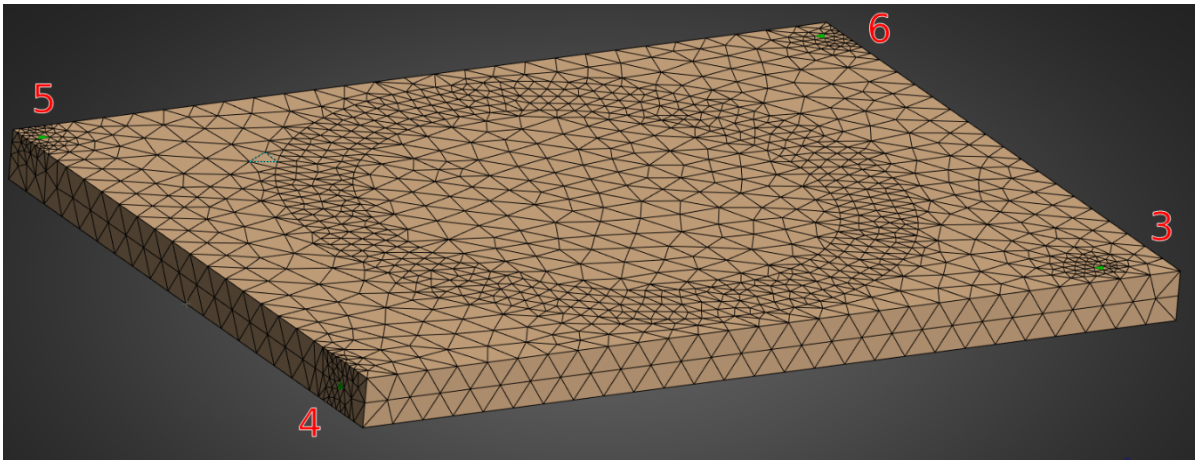


Figure 5.7: Thermal elements used to sample the temperature from for the thermocouples in the large welding test

The effect of the higher convective heat transfer coefficient of the baseplate can be seen to be negligible compared to that of the different feedstock temperatures. It can thus be concluded that the initially determined coefficients were correctly capturing the heat loss of the workpiece and baseplate, and that the increase in convective heat transfer could be modeled by refining the baseplate's other boundary conditions.

Figure 5.8 shows the full thermal profile of Trial 6, including the maximum, minimum, and average temperatures of the workpiece and baseplate, as well as the average surface temperature of the workpiece. The high-frequency oscillations in the maximum temperatures are the result of the discrete addition of new weld parts to the model, and would not be present in a fully continuous model. The second

subplot of Figure 5.8 shows the thermal fluxes from convection and radiation from the workpiece and baseplate. The maximum temperature of the workpiece does not exceed the melting temperature of the feedstock for the first layer, which is unrealistic. This behavior is likely due to the strong effect of the heater nodes acting as heat sinks at 250 °C, which is likely an overestimation of the actual temperature of the heater nodes. As the welding moves further from the baseplate, the maximum temperature settles at an oscillation between 600 and 800 °C, which is still an underestimation of the actual temperatures in the melt pool, which should be at least 1000-1500 °C [74]. This oscillation occurs due to the discrete nature of the weld parts as they are added to the model, since the heat in the previously active weld part is transferred to the new one, which starts at a lower temperature of 600 °C.

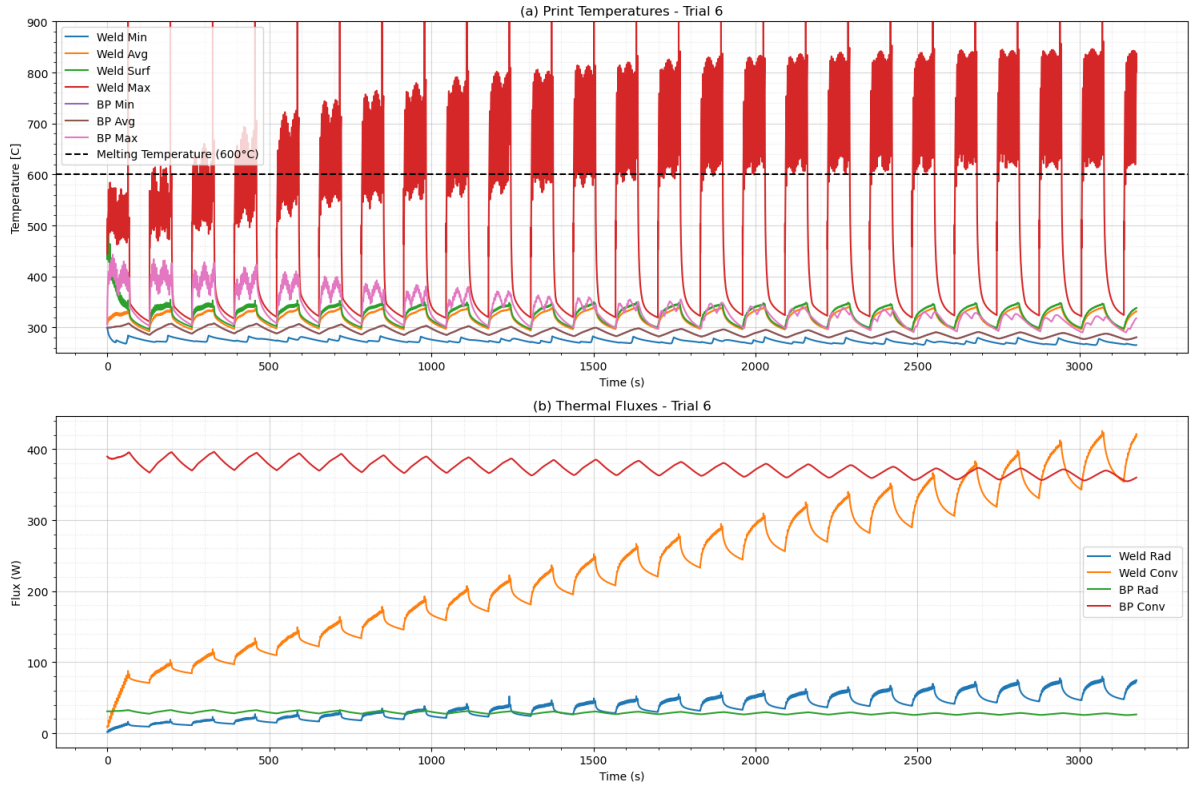


Figure 5.8: Full thermal profile of Trial 6. (a) Maximum, minimum, and average temperatures of the workpiece and baseplate, as well as the average surface temperature of the workpiece. (b) Thermal fluxes from convection and radiation from the workpiece and baseplate.

The boundary conditions of this model are a simplification of experimental conditions, and in order to improve the accuracy of the model, the main points for improvement are a more precise definition of the thermal interfaces with the support structures, which are currently assumed to be at the same temperature as the baseplate, and a more comprehensive modeling of the actual heat transfer on the sides and bottom of the baseplate, which still experience limited convection and conduction to the fiberglass insulation. Furthermore, the effect of the heater on the bottom of the baseplate is approximated as a row of nodes at a constant temperature of 250 °C, which is unlikely behavior for the actual heating unit. Thermally constrained nodes are a contentious strategy in Ansys because of their strong effect on the model's behaviour, since no real thermal element remains fixed without feedback and reciprocity. Furthermore, the definition of the convective heat transfer at the top of the currently active weld part, 40 W/mm^2K, was based on values in literature [80], but not verified experimentally. However, the convective coefficients of the workpiece and baseplate were found to be accurate for both the small and large models, and can thus be said to be validated. Further points of improvement lie in a finer division of the weld beads from 16 radial parts into 32 or more in order to more smoothly capture thermal evolution along the radius of the cylinder, allowing for a less jagged thermal profile.

Overall, due to the proximity of the simulated thermocouple results to the measured results, it can be

concluded that the thermal model is capable of predicting the averaged thermal history of the workpiece with accuracy sufficient for macro-scale predictions. This is usually defined in macro-scaled thermal modeling as a MAE of less than 50 °C [59], which is the case for the given results.

However, this model is not capable of fully approximating the temperatures in the melt pool. Thus, making microstructural predictions based on these maximum temperatures alone is not possible. It is possible that using a higher starting temperature for the feedstock would result in better melt pool accuracy, but this would also require an increase in the modeled heat loss at the baseplate to achieve realistic thermocouple temperature matching. The underestimation of melt pool temperatures is a not a defect of this model, but rather an inevitable consequence of using lumped-element heat sources in a welding simulation. The heat input from the welding process is usually concentrated in small region on the substrate (either the from electric arc in WAAM, electron beam in EBF3, or laser in LWDED). The discrete weld parts in this model are significantly larger than the region actually affected by the heat source, and thus the heat is spread out over a much larger volume than in reality. This leads to lower concentrations of heat, and thus a lower maximum temperature, meaning that such a model intrinsically cannot capture the accurate temperatures in the melt pool. The objective of this research was not to fully model the melt pool, and so the results achieved are within the scope of this work.

5.3. Microstructure Results

5.3.1. Microstructure for the Material

Previous research using Al-5183 in DED processes has shown that the microstructure of the material is heavily affected by the thermal gradient during printing. Dong et al. [81] investigated WAAM-deposited Al-5183 and found columnar grains within the weld beads, with grain refinement at the layers interfaces, as shown in Figure 5.9. Li et al. [82] conducted similar experiments found comparable results, shown in Figure 5.10a. Both experiments used CMT for heat input reduction, which is comparable to the AW-P process used in this study. Li et al. found grain sizes of 49.27 μm in the sample shown in Figure 5.10a, distributed roughly lognormally.

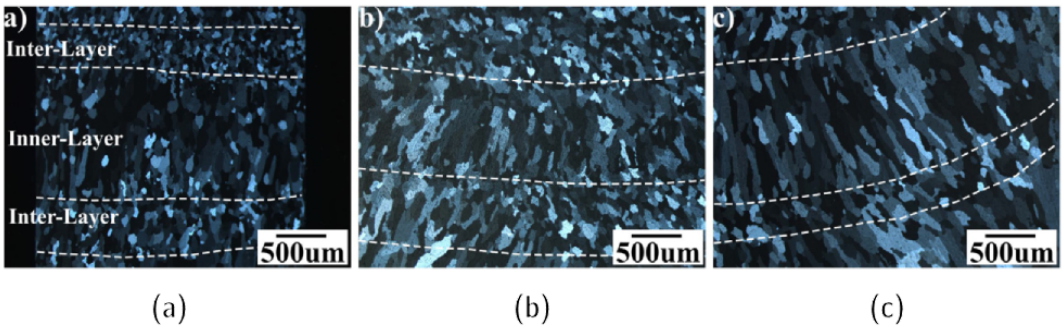
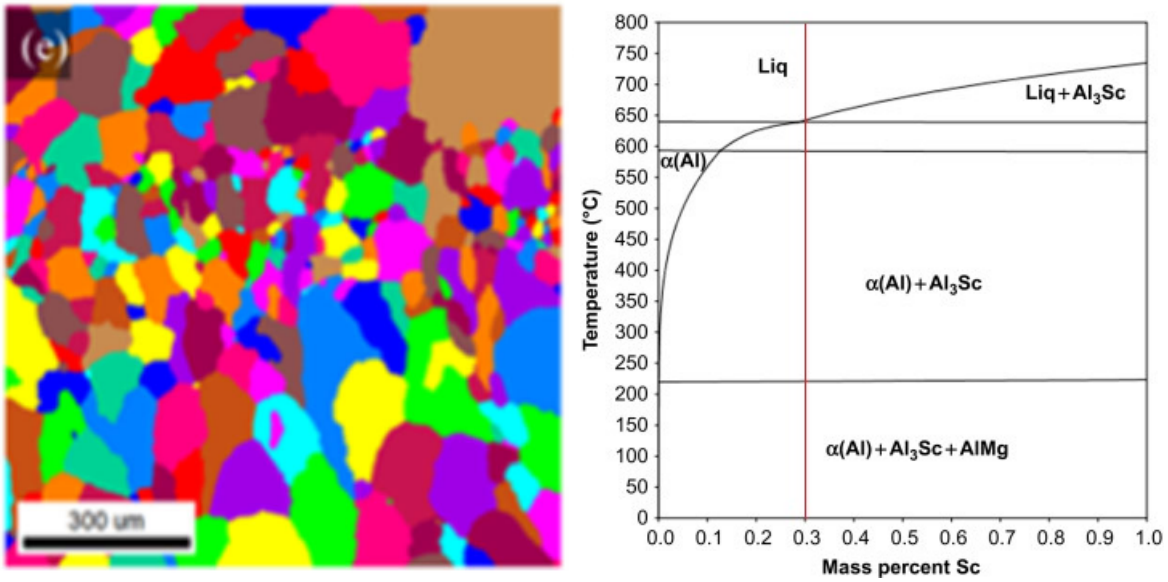


Figure 5.9: Microstructure of WAAM-deposited Al-5183 (a-c) three different samples taken in the study [81]



(a) (b)

Figure 5.10: (a) Microstructure of WAAM-deposited Al-5183 [82] (b) Phase diagram of Al–4 wt.%Mg–Sc (red line indicating mass percentage in feedstock used in this study) [83]

However, the addition of Scandium to the material, as is the case with the feedstock used in this study, has an impact on grain growth during AM.

Scandium exhibits low solubility in the aluminum matrix. During the rapid cooling inherent in AM, scandium atoms precipitate as primary intermetallics - predominantly as coherent Al_3Sc particles - which act as potent heterogeneous nucleation sites. The inclusion of Mg in 5000-series alloys does not influence the kinetics of Al_3Sc formation. Consequently, the ternary Al–Mg–Sc alloy exhibits behavior akin to the combination of the two binary alloys, Al–Mg and Al–Sc. Figure 5.10b shows the phase diagram of Al–4 wt.%Mg–Sc, which indicates that during solidification, the feedstock used in this study should form Al_3Sc precipitates during solidification, and depending on the time spent below 220 °C, some Al-Mg intermetallic phases might also form.

The formation of Al_3Sc precipitates leads to increased nucleation rates, a finer and more uniform grain structure, and also impedes grain boundary migration. This particle pinning effect stabilizes the microstructure by limiting grain coarsening during the thermal cycles typical of AM processes, thereby preserving a refined microstructure even during repeated remelting and solidification. [83].

It is thus expected that the microstructure of the samples in this study will have finer grains than those studied in unmodified Al-5183, particularly at layer interfaces due to the higher cooling rates and thus increased Al_3Sc formation.

Figure 5.11 shows a stitched panorama of a large portion of the etched sample, where the boundaries between the weld beads of different layers are clearly visible, along with several longer cracks and some impurities. In several regions of the sample, small ripple effects were visible, likely due remaining water and improper drying of the sample after etching.

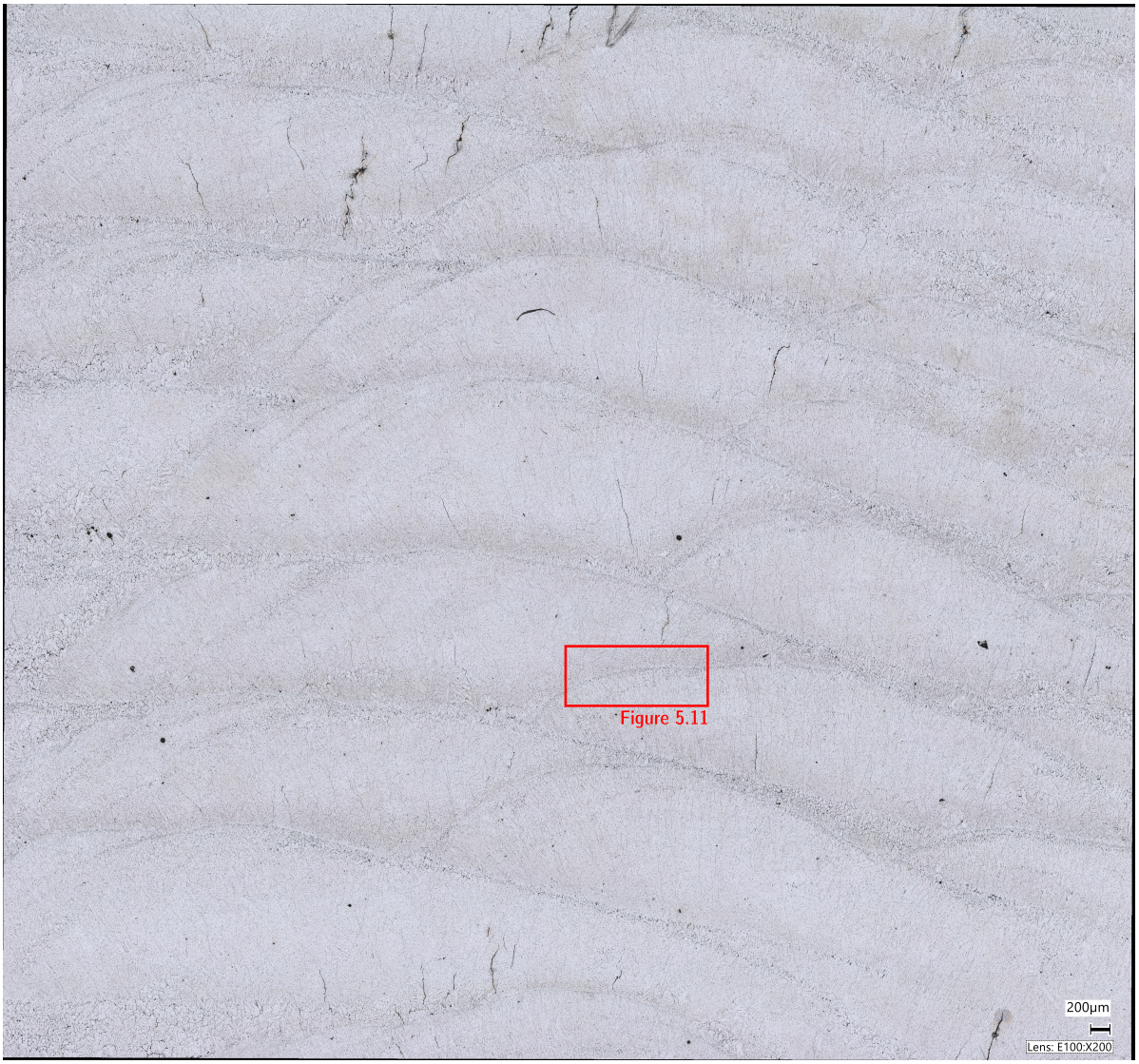


Figure 5.11: Panorama of etched sample showing weld bead boundaries, grain boundaries, and some potential impurities

Figure 5.12 shows a zoomed in view of the etched sample, where the grain boundaries are more clearly visible. It can be seen that the grain boundaries, insofar as closed regions can be seen, are not fully revealed by the etching process inside the weld beads, but only at the bead boundaries. The small dark lines apparent throughout the sample were not visible before etching, thus cannot be said to be microcracking. It is apparent that the grains are refined quite significantly at layer interfaces, and that the orientation of grains in the weld beads aligns roughly with the direction of the thermal gradient during the printing process, which is expected. The small black dots visible throughout the sample are expected to be pores, since Al_3Sc precipitates are an order of magnitude smaller, typically 2-6 nm in diameter. [83]



Figure 5.12: Zoomed in view of the etched sample at 200x magnification

In some regions of the sample, it was possible to attempt a rough manual counting and measurement of the grain sizes, as shown in Figure 5.13.

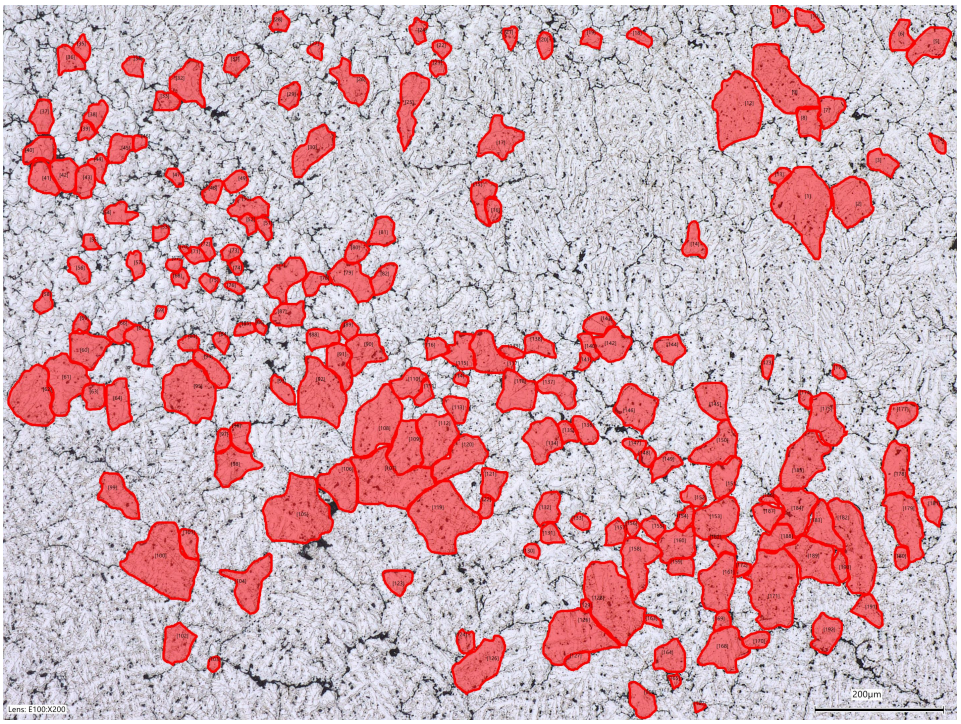


Figure 5.13: Manually identified grains at layer interfaces and in weld beads

Analysis of the grain areas and equivalent diameters is shown in Figure 5.14. The grain areas were directly measured from the microscope images, and the equivalent diameters were calculated from the areas using the formula $A = \pi \left(\frac{d}{2}\right)^2$. It is apparent that the grains are not uniformly distributed, with a nearly exponential distribution of grain sizes favouring smaller grains, with most having an area of less than 1000 μm^2. This is expected due to the sample image being taken at a layer interface, showing the previously mentioned grain refinement. The diameters are distributed more along a log-normal distribution, although this is the result of treating each grain as a circle and not accounting for the actual shape of the grains. The average equivalent diameter of 42.75 μm is in good agreement with the average of 50.81 μm as well as the distribution reported by Li et al. [82], indicating that the grain refinement is

consistent with the literature. It is expected that better etching techniques would reveal more of the grain boundaries in the weld beads, but that the resulting distributions would be similar at weld bead interfaces. Further microscopy techniques such as Electron Backscatter Diffraction could be used to more accurately determine the grain sizes, orientations, and shapes.

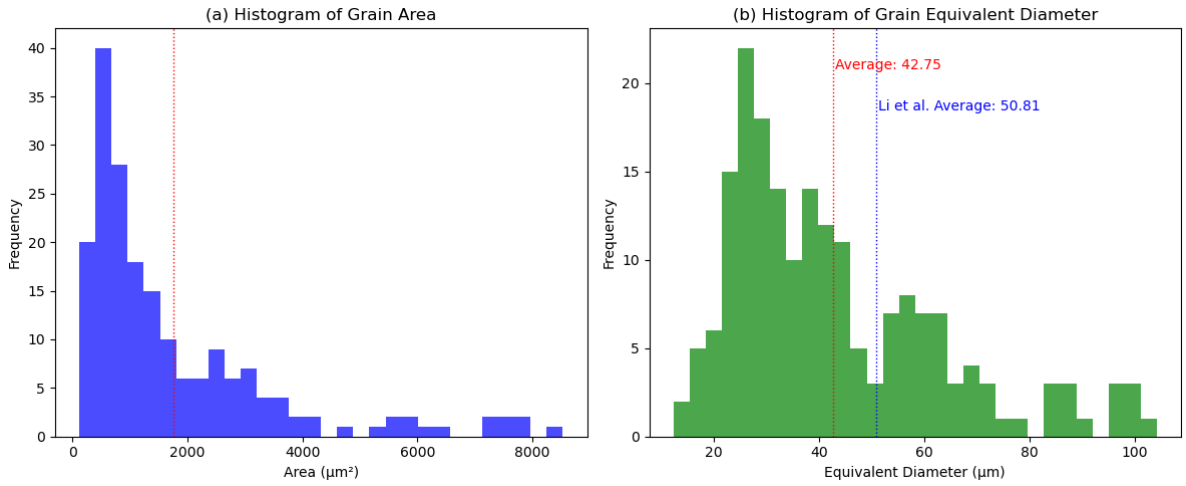
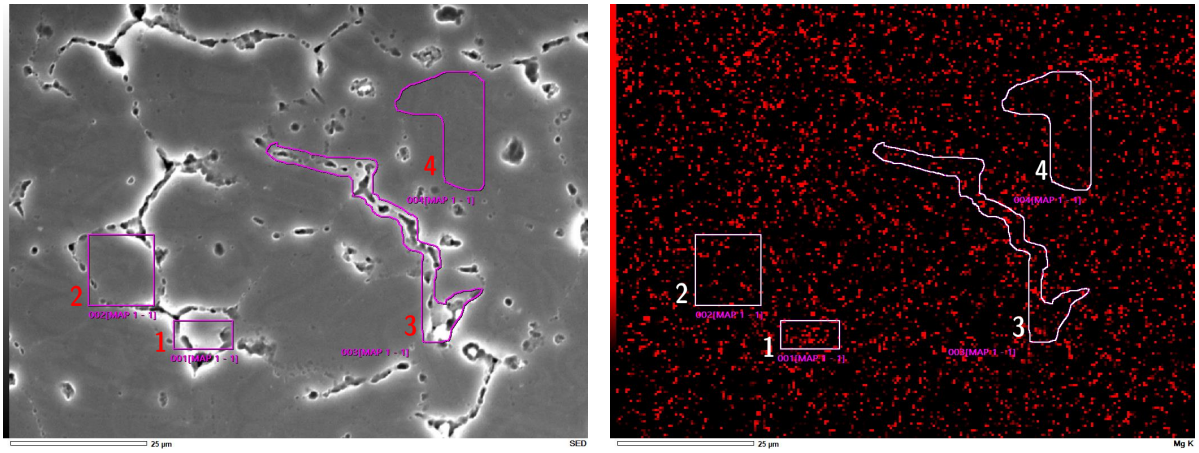


Figure 5.14: Histograms of measured grains in Al-5183-Sc etched sample. (a) Histogram of measured grain areas. (b) Histogram of equivalent grain diameters.

5.3.2. Scanning Electron Microscopy (SEM) Results

Identifying the presence of intermetallic phases is possible through SEM by using Energy Dispersive X-ray spectroscopy (EDS), which can be used to identify the presence of different elements in the sample in different regions. Different regions, specially across grain boundaries, are expected to have significantly different concentrations of Mg if different phases are present. Figure 5.15 shows the a SEM image taken of grain boundaries with regions of interest shown in purple, and the corresponding Mg concentration map in Figure 5.15b.



(a) (b)

Figure 5.15: EDS analysis of the etched Al-5183 sample. (a) SEM image of grain boundaries with sampled regions. (b) EDS concentration map of Mg concentration map based on the SEM image in (a)

The four different regions shown in Figure 5.15b have differing concentrations of Mg, as shown in Table 5.3. The difference in concentrations, particularly between regions 1 and 2, would indicate that a degree of spatial segregation of Mg is occurring, expected to be the Al-Mg phase as shown in Figure 5.10b. This is also indicated by the visibly higher presence of Mg along the grain boundaries in Figure 5.15.

Region	Molar Mg %
1	10.86
2	6.53
3	8.44
4	6.47

Table 5.3: Mg concentration in the different regions

Figure 5.16 shows the distribution of Sc along a crack in the sample, shown in Figure 5.17. According to the average expected grain size of 42.75 μm, this data leads to a suspicion that distribution patterns of Sc are consistent with Al_3Sc precipitates fixing grain growth and thus accumulating along grain boundaries [84]. The presence of Sc precipitates is consistent with the literature [75, 83], but further investigation with more advanced methods like EPMA (Electron Probe Microanalysis) is required to confirm the presence of Al_3Sc precipitates.

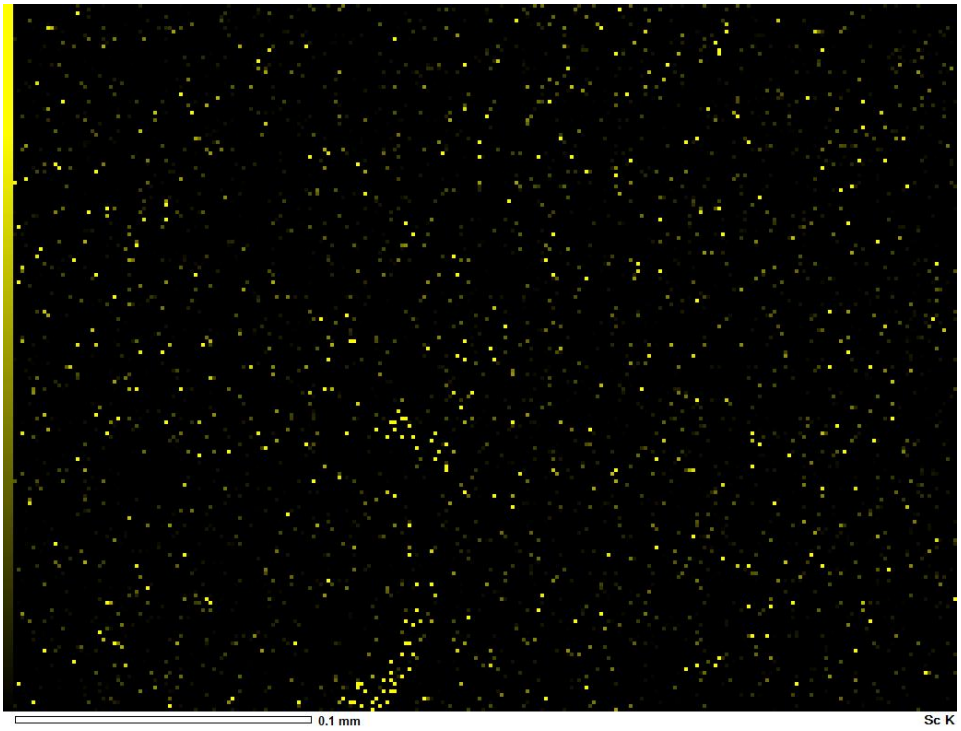


Figure 5.16: EDS map across a crack showing Sc distribution

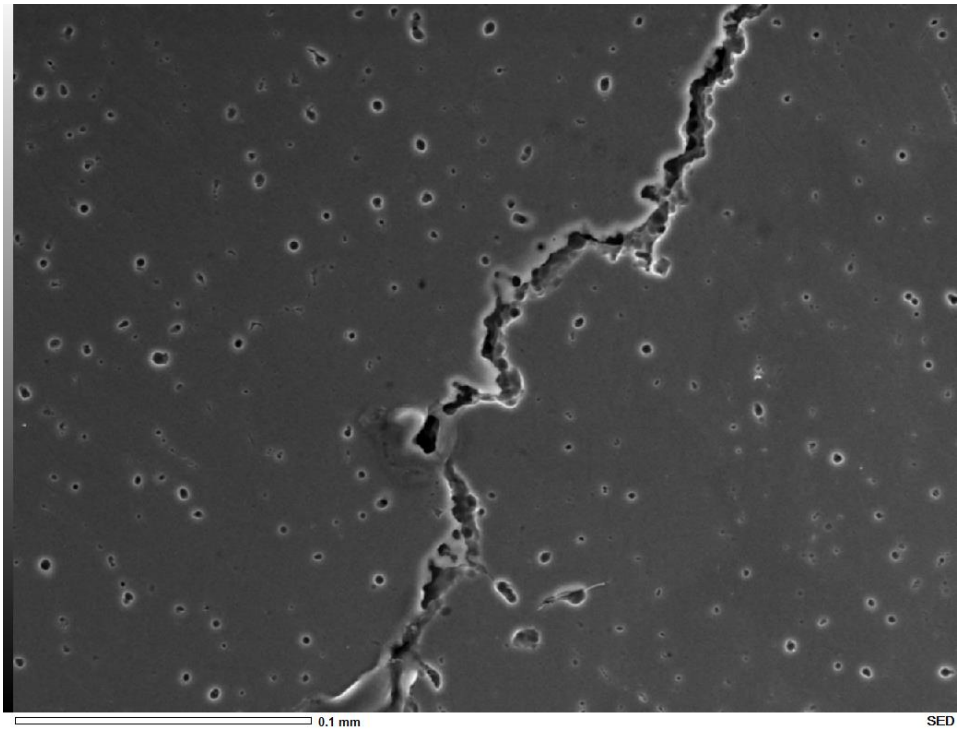


Figure 5.17: SEM image of a crack in the etched Al-5183 sample

5.3.3. Hardness Results

Results for HV0.2 hardness along the build direction in the measured zigzag pattern are shown in Figure 5.18. As can be seen, the hardness ranges from 90 to 110 HV0.2, averaging around 100 over the length of 5 tested mm. Of note is the downtrend of the hardness in the initial half of the measurement length, which likely indicates the difference between inter-layer boundaries with refined grains and inner-layer regions with coarser grains. Dong et al. [81] reported a similar range of hardness values for their WAAM-deposited Al-5183 samples, with an average of 75 HV0.2. The annealed HV0.2 of Al-5183 as stated in the literature [85] is approximately 85 HV. The addition of Scandium to aluminum alloys is known to improve hardness due to the formation of Al_3Sc precipitates, which act as barriers to dislocation movement, making it more difficult for the surface to deform plastically [83]. However, the lower cooling rates resulting from the pre-heating of the baseplate likely resulted in grain coarsening and thus a decrease in hardness gains from the Scandium addition.

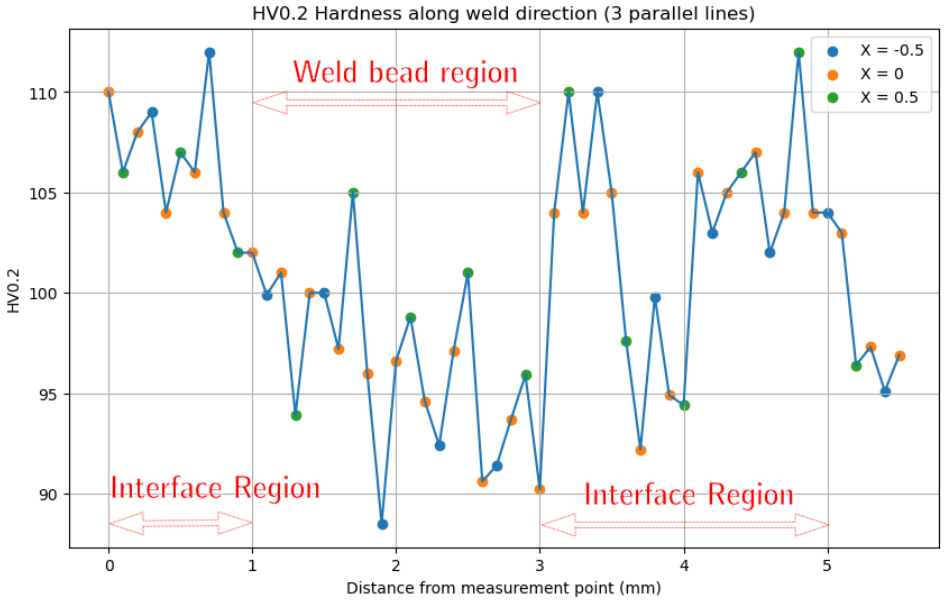


Figure 5.18: HV0.2 hardness along the build direction for the three parallel lines

5.4. Mechanical Test Results

14:3014

The stress-strain curves of the yield tests are shown in Figures 5.19 and 5.20 for the Longitudinal and Transverse orientations of the samples, respectively. The summary of the results is shown in Table 5.4.

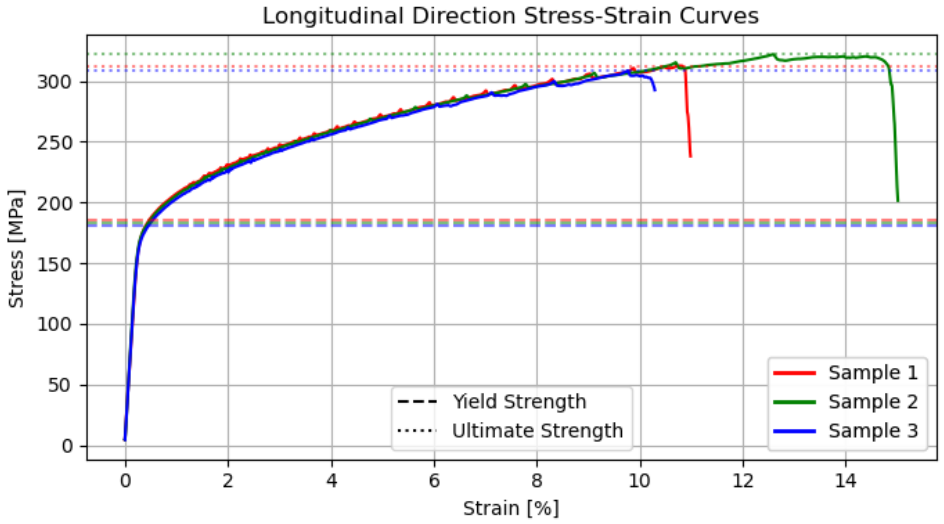


Figure 5.19: Stress-strain curve for longitudinal samples

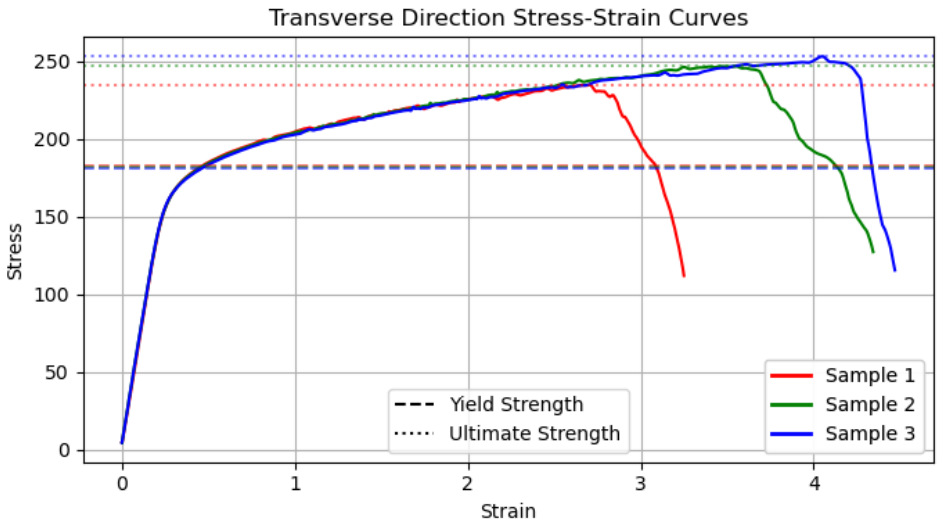


Figure 5.20: Stress-strain curve for transverse samples

Table 5.4: Mechanical Test Results

Sample	Orientation	⌀ [mm]	YS [MPa]	UTS [MPa]	E [%]	Area Reduction [%]
1	Long.	6.04	185	313	7.5	8.0
2	Long.	6.03	183	322	18.0	22.5
3	Long.	6.00	181	309	11.5	18.0
1	Trans.	6.00	183	235	3.5	5.5
2	Trans.	6.00	182	247	5.0	9.0
3	Trans.	6.04	181	253	4.0	6.5

The strength of the deposited material is roughly equal in both the longitudinal (build) and transverse (weld) orientations, with an average yield strength of roughly 180 MPa. However, the difference in ultimate tensile strength is more significant, with the transverse orientation suffering a 25% reduction in UTS. This is expected due to two factors: the larger number of weld bead interfaces and thus fine-grained regions in the longitudinal direction, and the orientation of the grains along the longitudinal direction. The latter increases the cross-sectional area of the grains along the transverse direction, lowering strength according to the Hall-Petch relationship shown in Equation 5.1. [86]

$$\sigma_y = \sigma_0 + k \cdot d^{-1/2} \tag{5.1}$$

where σ_y is the yield strength, σ_0 is a material constant, k is the Hall-Petch slope, and d is the average grain diameter. This equation indicates that yield strength increases as grain size decreases.

Comparably processed Al-5183 has shown yield strengths within a range of values depending on processing conditions and heat treatment applied. Ponomareva et al. [75] reported yield strengths of 176 MPa and UTS of 337 MPa for as-deposited Al-5183 with 0.23% Sc and 0.19% Zr additions. Dorin et al. [83] reported a distribution of yield strengths between 180 and 380 MPa for Al+0.3%Sc 5000-series alloys over a range of different processing conditions and heat treatments applied, as shown in Figure 5.21.

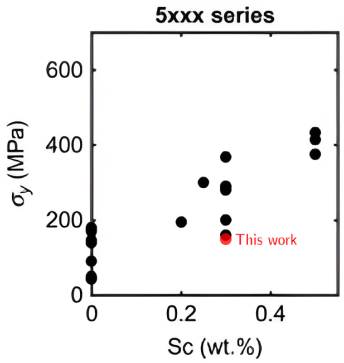


Figure 5.21: Yield strength of Al-Sc 5000-series alloys with different concentrations of Sc [83]

Dong et al. [81] and Li et al. [16] studied Al-5183 without Sc addition, and reported yield strengths of 120 MPa and 123 MPa, and UTS of 270 MPa and 285 MPa, respectively. These results are shown in Table 5.5.

Table 5.5: Summary of Yield Strength and Ultimate Tensile Strength Results

Source	YS [MPa]	UTS [MPa]	Notes
This work	183	322	Al-5183+0.3%Sc, as-deposited
Ponomareva et al. [75]	176	337	Al-5183 + 0.23% Sc and 0.19% Zr, as-deposited
Dorin et al. [83]	180-380	-	Range of values for Al+0.3%Sc 5000-series alloys.
Dong et al. [81]	120	270	Al-5183, as-deposited
Li et al. [16]	123	285	Al-5183, as-deposited

Therefore, it can be concluded that the addition of Scandium as a precipitation hardening agent improved YS and UTS of Al-5183 by 50% compared to the base material under similar deposition conditions, even taking the pre-heating of the baseplate into account. The Al_3Sc phase coherently integrates with the aluminum matrix, effectively impeding dislocation movement. This results in improved yield strength and tensile properties. Additionally, these thermally stable precipitates resist coarsening at high temperatures encountered during fabrication and heat treatments. They act as barriers to grain boundary movement, preserving the fine-grained structure against thermal exposure and preventing recrystallization and unwanted phase changes during subsequent processing or elevated temperature service. [83]

Tensile strength performance compared to Ponomareva et al. shows a slight improvement, and while a YS of 183 MPa is at the lower range of the values reported in Figure 5.21, this is likely due to the lack of heat treatment in this research.

For the purposes of using this material and process to build space infrastructure, a fair comparison to make is between this work's results and the strength of Al alloys commonly used in space structures, such as Al-2024, Al-7075, and Al-6061-T6, as shown in Table 5.6.

Table 5.6: Mechanical Properties of Selected Aluminum Alloys [87]

Alloy	Yield Strength (MPa)	Temper
This work	183	No Temper
Al-2024	140-210	No Temper
Al-2024	270-280	T3, T4, T851
Al-7075	140	No Temper
Al-7075	430-450	T6
Al-7075	500	T651
Al-6061-T6	276	T6

As can be seen, the yield strength of this work's material is comparable to untempered versions of popular space Al alloys, but considerably weaker than the tempered versions commonly used in the industry. It is important to highlight that the as-deposited material in this work was used for mechanical property comparisons due to the current infeasibility of heat treating large ISAM structures while in orbit. Designing printing conditions and strategy that would keep the workpiece at elevated temperatures for extended periods of time during manufacturing could allow for pre-tempering of the material, which would result in a significant increase in strength.

5.5. Orbital Conditions Simulation Results

Based on the previously presented results, it is deemed possible to estimate the approximate thermal profile of a medium sized component printed in orbit, not taking into account the granular thermal behavior in the melt pool.

The results of the 15 simulations run for the three different orbital scenarios presented in the following figures. Figure 5.22 shows the thermal profiles at several different interlayer cooling times for the shielded scenario. Figures 5.23 and 5.24 show the thermal profiles for the hot and cold scenarios, respectively. All three figures only show the thermal evolution of the average workpiece and baseplate temperatures, and each case can be seen to converge on a quasi-steady state profile.

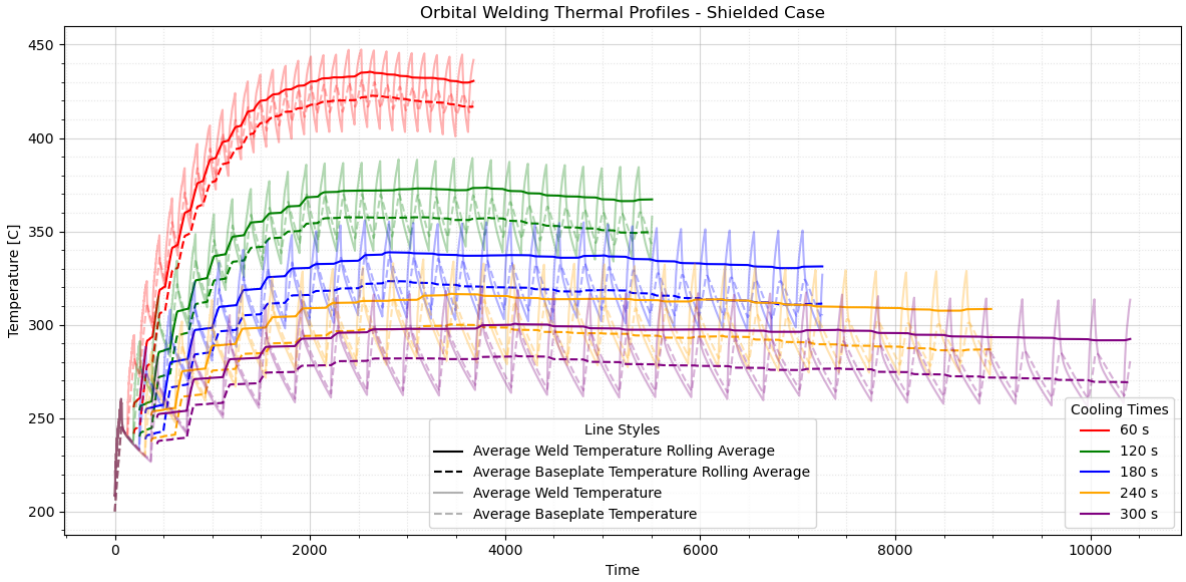


Figure 5.22: Thermal profiles at different interlayer cooling times for the shielded scenario - average workpiece and baseplate temperatures

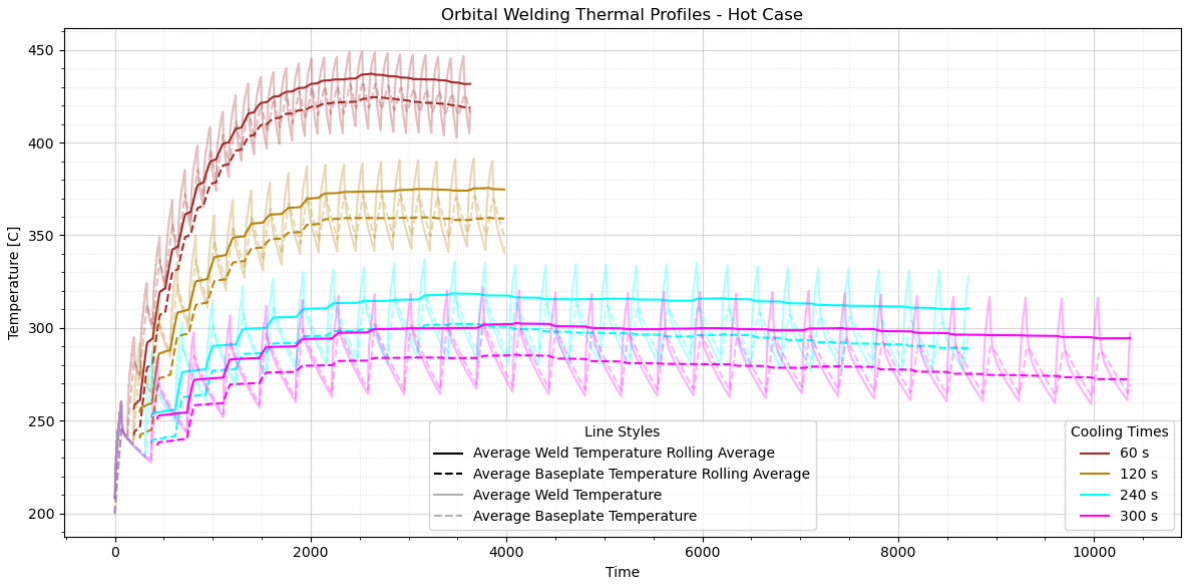


Figure 5.23: Thermal profiles at different interlayer cooling times for the hot orbital scenario - average workpiece and baseplate temperatures

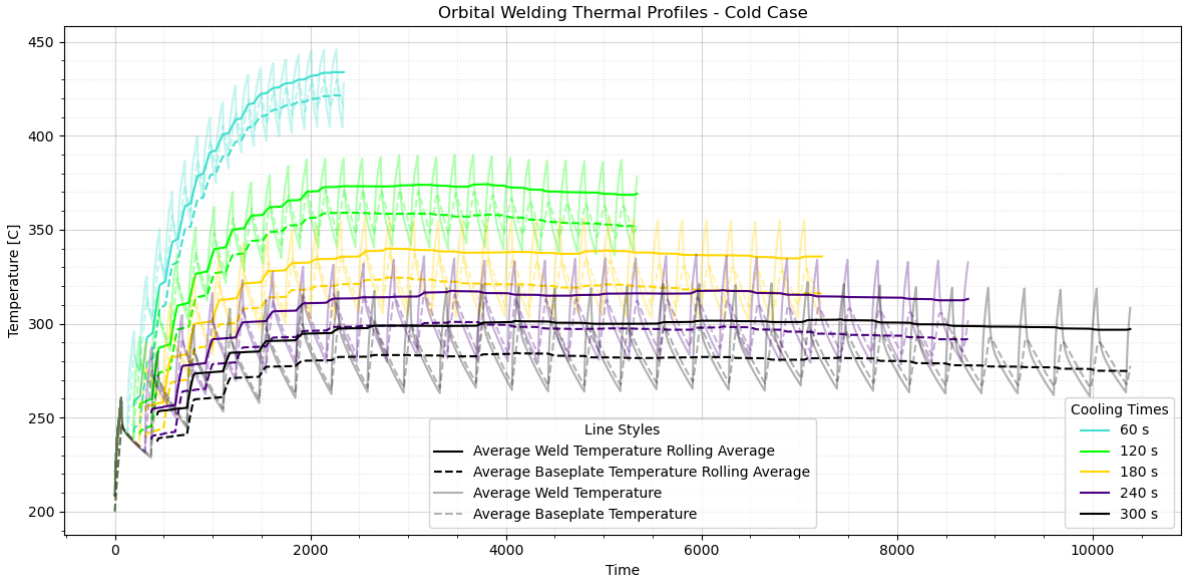


Figure 5.24: Thermal profiles at different interlayer cooling times for the cold orbital scenario - average workpiece and baseplate temperatures

The thermal profiles for all three cases are nearly identical. Figure 5.25 shows the difference in average workpiece temperature betwee the three cases. The difference between any of the three cases does not exceed 5 °C, indicating that for this small component, the incoming environmental heat has a negligible effect on the thermal profile.

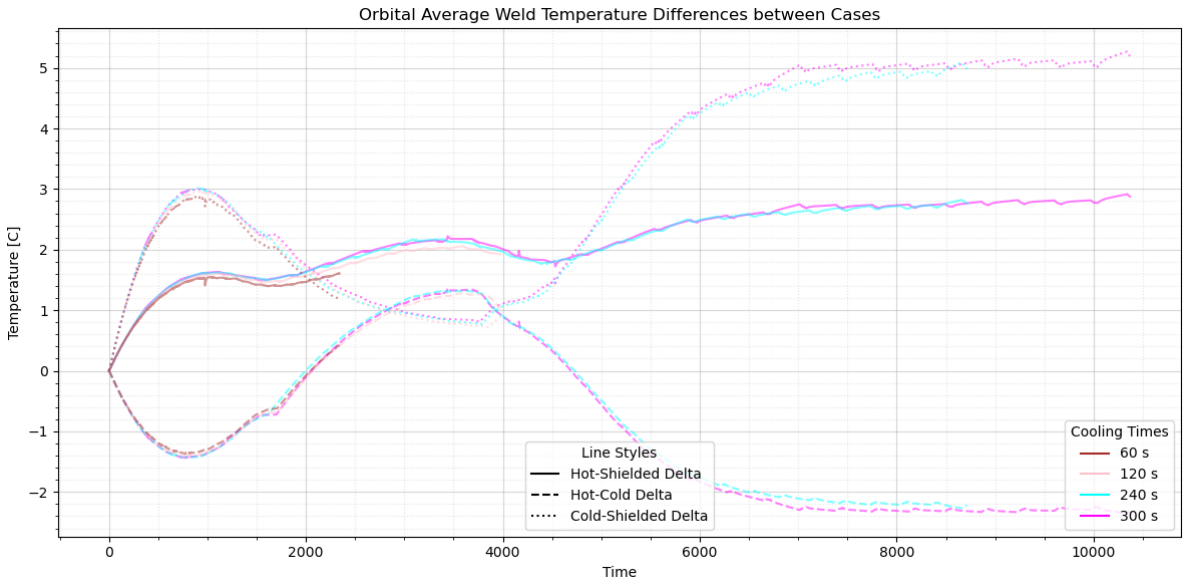


Figure 5.25: Difference in average workpiece temperature between the hot, cold and shielded cases

This is to be expected, considering the total incoming heat flow on the workpiece and baseplate is on the order to 20 W for both the hot and cold cases, as shown in Figure 5.26. Compared to the weld heat input of 1651 W, this is negligible.

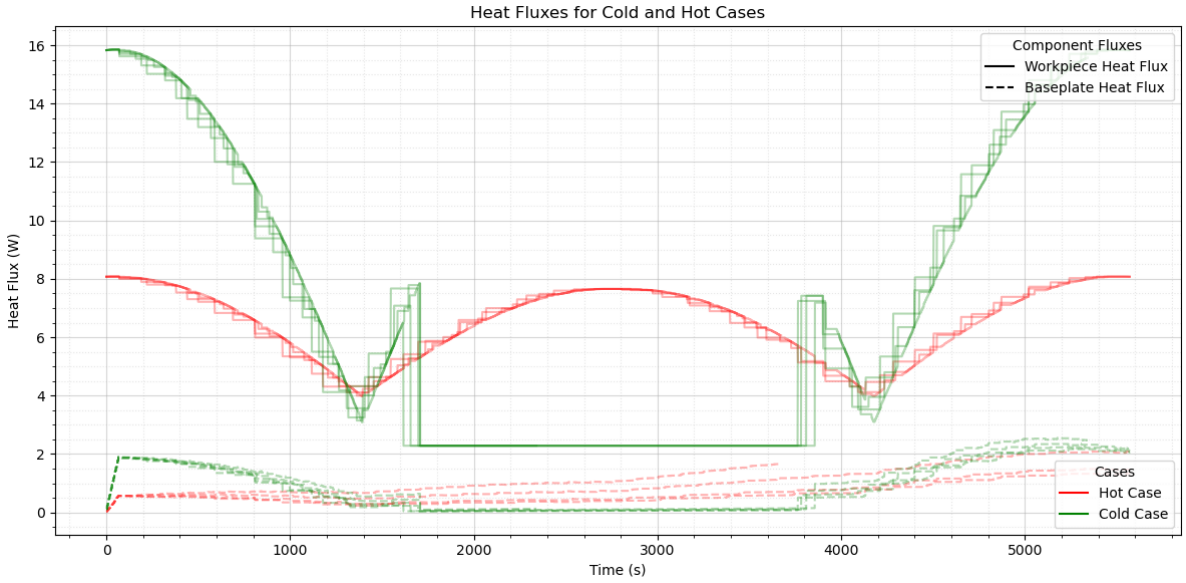


Figure 5.26: Total incoming heat flow on the workpiece and baseplate for the hot and cold cases - all simulated profiles shown for a single orbital revolution

Figure 5.27 shows the average steady-state temperature plotted against the total required print time, averaged over the three different scenarios. The decrease in average temperature with increased cooling time is roughly exponential, indicating that the most impactful reduction in process temperatures is achieved without too much increase in print time.

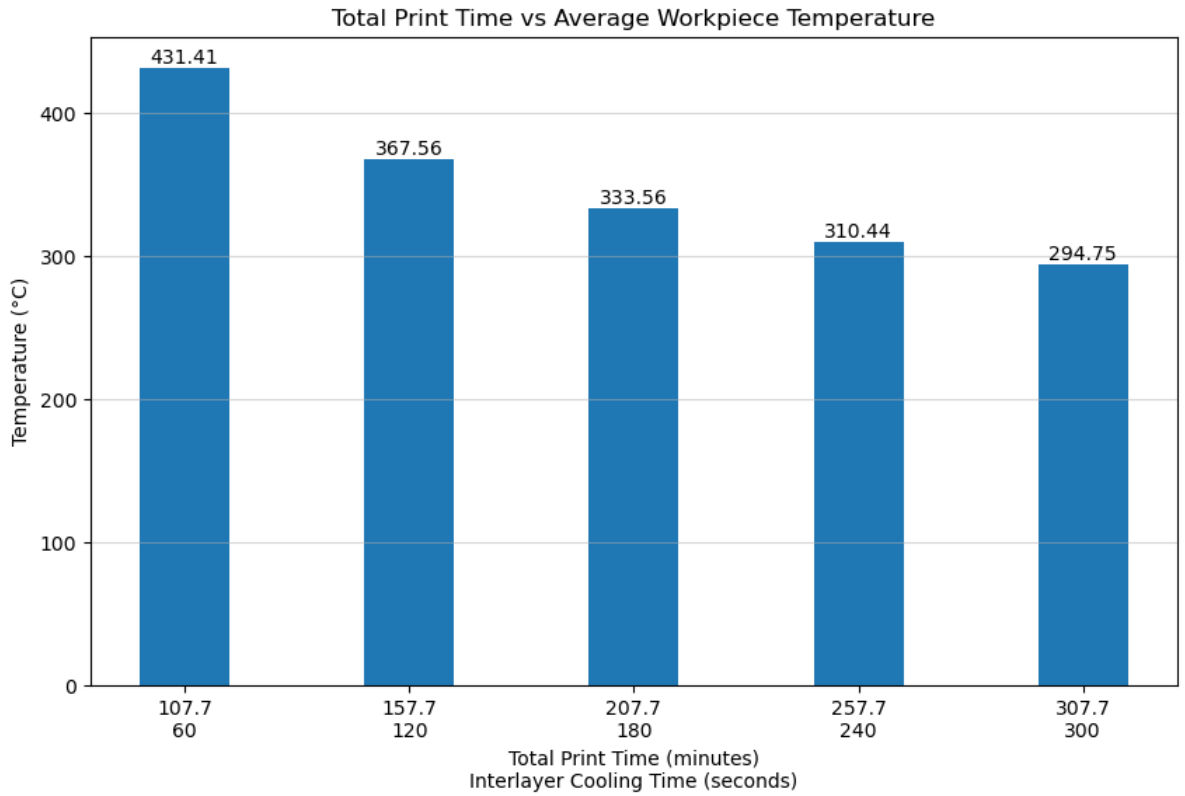


Figure 5.27: Comparison of average workpiece temperature vs total print time - averaged over hot, cold and shielded cases

The highest average temperature is achieved in the hot case for 60 seconds of cooling at 431 °C. Figure 5.28 shows the full thermal profile of this trial alongside the radiative heat loss from the workpiece and baseplate. As can be seen, the maximum temperature of the workpiece does not begin to exceed the melting temperature of the feedstock until the sixth layer is printed. This is unrealistic and due to the high amount of heat lost to the baseplate, which has an initial temperature of 0 °C. However, the steady state heating profile has a maximum temperature envelope comparable to that of the laboratory thermal model, indicating that the underestimation of maximum weld temperatures is similar between both cases.

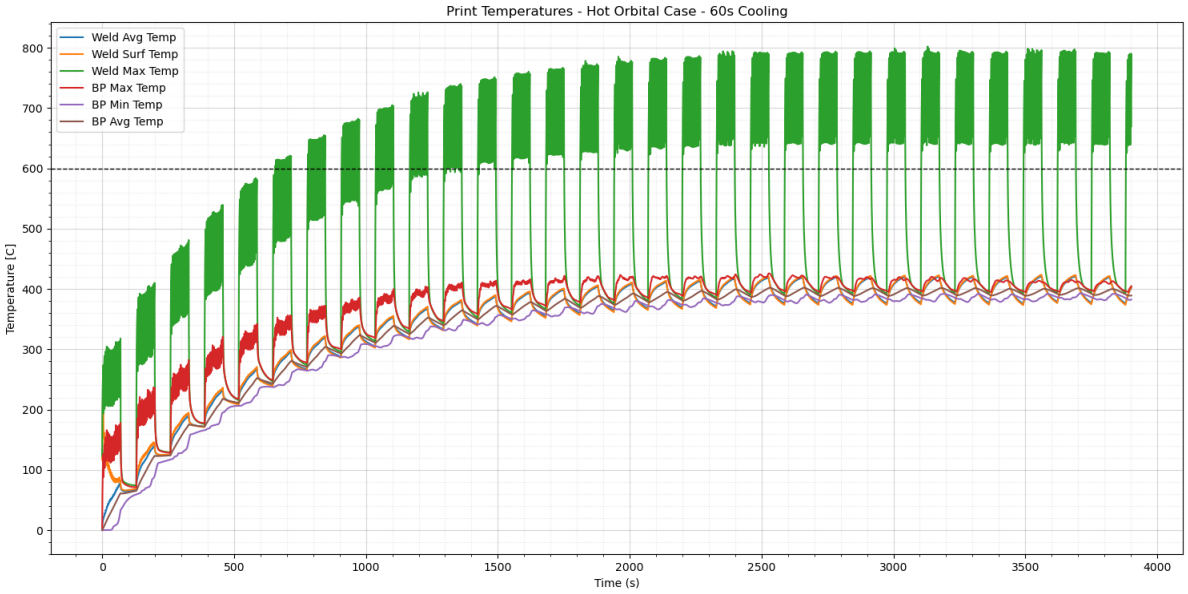


Figure 5.28: Thermal profile of the hot case with 60s cooling - maximum, minimum and average temperatures for the workpiece and baseplate

A simple conclusion that can be drawn from the heat profiles shown in Figures 5.22 to 5.24 is that pre-heating the baseplate before deposition helps lower the total thermal gradient experienced during printing. A lower thermal gradient would result in less distortions arising over the length of the printing process, since the different sections of the workpiece would have less varied thermal expansions, and ideally have a more consistent cooling pattern. However, the lower thermal gradient would also cause the workpiece to remain at elevated temperatures for longer, potentially causing grain coarsening and thus a decrease in strength and hardness. The Sc-containing feedstock used in this work is an attractive option for ISAM since the presence of Scandium raises the temperature at which grain coarsening occurs significantly [83]. This would allow for a hotter deposition process without causing detrimental grain growth.

5.5.1. Full-Scale Space Habitat Simulation

In this Section, the conclusions from Section 5.5 and the rest of this work are applied to the ISAM manufacturing of the full-scale space habitat. Some of the results that seemed negligible for small components are shown to have significant impact at a larger scale. Additionally, futher considerations for thermal behavior and the possible modeling of these effects are presented, along with a discussion on potential passive thermal control strategies. These are preferred over active ones due to the relative difficulty in thermally controlling structures several meters in size in free-flying vacuum.

The results in Section 5.5 show that the effect of different orbital conditions on the thermal evolution during ISAM of small components is negligible, as the small scale of the structure causes thermal evolution to be dominated by the welding process itself. However, for a full-scale space habitat with dimensions on the order of several meters, these effects cannot be ignored.

The full-scale space habitat cylinder has a radius of 2.2 m and length of 7.07 m. Using the same deposition parameters and layer thickness as for the large laboratory model, given in Tables 4.9 and 4.11, each layer would take 32 minutes to print, which is between 10-30 times longer than the cooling times considered in this work. By the time the welding torch reaches the end of the current layer, that location will already have settled at the equilibrium temperature of a structure with the current dimensions in orbit.

This is underscored by the dominance of environmental heat over the process at such scales. Figure 5.29 shows the incoming heat flow for the full-sized habitat for both orbital cases. The environmental heating grows with structure size in both cases, with the cold case experiencing a sharper reduction during full eclipse. During eclipse, this heating for the cold case is only 1-5 times greater than the welding

heat input, but while receiving solar flux, can be up to 20 times greater. This in effect means that the welding process will have a quasi-steady heat sink at the equilibrium temperature of the structure, as conduction is dominant and the mass of the structure is much larger than that of the added feedstock.

Further thermal simulation of such larger structures might be simplified by reducing the problem to a simple substrate at the equilibrium temperature. Deposition at this scale can also be done continuously without cooling periods, and thus modeled as a continuous process with only the substrate temperature changing over time.

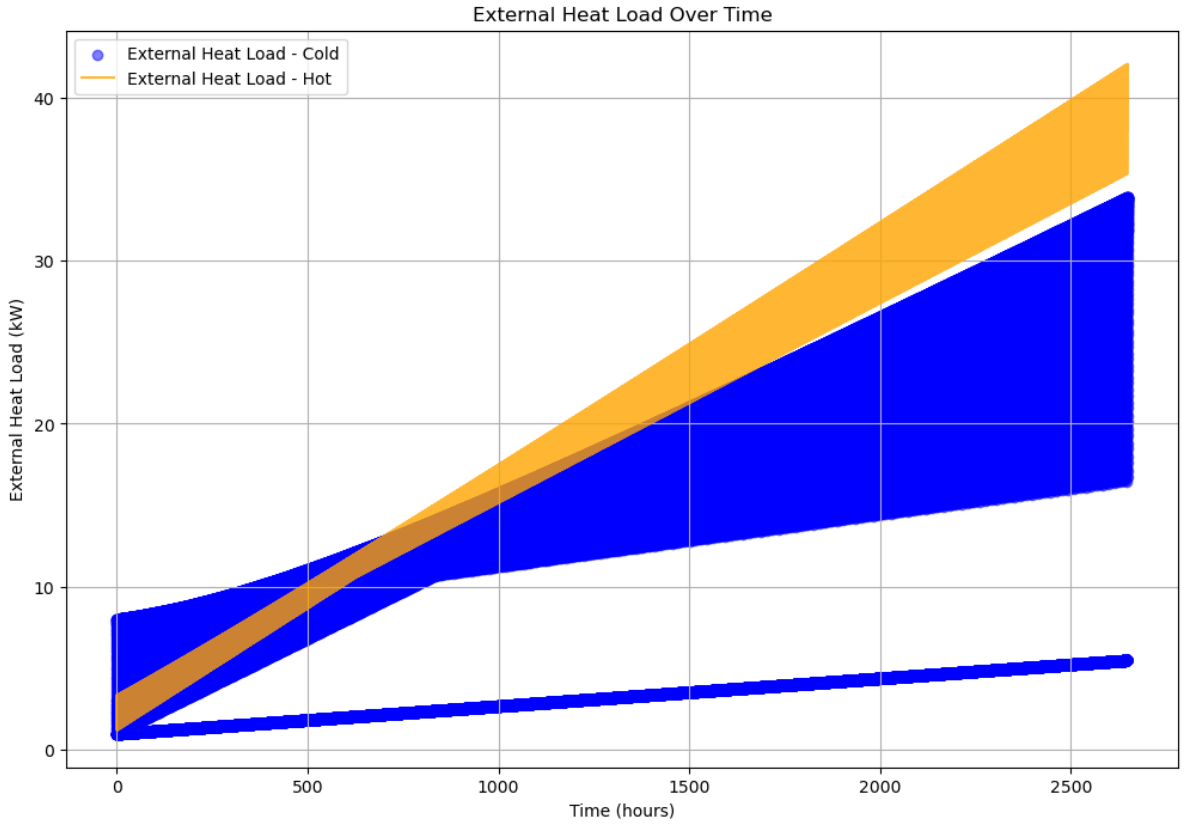


Figure 5.29: Incoming heat flux for the full-sized habitat for both orbital cases

The resulting equilibrium temperatures are shown in Figure 5.30. The cold case experiences significant temperature oscillations during eclipse, reaching a minimum of -90 °C, and oscillates around 50 °C outside eclipse. The hot case has a much narrower and slightly higher range, beginning at a low average of -25 °C with 50 °C swings and approaching an average of 20 °C within a roughly 10 °C range.

Such large equilibrium temperature oscillations have consequences not only for the deposition process itself, but on the overall geometric accuracy of the structure. Large periodic thermal gradients can cause anisotropic thermal expansion and thermal cycling fatigue, which can lead to significant distortions and stresses within the structure. Additionally, depositing molten aluminum feedstock onto quasi-cryogenic workpieces can cause cracking and undesirably high cooling rates in the heat-affected zone. [29]

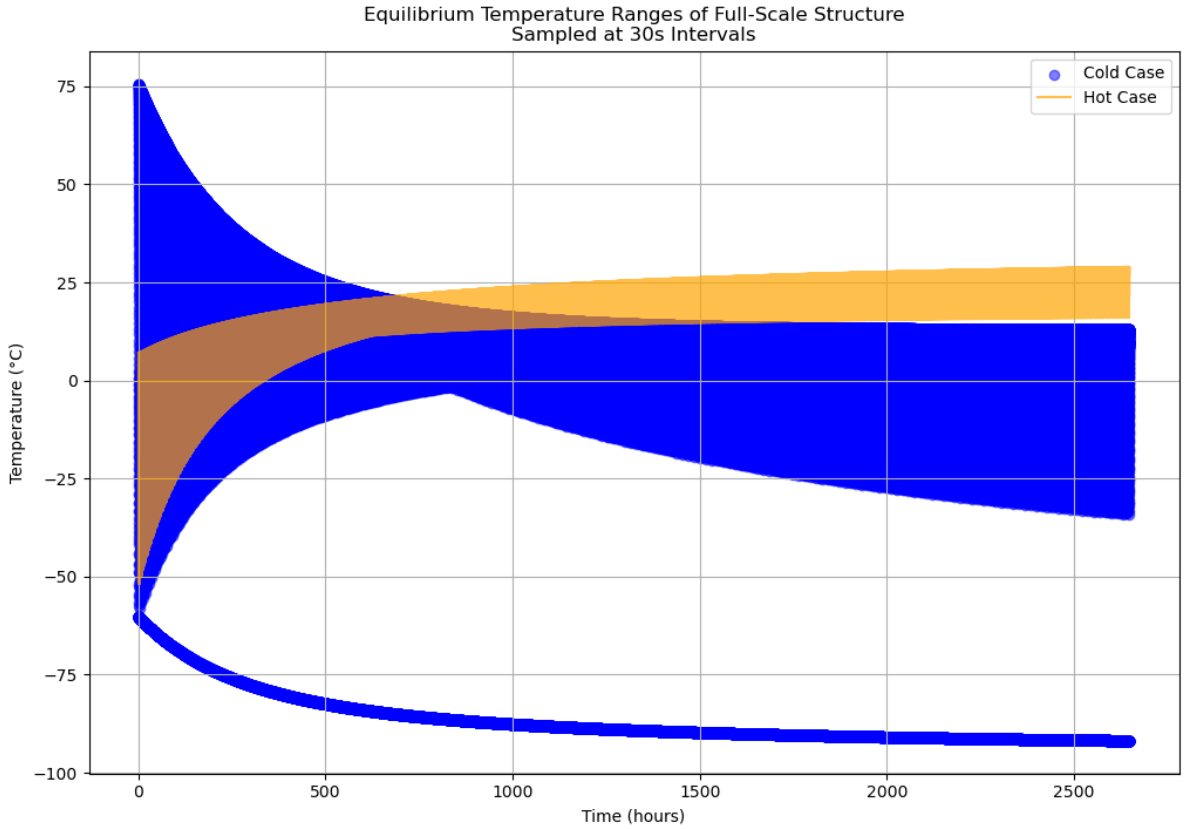


Figure 5.30: Equilibrium temperatures of the full-scale structure in the hot and cold orbital case (no weld heat input applied, 0 seconds cooling time between layers)

If no thermal shielding is available for the ISAM process, it is thus preferable to choose orbits similar to the hot case for more stable thermal conditions. However, one of the current assumption of the orbiting cube model is that the orientation of the structure towards Earth is constant, with the Zenith face pointing away from the Earth. For the hot case, the incoming environmental heat flux is primarily incident on the South face of the structure, as shown in Figure 3.16. This would cause one side of the cylinder to be heated disproportionately, and thus cause thermal gradients along the circumference of the cylinder, potentially leading to deformations. One possible solution to this that does not require active thermal control is to slowly rotate the workpiece around its longitudinal axis so that the incoming heat is distributed more evenly along the circumference of the cylinder. The polar moment of inertia of the cylinder around its longitudinal axis would continuously increase as the structure grows, requiring small adjustments to the torque applied at the baseplate. The full calculation of this is left for future work.

In the case that thermal shielding is available, it is not obvious that it would have a positive impact. The low equilibrium temperatures during eclipse in the cold case show that, cut off from an external heat source, the structure will naturally cool to near cryogenic temperatures. Instead of eliminating environmental heating completely, the purpose of such shielding would rather be to act as a thermal buffer. It should absorb incoming external fluxes and radiate the heat evenly from the inside surface of the shield. This inner surface would also reflect or absorb the radiation emitted by the workpiece.

The radiative exchange between the workpiece and the inner surface of the shield largely depends on the emissivity of the latter. Two radiating surfaces in view of each other can be described by the Gebhart factor, which describes the fraction of the radiation emitted by one surface that is absorbed by the other. This takes into account the absorption and re-radiation of energy between the two surfaces [88]. The Gebhart factor is a function of the view factor between the two surfaces and the emissivity of both surfaces. The view factor between the outer surface of the workpiece and the enclosure is assumed to be 1. The Gebhart factor between them is then given by Equation 5.2.

$$B_{\text{cylinder}\rightarrow\text{shield}} = \frac{\epsilon_{\text{shield}} \cdot A_{\text{shield}}}{\epsilon_{\text{shield}} \cdot A_{\text{shield}} + \epsilon_{\text{cylinder}} \cdot A_{\text{cylinder}}} \tag{5.2}$$

Where A_{shield} and A_{cylinder} are the surface areas of the shield and the workpiece, and ϵ_{shield} and $\epsilon_{\text{cylinder}}$ are the emissivities of the shield and the workpiece, respectively. Calculating this for various enclosure emissivities yields the evolving Gebhart factor shown in Figure 5.31.

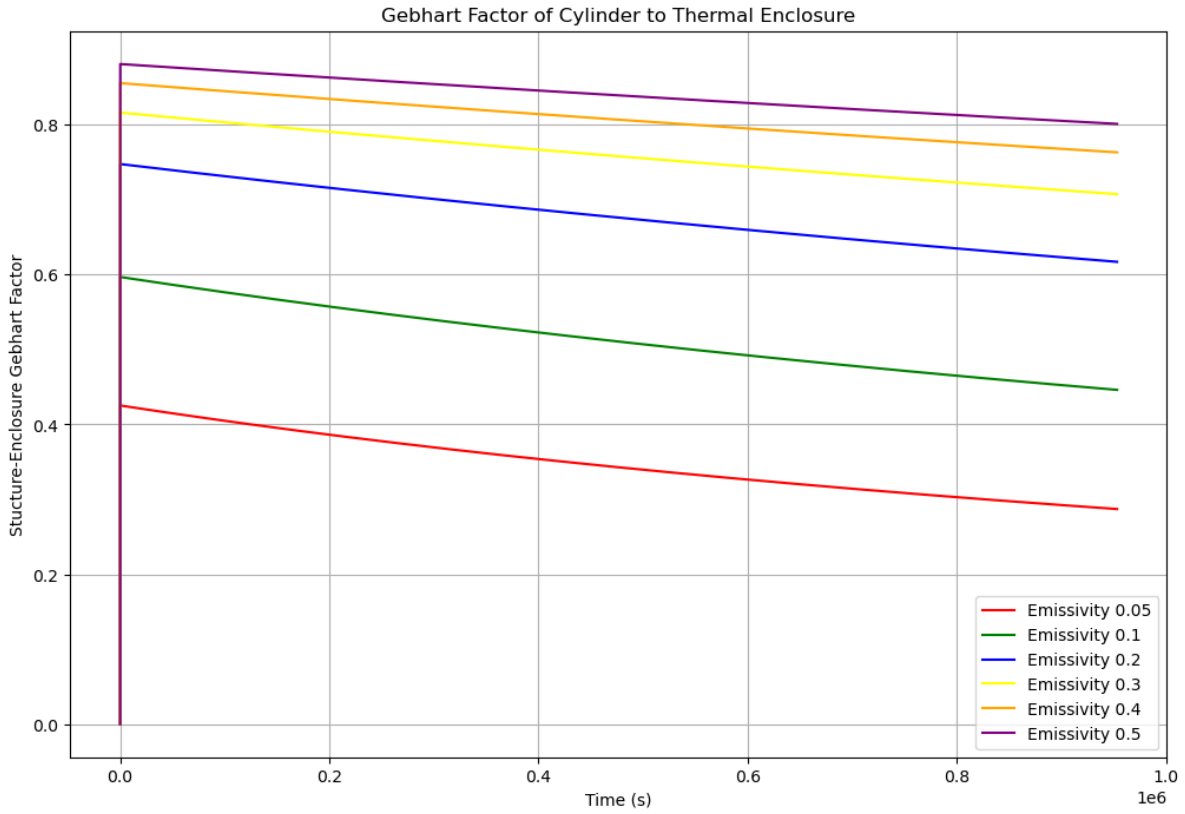


Figure 5.31: Gebhart factor between the workpiece and the inner surface of the shield for various enclosure emissivities

These values indicate that even with a moderate inner enclosure emissivity of 0.2, between 50% and 60% of the radiation emitted by the workpiece is absorbed by the shield. By choosing an outer enclosure coating with a high absorptivity and very low emissivity, the shield can absorb a significant portion of incoming visible solar and albedo fluxes without radiating the heat back out. This traps both the heat from the workpiece and orbital environment in the shield, which it can only radiate back towards the workpiece. The precise calculation of this exchange is beyond the scope of this work, leaving this as a concept proposed for future work.

A final point of consideration for radiative thermal transport at the scales considered is the radiative exchange between the inner surfaces of the hollow cylinder. The inner surface of the workpiece mostly faces itself, and thus will absorb and re-radiate a significant portion of its own radiation, trapping extra heat within the structure and potentially causing thermal gradients.

To estimate this effect, the view factors between the inner surfaces of the cylinder and the outside environment must be calculated. Leuenberger et al. [89] provides an analytical solution for the view factors for a cylindrical structure, shown in Figure 5.33. The view factors for the inner surfaces to themselves and the inner surfaces to the outside environment are given by Equations 5.3 and 5.4, respectively. The Gebhart factor between the inner surfaces and the cylinder opening is given by Equation 5.5 [88].

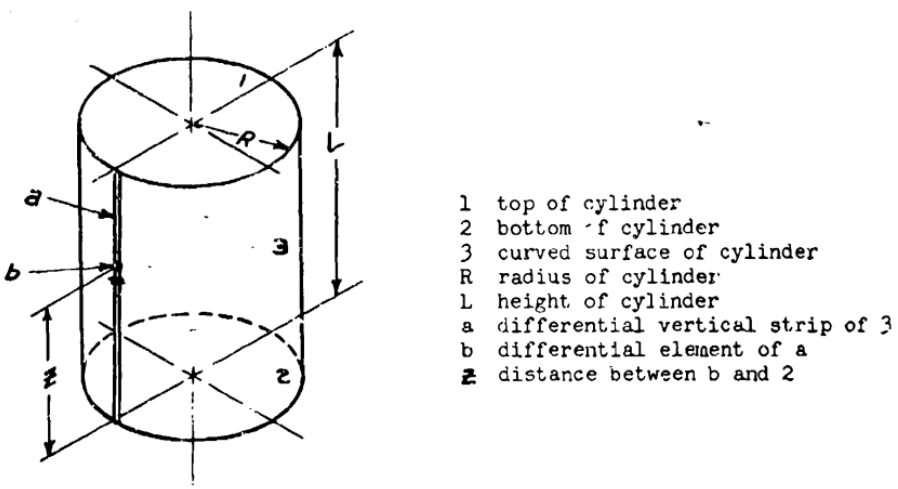


Figure 5.32: View factors for a cylindrical structure [89]

$$F_{3\to3} = 1 - \frac{1}{2}\left(\sqrt{4 + \frac{L^2}{R^2}} - \frac{L}{R}\right) \tag{5.3}$$

$$F_{3\to1} = \frac{1}{2}\left(\frac{L}{R}\sqrt{4 + \frac{L^2}{R^2}} - \frac{L^2}{R^2}\right) \tag{5.4}$$

$$B_{3\to1} = \frac{F_{3\to3}}{1 - 0.8F_{3\to1}} \tag{5.5}$$

Solving these equations for $R = 2.2$ m and ranging L from 0 to 7.07 m, the view factors and Gebhart factor are shown in Figure 5.33. By the end of the deposition process, the inner surfaces have a nearly five times higher view factor to themselves than to the one open end of the cylinder, leading to significant emission and re-radiation of heat within the hollow inside of the cylinder. The Gebhart factor between the inner surfaces and the opening of the cylinder is around 0.55 over the legnth of the process, meaning only only half of the emitted radiation is transmitted to the outside environment. This will be a problem for the ISAM printing of any large scaled hollow structure, and thus must be taken into account in future thermal models. However, this effect can be simplified by taking the view factors at every point in time and incorporating the inner radiative transfer into the calculation of the current equilibrium temperature of the structure. The full development of this model is beyond the scope of this work.

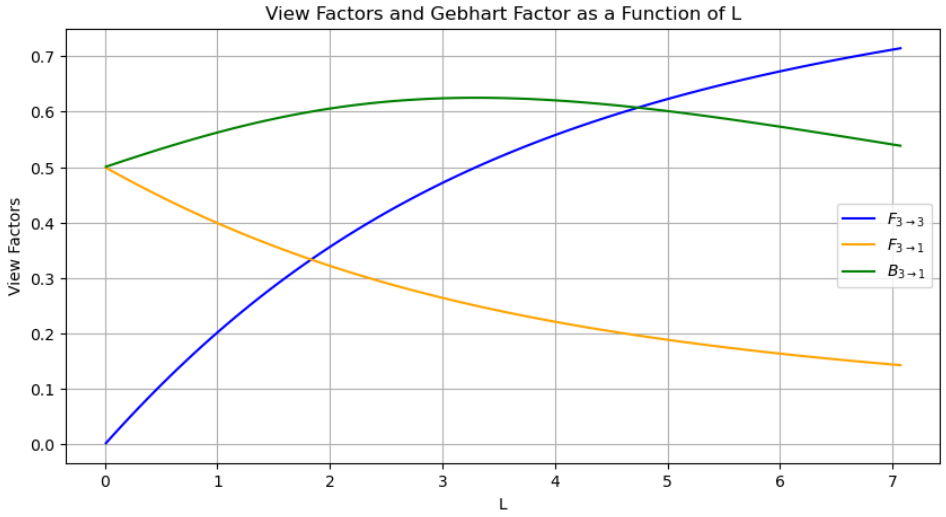


Figure 5.33: View factors for a cylindrical structure

To conclude this section, it is clear that full thermal modeling of large structures presents significant complexity and thus computational power. The aforementioned simplifications and considerations are a first step towards allowing large-scale ISAM processes to be modeled efficiently. The more scientifically important question of the interaction between other environmental factors like microgravity, ATOX, and radiation on the weld pool and resulting structure can then be studied while still taking the full thermal profile of the geometry into account.

5.6. Results Summary

The thermal modeling of the welding process under terrestrial and orbital conditions yields valuable insights into process parameters, microstructural evolution, and mechanical performance. Convective heat transfer simulations allowed the identification of optimal parameters; notably, Trial 15 of the convection coefficient validation model achieved mean absolute errors of 1.33 and 12.73 °C for thermocouples 1 and 2, respectively (Table 5.1). For the high-temperature deposition model, Trial 5 provided the best fit with a thermocouple RMSE of 4.78 °C (Table 5.2), confirming the adequacy of the boundary conditions and heat loss assumptions. However, the discrepancy between the maximum melt pool temperatures in the first simulated layers and experimentally observed values indicates that the model is not able to predict both melt pool and structural temperatures simultaneously, but this is to be expected given the lumped-element heating process used in the simulation.

Microstructural characterization revealed pronounced grain refinement at layer interfaces. The histogram of grain sizes (Figure 5.14) indicates a predominance of small grains, while SEM/EDS analyses (Figures 5.15 and **??**) suggest the formation of Al_3Sc precipitates. Hardness testing further corroborated these findings, with values averaging approximately 100 HV0.2 (Figure 5.18), representing a noticeable enhancement relative to previously reported values for unmodified Al-5183 [81, 82].

Mechanical testing demonstrated consistent yield strengths of roughly 183 MPa and ultimate tensile strengths near 322 MPa (Table 5.4). The reduction in UTS for transverse specimens, attributed to grain orientation effects and consistent with the Hall-Petch relationship (Equation 5.1), emphasizes the role of microstructural alignment on mechanical performance. This material compares favorably to Al-5183 alloys without Scandium additions, but has a strength in the range of untempered common space alloys.

Orbital condition simulations further extend model applicability. Figures 5.22–5.24 illustrate quasi-steady thermal profiles for shielded, hot, and cold scenarios, respectively. The impact of environmental heating conditions on the chosen component on thermal profiles was negligible due to the small surface areas and thus low incoming heat flux. For all cooling times simulated, the average workpiece temperatures did not exceed the melting point, and are thus assumed to be stable deposition strategies. Melt pool temperatures in the first few layers are again observed to be significantly underestimated, but

since both the laboaratory validation and orbital simulations display the same error, it is assumed that their predictive power for strucutral thermal history is similar.

For full-scale space habitats manufactured by ISAM, it was estimated that the cold orbital case could cause excessive thermal gradients during ISAM, and thus it is recommended to use the hot case for manufacturing. Passive thermal control strategies like rotation of the structure along its longitudinal axis were suggested as a possible solution to uneven heating in the hot case. A concept for a thermal buffer enclosure was proposed to further increase the equilibrium temperature of the structure and smooth out thermal oscillations.

In summary, the integrated approach—combining numerical thermal simulations, microstructural and mechanical characterization, and orbital modeling—substantiates the viability of the proposed welding and deposition process for both terrestrial and space applications. These comprehensive results provide a robust foundation for further refinement of thermal models and process parameters, which are critical for the advancement of in-situ additive manufacturing in space environments.

6

Conclusion and Recommendations

This discussion chapter provides a general overview of the findings and implications of the research conducted on ISAM.

An integrated analysis of the experimental and numerical investigations confirms that the developed thermal model is capable of capturing the average thermal history of the workpiece under terrestrial conditions with reasonable accuracy, allowing for preliminary orbital models to be developed. Although the melt pool temperatures remain underestimated relative to expected values, the model successfully reproduces the general thermal trends observed in thermocouple measurements, with error bounds within approximately 10°C. This validation across both small- and large-scale experiments lends confidence to the application of the model for simulating the thermal environments in In-Space Additive Manufacturing (ISAM).

To answer the initially posed research questions, the following points are considered:

1. How well can analogous terrestrial experiments in combination with computational simulations be used to predict ISAM performance?

   The accuracy of the developed thermal model was validated against analogous high-temperature experiments, leading to the expectation that this same model, using ISAM conditions, would be able to predict the macro-scale thermal history of ISAM components taking only the major sources of heat into account. However, due to the lumped-element nature of the model, it is not able to predict the fine-scale thermal gradients and thus the microstructural evolution during the deposition process. Further environmental conditions like microgravity, vacuum, and radiation were also simplified, but are not expected to have a significant impact on the thermal behavior of the deposited material.

2. What are the optimal process parameters for Wire Arc Additive Manufacturing (WAAM) in space-analogous conditions?

   The optimal process parameters for the chosen Al-5183+0.3%Sc alloy are reported in Table 4.9, and yielded stable performance during the high-temperature experiments. The degree to which this experiment was analogous to actual ISAM conditions is limited, as the only condition that was altered was the raised initial temperature and decrease in convective cooling for the baseplate. Further experiments in more similar conditions (e.g. a thermal vacuum chamber) are needed to find further optimal process parameters.

3. How do printing parameters (heat input, geometry, cooling times) affect thermal dynamics during ISAM?

   The main printing parameter investigated was the interlayer cooling time, which was found to have an impact on the average temperature of the workpiece and baseplate in the steady-state solution where thermal profiles were found to be roughly periodic. The largest decrease in average temperatures, 63.8 °C, was between 60 and 120 seconds, with successive increases in cooling time resulting in smaller decreases. Other parameters were not iterated upon under ISAM conditions, which is left for future work.

4. What is the thermal design space for ISAM-printed components, and what thermal control strategies would be required for future mission designers?

The effect of different environmental heating conditions (high constant flux, periodic flux, and no flux) on the thermal behavior of the workpiece was investigated and found to have minimal impact on the thermal profile of the process for small components. The thermal design space for average temperatures of the workpiece under different cooling times was found to range from roughly 300 to 430 °C, with pre-heating of the baseplate to 200 °C decreasing the time required to reach steady-state conditions. Removing pre-heating is not expected to change the periodic steady-state solution of the thermal profile, and thus is of limited utility for controlling temperatures during ISAM. For larger components, on the scale of several meters, the equilibrium temperature of the structure was found to be strongly related to environmental heating conditions. Full shielding of the print volume during deposition would result in excessively low equilibrium temperatures, and orbits with large eclipse periods introduce large equilibrium temperature oscillations that would negatively impact the stability of the deposition process, leading to orbits with constant solar heating to be the most stable and thus preferred for ISAM. Extra considerations are required for radiative heat transfer inside large hollow structures, and passive thermal control strategies like slow rotation of the structure are recommended to avoid thermal gradients due to uneven heating.

Notably, the use of Sc-modified alloys appears to offer an enhanced resistance to grain coarsening at elevated temperatures, thereby mitigating some of the detrimental effects associated with prolonged thermal exposure in low-gravity environments. The strength of as-deposited ISAM structures highly depends on the microstructural evolution during the deposition process since post-processing of large structures is impractical, particularly in orbit. Therefore, it is important to consider materials that can be benefited by high-temperature processing during manufacturing, like Aluminum alloys with precipitating alloying elements like Scandium, Manganese, and Zirconium.

The numerical framework presented herein not only aids in delineating the thermal design space for ISAM-printed components but also establishes a foundation for future refinements. Moreover, the insights gained regarding radiative heat losses in orbital conditions—encoded through the application of advanced thermal boundary condition formulations—underscore the potential for adaptive thermal control strategies that optimize process performance during in-space fabrication. Understanding the thermal behavior of a deposition process without thermal control allows for precise control requirements to be formulated.

The model developed using lumped-element methods and heating inherently cannot capture the full thermal behavior of the melt pool during deposition. However, the objective of this work was not to extend thermal predictions to this scale, but rather to provide a platform that allows for the investigation of boundary condition validity in several different conditions, be they in the laboratory or in space. The value of this model is its extendability to more complex geometries and conditions, which can be generated quickly and iterated upon to find reasonable approximations for a number of different metal DED processes, as the discrete element heating is process agnostic.

It is important to acknowledge that the scope of this work is limited, primarily focusing on the thermal dynamics and material behavior of metal AM in microgravity conditions. While the results obtained offer valuable insights, they represent an initial foray into the field of ISAM, serving as a foundational step for future researchers. The findings presented herein are intended to stimulate further investigation and exploration, ultimately contributing to the advancement of ISAM technologies and methodologies in the context of space manufacturing.

6.1. Limitations

The fundamental limitation of this work was the lack of experimental equipment capable of recreating the environmental conditions in orbit, potentially undermining the validity of the results regarding thermal and structural integrity. The small-scale WAAM-centric experiments were chosen due to this being the available equipment at the time of the experiments.

The Wire Arc Additive Manufacturing (WAAM) process, while promising, is not currently employed in space environments. This limitation raises concerns regarding the applicability of the findings, as the deposition characteristics and resulting microstructure observed on Earth may not accurately reflect those encountered in actual space operations.

Furthermore, the study was constrained by computational limitations, necessitating the use of small-scale models for simulation. The maximum simulation time was 24 hours, with a maximum CPU core count of 64. This restriction may have impacted the fidelity of the results, as larger and more complex geometries could provide a more representative understanding of thermal behaviour during ISAM.

The research also did not account for critical orbital environmental conditions, such as Atomic Oxygen (ATOX) and radiation, which may significantly influence the effects on the melt pool during deposition. The simplification of the melt pool to a lumped-element model further limits the accuracy of thermal behaviour predictions, as it fails to capture the intricate dynamics of heat transfer during the deposition process.

Another limitation of this work was the lack of investigation into the structural effects of thermal history on the structure. Distortions and stress modeling were not performed due to limitations on time during the thesis timeframe.

6.2. Future Work

In order to more fully capture the thermal behavior during ISAM, metal AM methods and testing enviornments more similar to actual space conditions are needed. This could encompass a thermal vacuum chamber where EBF3 or LWDED is performed, and potentially the addition of a radiation source to simulate the effects of the space environment on the deposited material. The addition of microgravity to Earth-based analogous experiments is more of a challenge, and ultimately, the best test location is on-site in orbit.

Future research should prioritize a comprehensive review of the added value of ISAM for various components and structure types, providing insights into the technology's potential benefits and limitations across different applications. Moreover, the thickness of the deposited material in the experiments was considerably greater than the structural thicknesses typically employed in space habitats, primarily due to the need for enhanced structural protection. Exploring advanced shielding strategies during the printing process could yield significant reductions in the required thickness of resulting structures, enhancing the efficiency of ISAM in space environments.

A broader investigation into diverse alloys is warranted to expand the design space available to ISAM space structure designers, potentially leading to the identification of materials that offer superior performance under unique space conditions. Additionally, a wider range of thermal control strategies, including both active and passive methods, should be considered to manage thermal behaviour during manufacturing and ensure the integrity of final structures.

The evaluation of alternative simulation packages, such as Multiphysics COMSOL, is essential to address the full scope of the problem, as these tools may provide enhanced capabilities for modelling multi-physics phenomena, integrating e.g. the effect of radiation on the melt pool. Modeling the melt pool accurately is difficult to do alongside structure-level thermal behavior due to the much higher computational cost of the former, presenting the opportunity for finding approximations for melt pool behavior that can be used in more coarse thermal models. A more comprehensive characterization of cooling rates in cryogenic vacuum environments is needed for future correlations with material properties.

Developing full-scale models for simulation, as mentioned in Section 5.5.1, is also crucial for understanding thermal behaviour in realistic scenarios, facilitating the exploration of complex geometries relevant to actual space infrastructure.

The need for more experimental data regarding microgravity deposition conditions is critical to enhance understanding of processes involved in LWDED and EBF3, which are currently employed in space applications. WAAM has not been tested extensively in vacuum environments, and thus is an unlikely first choice for ISAM. Much more likely process candidates are EBF3 and LWDED, which have both been previously researched in microgravity conditions. The weld beads, heat-affected zones, and resulting microstructures of these processes have been shown to be significantly different to that of WAAM, and thus more work is needed to correlate large-scale simulation results to microstructural development.

Another point of future improvement is a more accurate modeling of thermo-optical properties of

the deposited material. Emissivity is dependent on temperature and phase changes, and thus a more accurate model would take this into account. Consideration should also be given to the actual robotic mechanisms that will perform the printing in space, as understanding their capabilities and limitations will help further the possible conditions under which ISAM can be performed.

References

[1] Erik Kulu. "In-Space Manufacturing - 2022 Industry Survey and Commercial Landscape". In: ().

[2] Erik Kulu. "In-Space Economy in 2023 - Statistical Overview and Trends". In: *th International Astronautical Congress* (2023).

[3] Alejandro E. Trujillo et al. "Feasibility Analysis of Commercial In-Space Manufacturing Applications". In: *AIAA SPACE and Astronautics Forum and Exposition*. Orlando, FL: American Institute of Aeronautics and Astronautics, Sept. 2017. ISBN: 978-1-62410-483-1. DOI: 10.2514/6.2017-5360. (Visited on 06/10/2024).

[4] Paul Gradl et al. "Robust Metal Additive Manufacturing Process Selection and Development for Aerospace Components". In: *Journal of Materials Engineering and Performance* 31.8 (Aug. 2022), pp. 6013–6044. ISSN: 1059-9495, 1544-1024. DOI: 10.1007/s11665-022-06850-0. (Visited on 09/04/2023).

[5] Johnnieew Zhong Li et al. "Review of Wire Arc Additive Manufacturing for 3D Metal Printing". In: *International Journal of Automation Technology* 13.3 (May 2019), pp. 346–353. ISSN: 1883-8022, 1881-7629. DOI: 10.20965/ijat.2019.p0346. (Visited on 09/04/2023).

[6] Miguel Hoffmann and Alaa Elwany. "In-Space Additive Manufacturing: A Review". In: *Journal of Manufacturing Science and Engineering* 145.2 (Feb. 2023), p. 020801. ISSN: 1087-1357, 1528-8935. DOI: 10.1115/1.4055603. (Visited on 04/25/2024).

[7] David Svetlizky et al. "Directed Energy Deposition (DED) Additive Manufacturing: Physical Characteristics, Defects, Challenges and Applications". In: *Materials Today* 49 (Oct. 2021), pp. 271–295. ISSN: 13697021. DOI: 10.1016/j.mattod.2021.03.020. (Visited on 06/14/2024).

[8] Jens Guenster. *METHOD FOR STABILIZING A POWDER BED BY MEANS OF VACUUM FOR ADDITIVE MANUFACTURING*. Mar. 2017. (Visited on 06/19/2024).

[9] Karen M B Taminger. "Metal Additive Manufacturing In Space". In: ().

[10] *First Metal Part 3D Printed in Space*. June 2024.

[11] Dmitry G Luchinsky et al. "Analysis of Arc Welding Process in Space". In: ().

[12] F42 Committee. *Standard Guide for Directed Energy Deposition of Metals*. DOI: 10.1520/F3187-16. (Visited on 06/19/2024).

[13] Georgi M Mladenov, Elena G Koleva, and Katia J Vutova. "Heat Transfer and Weld Geometry at Electron Beam Welding". In: (2007).

[14] Karen M B Taminger and Robert A Hafley. "ELECTRON BEAM FREEFORM FABRICATION: A RAPID METAL DEPOSITION PROCESS". In: (2003).

[15] Murat Sarıkaya et al. "A Review on Aluminum Alloys Produced by Wire Arc Additive Manufacturing (WAAM): Applications, Benefits, Challenges and Future Trends". In: *Journal of Materials Research and Technology* 33 (Nov. 2024), pp. 5643–5670. ISSN: 22387854. DOI: 10.1016/j.jmrt.2024.10.212. (Visited on 02/12/2025).

[16] Kun Li et al. "Additive Manufacturing of Ultra-High Strength Steels: A Review". In: *Journal of Alloys and Compounds* 965 (Nov. 2023), p. 171390. ISSN: 09258388. DOI: 10.1016/j.jallcom.2023.171390. (Visited on 07/30/2024).

[17] Zhu Liang et al. "Characteristics of Metal Droplet Transfer in Wire-Arc Additive Manufacturing of Aluminum Alloy". In: *The International Journal of Advanced Manufacturing Technology* 99.5-8 (Nov. 2018), pp. 1521–1530. ISSN: 0268-3768, 1433-3015. DOI: 10.1007/s00170-018-2604-7. (Visited on 07/31/2024).

[18] Harley Stinson et al. “Comparison of Properties and Bead Geometry in MIG and CMT Single Layer Samples for WAAM Applications”. In: *Metals* 11.10 (Sept. 2021), p. 1530. ISSN: 2075-4701. DOI: 10.3390/met11101530. (Visited on 09/19/2023).

[19] *Super Active Tawers*. Jan. 2018. (Visited on 07/31/2024).

[20] Laserax. *Understanding Common Aluminum Alloys Series*. https://www.laserax.com/blog/understanding-common-aluminum-alloys-series. July 2017. (Visited on 07/07/2024).

[21] None Available. *Materials Data on Al by Materials Project*. 2020. DOI: 10.17188/1189564. (Visited on 02/04/2025).

[22] Nor Ana Rosli et al. “Review on Effect of Heat Input for Wire Arc Additive Manufacturing Process”. In: *Journal of Materials Research and Technology* 11 (Mar. 2021), pp. 2127–2145. ISSN: 22387854. DOI: 10.1016/j.jmrt.2021.02.002. (Visited on 06/19/2024).

[23] Guo Xian et al. “Effect of Heat Input on Microstructure and Mechanical Property of Wire-Arc Additive Manufactured Ti-6Al-4V Alloy”. In: *Welding in the World* 66.5 (May 2022), pp. 847–861. ISSN: 0043-2288, 1878-6669. DOI: 10.1007/s40194-021-01248-3. (Visited on 06/20/2024).

[24] Junyi Cui et al. “WAAM Process for Metal Block Structure Parts Based on Mixed Heat Input”. In: *The International Journal of Advanced Manufacturing Technology* 113.1-2 (Mar. 2021), pp. 503–521. ISSN: 0268-3768, 1433-3015. DOI: 10.1007/s00170-021-06654-x. (Visited on 06/20/2024).

[25] Nor Ana Rosli et al. “Review on Effect of Heat Input for Wire Arc Additive Manufacturing Process”. In: *Journal of Materials Research and Technology* 11 (Mar. 2021), pp. 2127–2145. ISSN: 22387854. DOI: 10.1016/j.jmrt.2021.02.002. (Visited on 08/01/2024).

[26] Debasish Das, Dilip Kumar Pratihar, and Gour Gopal Roy. “Cooling Rate Predictions and Its Correlation with Grain Characteristics during Electron Beam Welding of Stainless Steel”. In: *The International Journal of Advanced Manufacturing Technology* 97.5-8 (July 2018), pp. 2241–2254. ISSN: 0268-3768, 1433-3015. DOI: 10.1007/s00170-018-2095-6. (Visited on 05/03/2024).

[27] Zhening Yang et al. “Predicting Melt Pool Dimensions for Wire-Feed Directed Energy Deposition Process”. In: *Integrating Materials and Manufacturing Innovation* 11.4 (Dec. 2022), pp. 532–544. ISSN: 2193-9764, 2193-9772. DOI: 10.1007/s40192-022-00278-z. (Visited on 06/20/2024).

[28] Thomas Stenberg, Eric Lindgren, and Zuheir Barsoum. “Development of an Algorithm for Quality Inspection of Welded Structures”. In: *Proceedings of the Institution of Mechanical Engineers, Part B: Journal of Engineering Manufacture* 226.6 (June 2012), pp. 1033–1041. ISSN: 0954-4054, 2041-2975. DOI: 10.1177/0954405412439138. (Visited on 06/21/2024).

[29] J.W. Elmer. *The Influence of Cooling Rate on the Microstructure of Stainless Steel Alloys*. Tech. rep. UCRL-53934, 5678406. Sept. 1988, UCRL–53934, 5678406. DOI: 10.2172/5678406. (Visited on 06/21/2024).

[30] M. Zubairuddin et al. “Numerical Simulation of Multi-Pass GTA Welding of Grade 91 Steel”. In: *Journal of Manufacturing Processes* 27 (June 2017), pp. 87–97. ISSN: 15266125. DOI: 10.1016/j.jmapro.2017.04.031. (Visited on 06/21/2024).

[31] A. Kumar and T. Debroy. “Tailoring Complex Weld Geometry through Reliable Heat-Transfer and Fluid-Flow Calculations and a Genetic Algorithm”. In: *Metallurgical and Materials Transactions A* 36.10 (Oct. 2005), pp. 2725–2735. ISSN: 1073-5623, 1543-1940. DOI: 10.1007/s11661-005-0269-y. (Visited on 06/22/2024).

[32] Theresa Stanley. *The Vulcan Advanced Hybrid Manufacturing System*. Feb. 2021.

[33] Heng Gu and Lin Li. “Computational Fluid Dynamic Simulation of Gravity and Pressure Effects in Laser Metal Deposition for Potential Additive Manufacturing in Space”. In: *International Journal of Heat and Mass Transfer* 140 (Sept. 2019), pp. 51–65. ISSN: 00179310. DOI: 10.1016/j.ijheatmasstransfer.2019.05.081. (Visited on 07/05/2024).

[34] Renzhi Hu et al. “Thermal Fluid Dynamics of Liquid Bridge Transfer in Laser Wire Deposition 3D Printing”. In: *Science and Technology of Welding and Joining* 24.5 (July 2019), pp. 401–411. ISSN: 1362-1718, 1743-2936. DOI: 10.1080/13621718.2019.1591039. (Visited on 07/07/2024).

[35] N Naden and T J Prater. “A Review of Welding in Space and Related Technologies”. In: ().

[36] Matthew Tyler Moraguez. *Technology Development Targets for Commercial In-Space Manufacturing*. Nov. 2018. (Visited on 06/08/2024).

[37] Harsh G. Bhundiya, Fabien Royer, and Zachary Cordero. "Engineering Framework for Assessing Materials and Processes for In-Space Manufacturing". In: *Journal of Materials Engineering and Performance* 31.8 (Aug. 2022), pp. 6045–6059. ISSN: 1059-9495, 1544-1024. DOI: 10.1007/s11665-022-06755-y. (Visited on 04/25/2024).

[38] Roberto Opromolla et al. "Future In-Orbit Servicing Operations in the Space Traffic Management Context". In: *Acta Astronautica* 220 (July 2024), pp. 469–477. ISSN: 00945765. DOI: 10.1016/j.actaastro.2024.05.007. (Visited on 06/13/2024).

[39] Sunjae Kim et al. "Cryogenic Flow Boiling in Microgravity: Effects of Reduced Gravity on Two-Phase Fluid Physics and Heat Transfer". In: *International Journal of Heat and Mass Transfer* 218 (Jan. 2024), p. 124751. ISSN: 00179310. DOI: 10.1016/j.ijheatmasstransfer.2023.124751. (Visited on 06/13/2024).

[40] *NSS Roadmap to Space Settlement 3rd Edition*. Jan. 2019. (Visited on 06/04/2024).

[41] W Schneider. "Large Space Antenna Systems Technology - 1984 December 4-6, 1984". In: ().

[42] Miria M. Finckenor. *The Researcher's Guid to the ISS: Space Environmental Effects*. (Visited on 06/22/2024).

[43] Jane A Hagaman. "A Survey of Structural Material Issues for a Space Station". In: ().

[44] J. E. Turner. *Atoms, Radiation, and Radiation Protection*. 3rd completely rev. and enl. ed. Physics Textbook. Weinheim: Wiley-VCH, 2007. ISBN: 978-3-527-40606-7.

[45] Ailing Zhang and Yanxiang Li. "Thermal Conductivity of Aluminum Alloys—A Review". In: *Materials* 16.8 (Apr. 2023), p. 2972. ISSN: 1996-1944. DOI: 10.3390/ma16082972. (Visited on 07/03/2024).

[46] admin. *Aluminium at Elevated Temperatures*. https://aluminium-guide.com/aluminium-elevated-temperatures/. May 2013. (Visited on 07/02/2024).

[47] Adam L. Woodcraft. "Predicting the Thermal Conductivity of Aluminium Alloys in the Cryogenic to Room Temperature Range". In: *Cryogenics* 45.6 (June 2005), pp. 421–431. ISSN: 00112275. DOI: 10.1016/j.cryogenics.2005.02.003. (Visited on 07/03/2024).

[48] Mitra Taghizadeh and Zheng H. Zhu. "A Comprehensive Review on Metal Laser Additive Manufacturing in Space: Modeling and Perspectives". In: *Acta Astronautica* 222 (Sept. 2024), pp. 403–421. ISSN: 00945765. DOI: 10.1016/j.actaastro.2024.06.027. (Visited on 07/04/2024).

[49] C.P. Paul et al. "Laser Rapid Manufacturing on Vertical Surfaces: Analytical and Experimental Studies". In: *Surface and Coatings Technology* 224 (June 2013), pp. 18–28. ISSN: 02578972. DOI: 10.1016/j.surfcoat.2013.02.044. (Visited on 07/05/2024).

[50] C. Garb, M. Leitner, and F. Grün. "Effect of Elevated Temperature on the Fatigue Strength of Casted AlSi8Cu3 Aluminium Alloys". In: *Procedia Structural Integrity* 7 (2017), pp. 497–504. ISSN: 24523216. DOI: 10.1016/j.prostr.2017.11.118. (Visited on 07/03/2024).

[51] Farhad B. Bahaideen et al. "Fatigue Behaviour of Aluminum Alloy at Elevated Temperature". In: *Modern Applied Science* 3.4 (Mar. 2009), p52. ISSN: 1913-1852, 1913-1844. DOI: 10.5539/mas.v3n4p52. (Visited on 07/03/2024).

[52] Amal Masmoudi, Rodolphe Bolot, and Christian Coddet. "Investigation of the Laser–Powder–Atmosphere Interaction Zone during the Selective Laser Melting Process". In: *Journal of Materials Processing Technology* 225 (Nov. 2015), pp. 122–132. ISSN: 09240136. DOI: 10.1016/j.jmatprotec.2015.05.008. (Visited on 07/05/2024).

[53] X. He and J. Mazumder. "Transport Phenomena during Direct Metal Deposition". In: *Journal of Applied Physics* 101.5 (Mar. 2007), p. 053113. ISSN: 0021-8979, 1089-7550. DOI: 10.1063/1.2710780. (Visited on 07/05/2024).

[54] Alexander Klassen, Vera E Forster, and Carolin Körner. "A Multi-Component Evaporation Model for Beam Melting Processes". In: *Modelling and Simulation in Materials Science and Engineering* 25.2 (Feb. 2017), p. 025003. ISSN: 0965-0393, 1361-651X. DOI: 10.1088/1361-651X/aa5289. (Visited on 07/05/2024).

[55] Seyyed Mohammad Ali Noori Rahim Abadi et al. "CFD-Based Feasibility Study of Laser-Directed Energy Deposition With a Metal Wire for On-Orbit Manufacturing". In: *Frontiers in Space Technologies* 3 (July 2022), p. 880012. ISSN: 2673-5075. DOI: 10.3389/frspt.2022.880012. (Visited on 07/05/2024).

[56] Liqun Li et al. "Numerical and Experimental Study on Keyhole and Melt Flow Dynamics during Laser Welding of Aluminium Alloys under Subatmospheric Pressures". In: *International Journal of Heat and Mass Transfer* 133 (Apr. 2019), pp. 812–826. ISSN: 00179310. DOI: 10.1016/j.ijheatmasstransfer.2018.12.165. (Visited on 07/05/2024).

[57] Perm National Research Polytechnic University, Russian Federation et al. "Numerical Analysis of the Process of Electron Beam Additive Deposition with Vertical Feed of Wire Material". In: *Metal Working and Material Science* 24.3 (Sept. 2022), pp. 6–21. ISSN: 19946309, 2541819X. DOI: 10.17212/1994-6309-2022-24.3-6-21. (Visited on 07/04/2024).

[58] Fatih Sikan et al. "Thermo-Mechanical Modeling of Wire-Fed Electron Beam Additive Manufacturing". In: *Materials* 14.4 (Feb. 2021), p. 911. ISSN: 1996-1944. DOI: 10.3390/ma14040911. (Visited on 07/05/2024).

[59] Donghong Ding et al. "The Well-Distributed Volumetric Heat Source Model for Numerical Simulation of Wire Arc Additive Manufacturing Process". In: *Materials Today Communications* 27 (June 2021), p. 102430. ISSN: 23524928. DOI: 10.1016/j.mtcomm.2021.102430. (Visited on 07/05/2024).

[60] Conny Lampa et al. "An Analytical Thermodynamic Model of Laser Welding". In: *Journal of Physics D: Applied Physics* 30.9 (May 1997), pp. 1293–1299. ISSN: 0022-3727, 1361-6463. DOI: 10.1088/0022-3727/30/9/004. (Visited on 07/07/2024).

[61] *APDL Command Reference*. ANSYS, Inc. Canonsburg, PA, July 2024.

[62] *ANSYS Mechanical APDL Element Reference*. ANSYS, Inc. Canonsburg, PA, Nov. 2013.

[63] *ISS Harmony Module Factsheet*. Jan. 2007. (Visited on 09/17/2024).

[64] "International Docking System Standard (IDSS) - Interface Definition Document (IDD)". In: (2016).

[65] Kelly. "Elasticity Applications -Presure Vessels". In: *Solid Mechanics Part 1*. (Visited on 08/14/2024).

[66] Engineers Edge and Engineers Edge LLC. *Stress in Pressure Vessel Flanged or Dished Head Section Seam Equation and Calculator*. https://www.engineersedge.com/pressure,045vessel/stress_in_pressure_vessel_flanged_14 (Visited on 09/17/2024).

[67] S. Ryan and E.L. Christiansen. "A Ballistic Limit Analysis Programme for Shielding against Micrometeoroids and Orbital Debris". In: *Acta Astronautica* 69.5-6 (Sept. 2011), pp. 245–257. ISSN: 0094-5765. DOI: 10.1016/j.actaastro.2011.04.012. (Visited on 09/17/2024).

[68] Kayleigh Fowler and Filipe Teixeira-Dias. "Hybrid Shielding for Hypervelocity Impact of Orbital Debris on Unmanned Spacecraft". In: *Applied Sciences* 12.14 (July 2022), p. 7071. ISSN: 2076-3417. DOI: 10.3390/app12147071. (Visited on 06/06/2024).

[69] Isaac J Dr-01 Usaf Afmc Afrl/Rvsv Foster. "Small Satellite Thermal Modeling Guide". In: ().

[70] Steven Rickman. *Introduction to On-Orbit Thermal Environments*. NASA Engineering and Safety Center, Aug. 2014. (Visited on 08/19/2024).

[71] Robert E. Smith. "Environmental Control of Manned Space Vehicles". In: *Advances in Space Science and Technology*. Vol. 5. Elsevier, 1963, pp. 87–142. ISBN: 978-1-4831-9963-4. DOI: 10.1016/B978-1-4831-9963-4.50010-5. (Visited on 02/09/2025).

[72] *Atmospheric Absorbance of CO2 and Impact of Increaseing Concentration*. https://www.physicsforums.com/threads/atm absorbance-of-co2-and-impact-of-increaseing-concentration.979447/. Oct. 2019. (Visited on 02/06/2025).

[73] J N DuPONT and A R Marder. "Thermal Efficiency of Arc Welding Processes". In: ().

[74] Andreas Richter et al. "Real-Time Measurement of Temperature and Volume of the Weld Pool in Wire-Arc Additive Manufacturing". In: *Measurement: Sensors* 17 (Oct. 2021), p. 100060. ISSN: 26659174. DOI: 10.1016/j.measen.2021.100060. (Visited on 02/09/2025).

[75] Taisiya Ponomareva et al. “Wire Arc Additive Manufacturing of Al-Mg Alloy with the Addition of Scandium and Zirconium”. In: *Materials* 14.13 (June 2021), p. 3665. ISSN: 1996-1944. DOI: 10.3390/ma14133665. (Visited on 09/17/2024).

[76] K. C. Mills. *Recommended Values of Thermophysical Properties for Selected Commercial Alloys*. Cambridge: Woodhead, 2002. ISBN: 978-1-85573-569-9 978-0-87170-753-6.

[77] July 2008.

[78] Günter Petzow, Günter Petzow, and Günter Petzow. *Metallographic Etching: Techniques for Metallotraphy, Ceramography, Plastography*. 2. ed., 1. print. Materials Park, Ohio: ASM International, 1999. ISBN: 978-0-87170-633-1.

[79] *Metallic Materials - Tensile Testing - Part 1: Method of Test at Room Temperature*. Nov. 2019.

[80] Xingwang Bai et al. “Numerical Analysis of Heat Transfer and Fluid Flow in Multilayer Deposition of PAW-based Wire and Arc Additive Manufacturing”. In: *International Journal of Heat and Mass Transfer* 124 (Sept. 2018), pp. 504–516. ISSN: 00179310. DOI: 10.1016/j.ijheatmasstransfer.2018.03.085. (Visited on 03/10/2025).

[81] Bolun Dong et al. “Microstructures and Mechanical Properties of Wire Arc Additive Manufactured 5183-Al: Influences of Deposition Dimensions”. In: *CIRP Journal of Manufacturing Science and Technology* 35 (Nov. 2021), pp. 744–752. ISSN: 17555817. DOI: 10.1016/j.cirpj.2021.08.014. (Visited on 02/14/2025).

[82] Lu Li et al. “Investigation on the Microstructure and Mechanical Properties of Multi-layer and Multi-pass Al Alloy Deposition Based on Cold Metal Transfer Technology”. In: *Journal of Materials Engineering and Performance* (June 2024). ISSN: 1059-9495, 1544-1024. DOI: 10.1007/s11665-024-09688-w. (Visited on 02/14/2025).

[83] Thomas Dorin et al. “Aluminium Scandium Alloys”. In: *Fundamentals of Aluminium Metallurgy*. Elsevier, 2018, pp. 439–494. ISBN: 978-0-08-102063-0. DOI: 10.1016/B978-0-08-102063-0.00012-6. (Visited on 02/16/2025).

[84] Socorro Valdez Rodríguez et al. “Solidification Physics and Microstructure: A Study of AlMg and AlMgSi Alloys by Vortex Method”. In: *Solidification*. IntechOpen, Mar. 2018. ISBN: 978-953-51-3906-5. DOI: 10.5772/intechopen.72763. (Visited on 02/04/2025).

[85] *Aluminum Alloy Hardness Chart: HW, HB, HV, HRB, HBA | MachineMFG*. https://www.machinemfg.com/aluminum-alloy-hardness-chart/. Nov. 2024. (Visited on 02/20/2025).

[86] Takayuki Koizumi and Mitsutoshi Kuroda. “Grain Size Effects in Aluminum Processed by Severe Plastic Deformation”. In: *Materials Science and Engineering: A* 710 (Jan. 2018), pp. 300–308. ISSN: 09215093. DOI: 10.1016/j.msea.2017.10.077. (Visited on 02/16/2025).

[87] *WixSteel Industrial Aluminum Alloy Products Catalogue*. https://www.wixsteel.com/products/aluminum-alloy. (Visited on 02/20/2025).

[88] Steven Rickman. *Form Factors Grey Bodies and Radiation*. Thermal and Fluids Analysis Workshop, NASA, Aug. 2012. (Visited on 02/24/2025).

[89] H Leuenberger and R A Person. “Compilation of Radiation Shape Factors for Cylindrical Assemblies”. In: ().

A

APDL Source Code

All source code can be found at the following github repository: `https://github.com/ulfkemmsies/in-space-AM-thermal-modeling`

B

Orbital Heat Load Diagrams

Hot Case Heat Load Diagrams

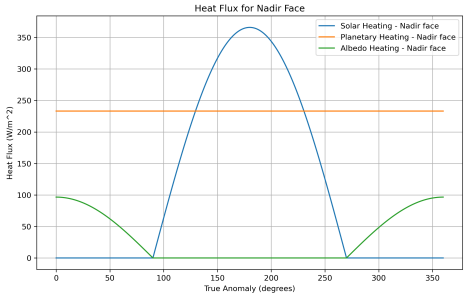


Figure B.1: Nadir face heat load for the hot case

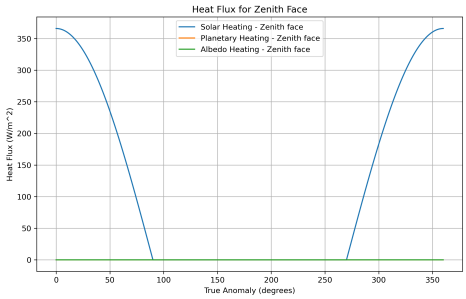


Figure B.2: Zenith face heat load for the hot case

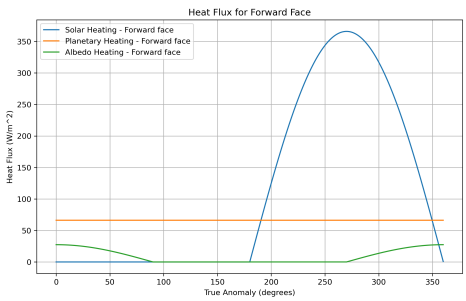


Figure B.3: Forward face heat load for the hot case

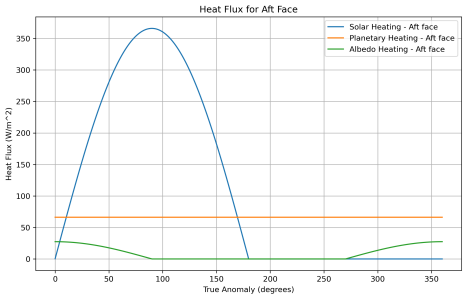


Figure B.4: Aft face heat load for the hot case

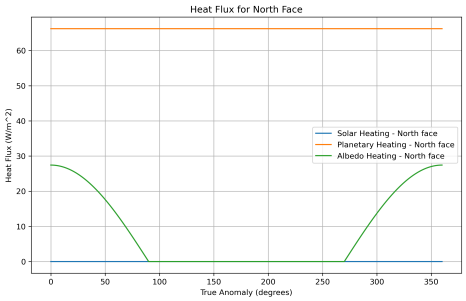


Figure B.5: North face heat load for the hot case

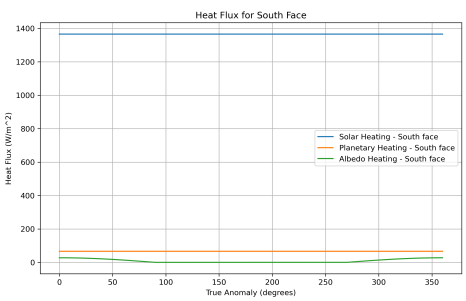


Figure B.6: South face heat load for the hot case

Cold Case Heat Load Diagrams

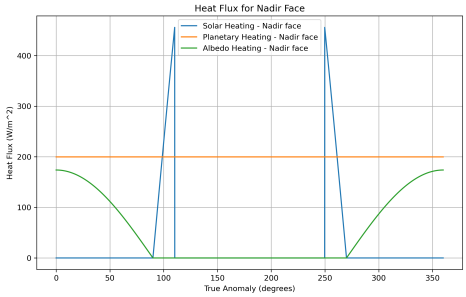


Figure B.7: Nadir face heat load for the cold case

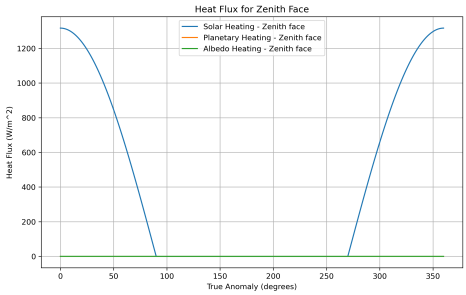


Figure B.8: Zenith face heat load for the cold case

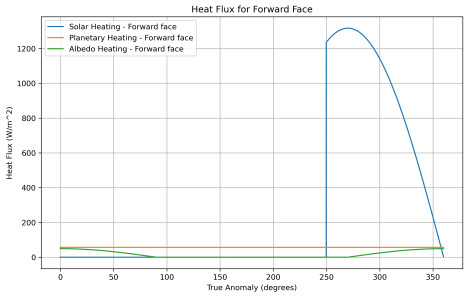


Figure B.9: Forward face heat load for the cold case

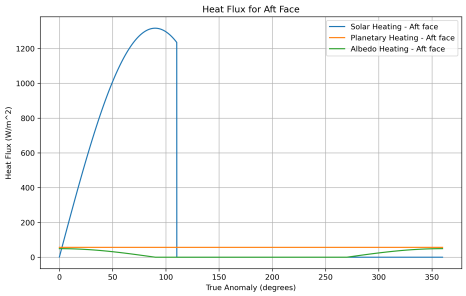


Figure B.10: Aft face heat load for the cold case

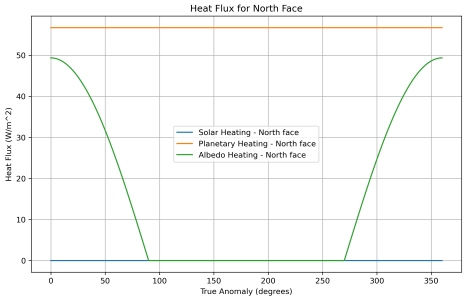


Figure B.11: North face heat load for the cold case

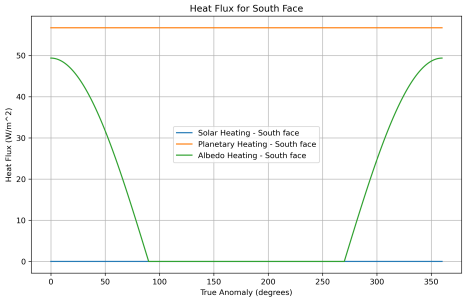


Figure B.12: South face heat load for the cold case

C
Simulation Results

C.1. Orbital Simulation Results
C.1.1. Shielded Case

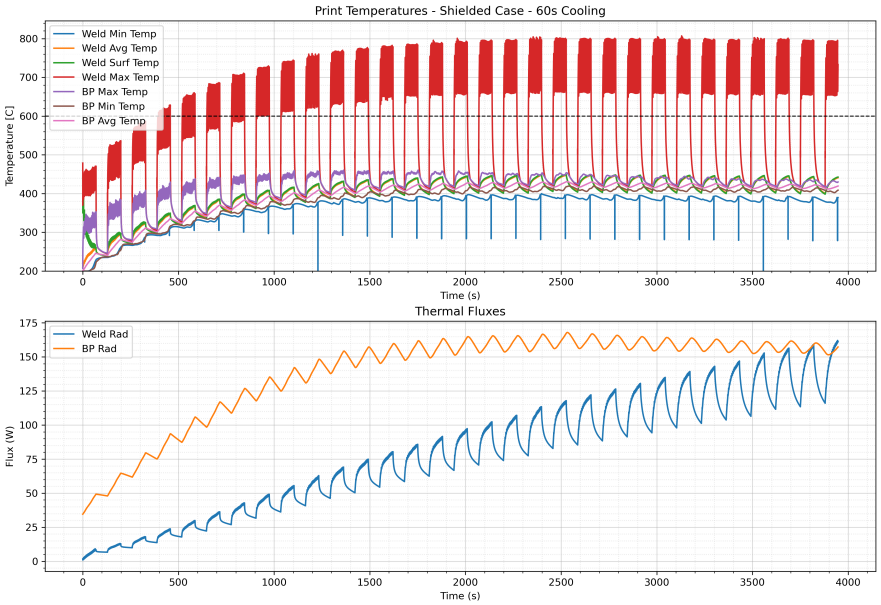


Figure C.1: Full orbit simulation results for the shielded case with 60 seconds of cooling

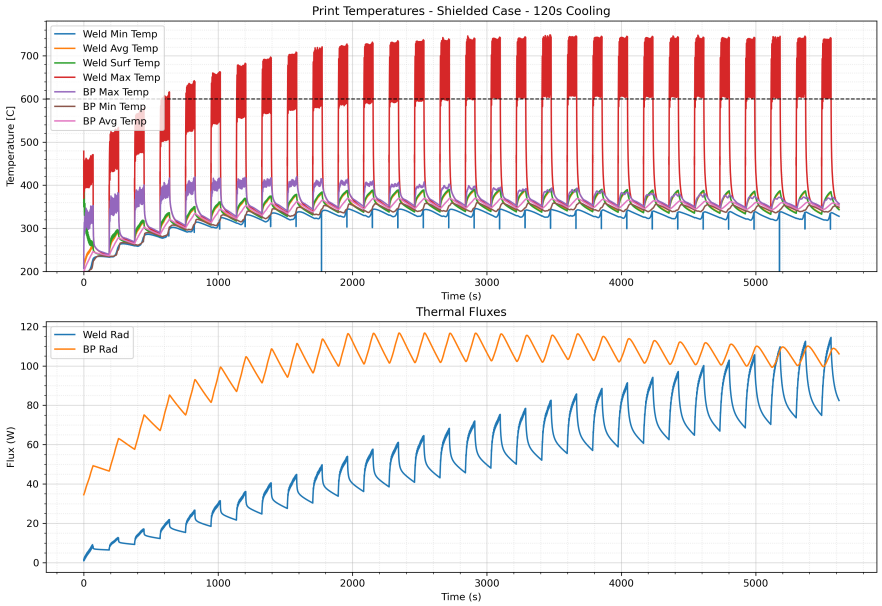


Figure C.2: Full orbit simulation results for the shielded case with 120 seconds of cooling

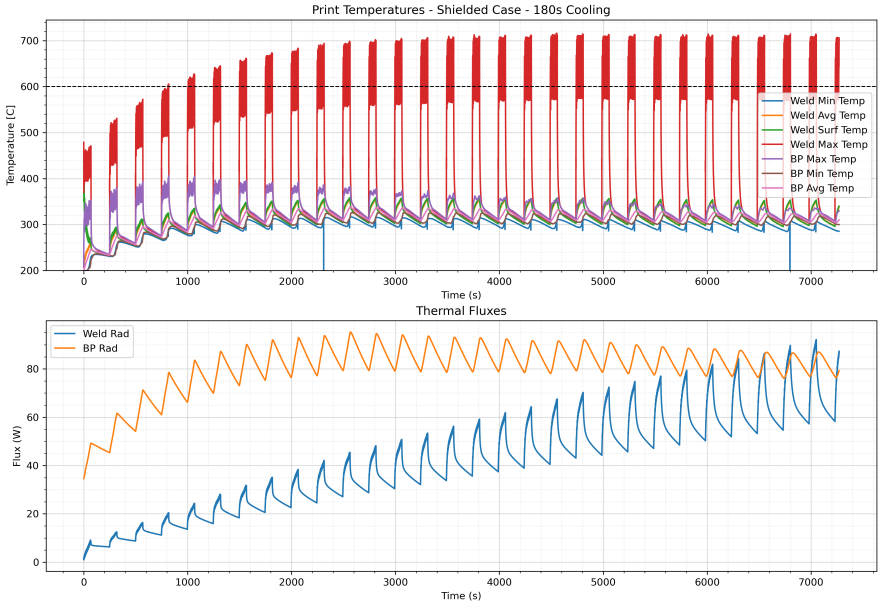


Figure C.3: Full orbit simulation results for the shielded case with 180 seconds of cooling

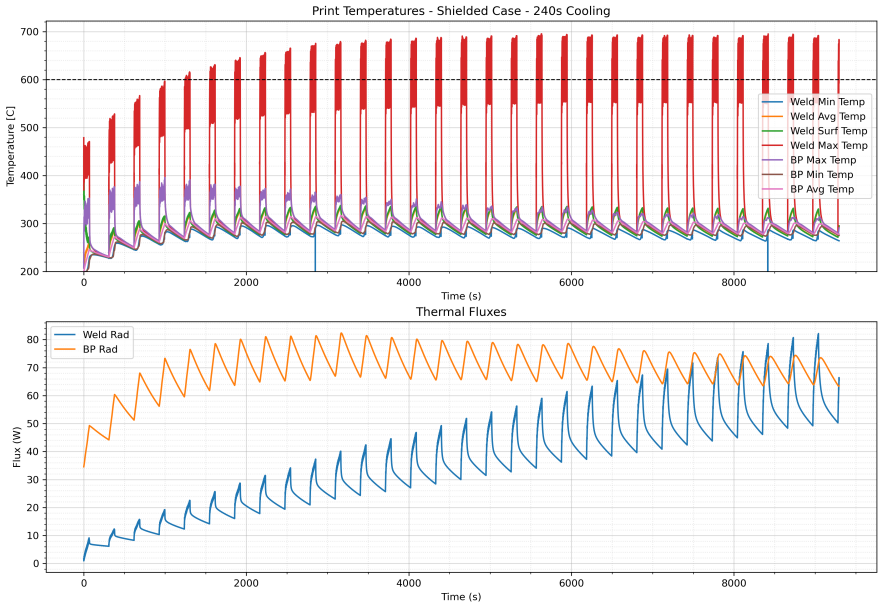


Figure C.4: Full orbit simulation results for the shielded case with 240 seconds of cooling

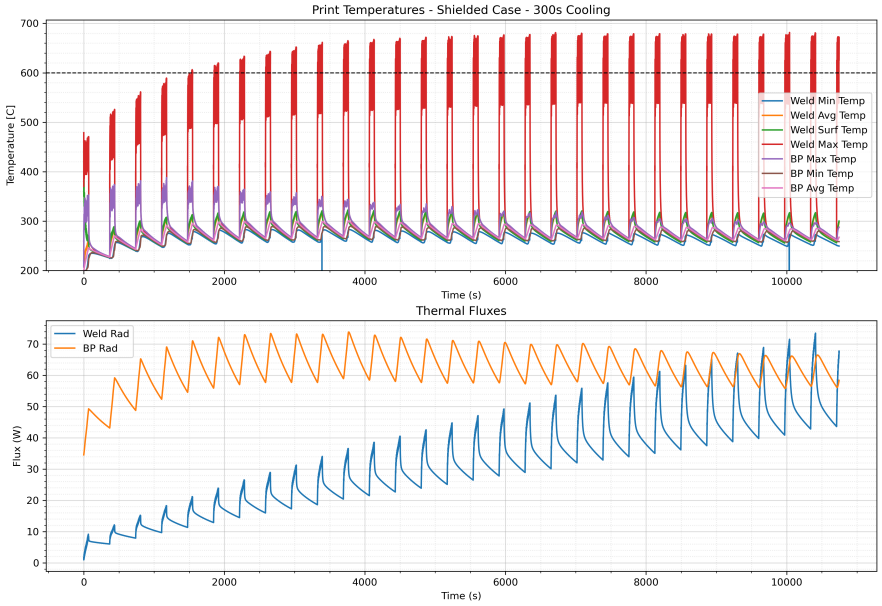


Figure C.5: Full orbit simulation results for the shielded case with 300 seconds of cooling

C.1.2. Hot Case

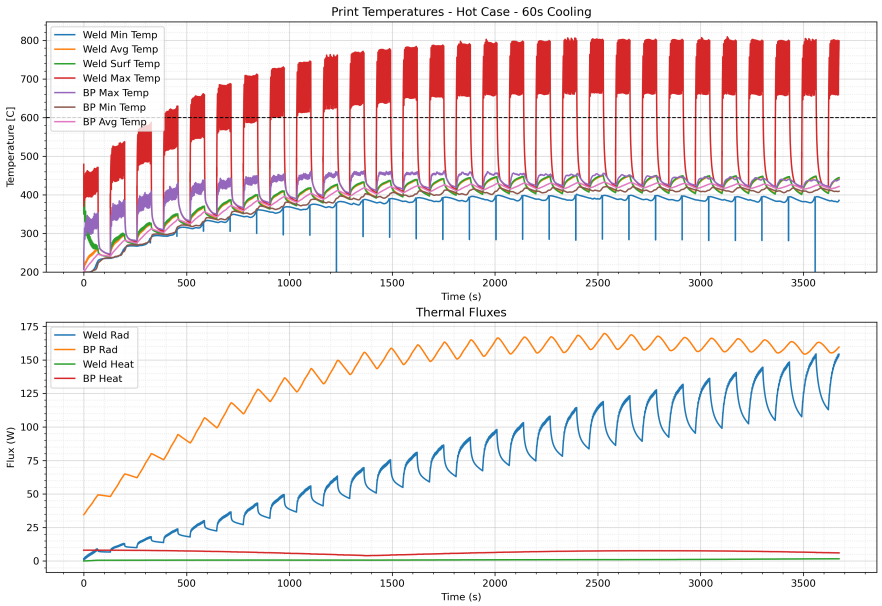


Figure C.6: Full orbit simulation results for the hot case with 60 seconds of cooling

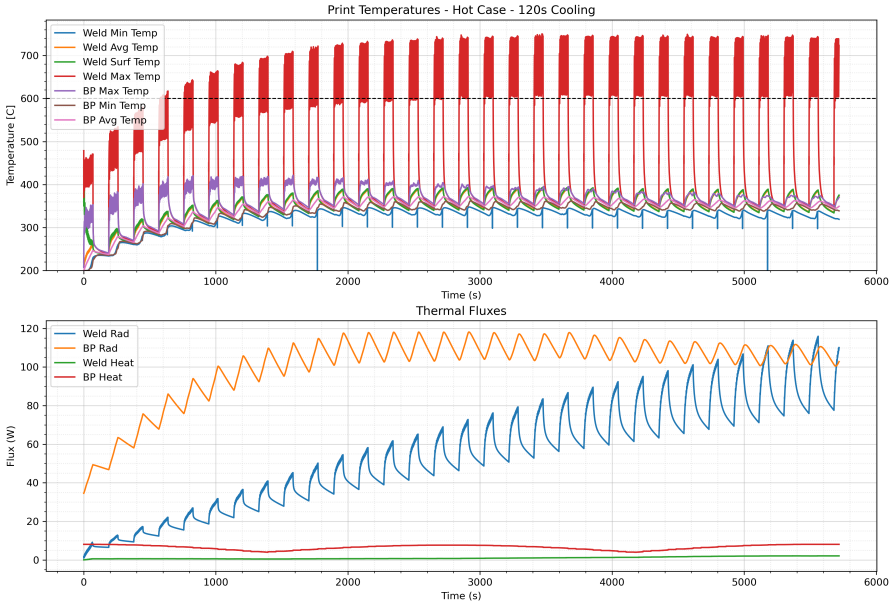


Figure C.7: Full orbit simulation results for the hot case with 120 seconds of cooling

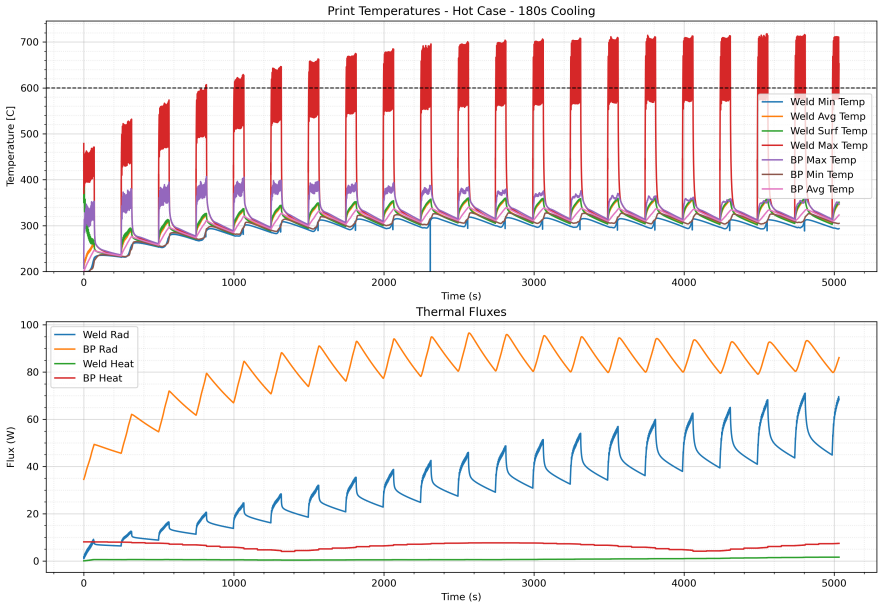


Figure C.8: Full orbit simulation results for the hot case with 180 seconds of cooling

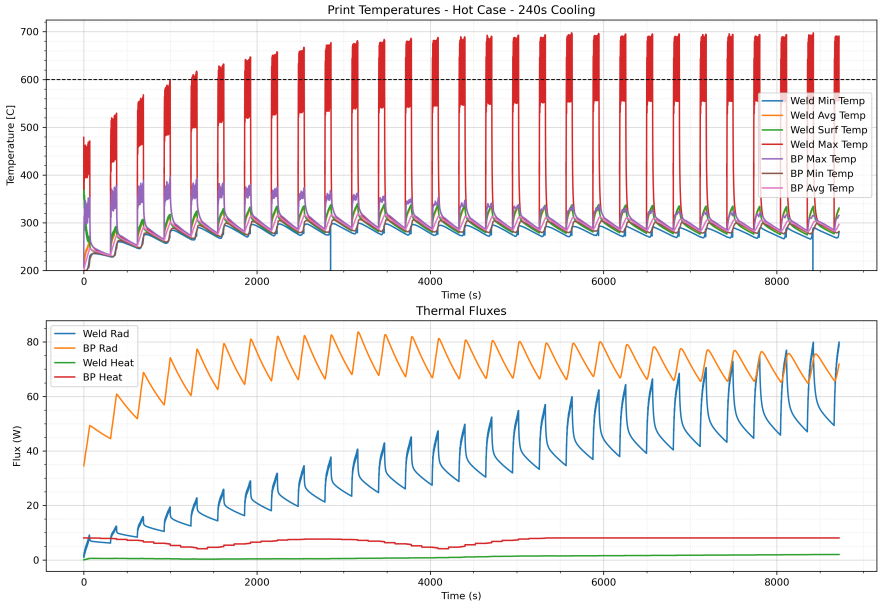


Figure C.9: Full orbit simulation results for the hot case with 240 seconds of cooling

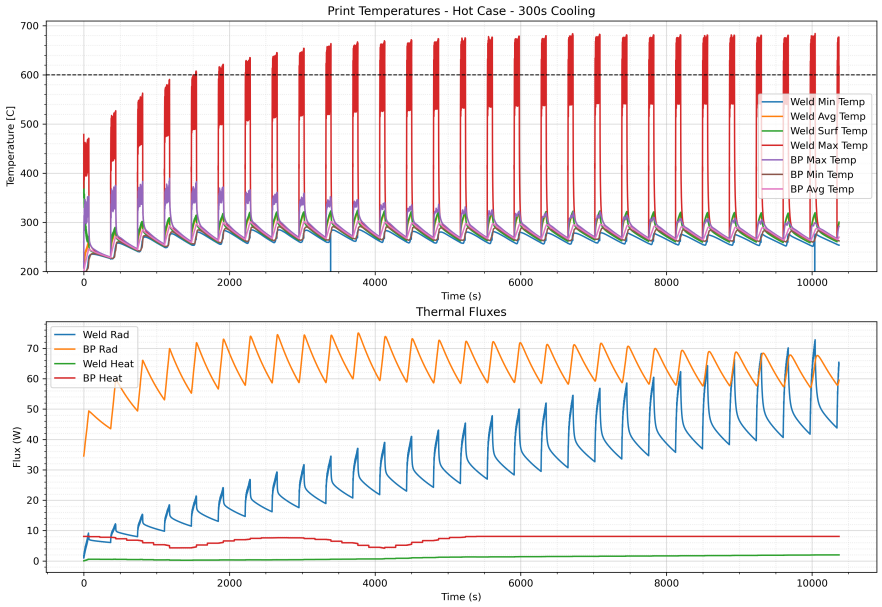


Figure C.10: Full orbit simulation results for the hot case with 300 seconds of cooling

C.1.3. Cold Case

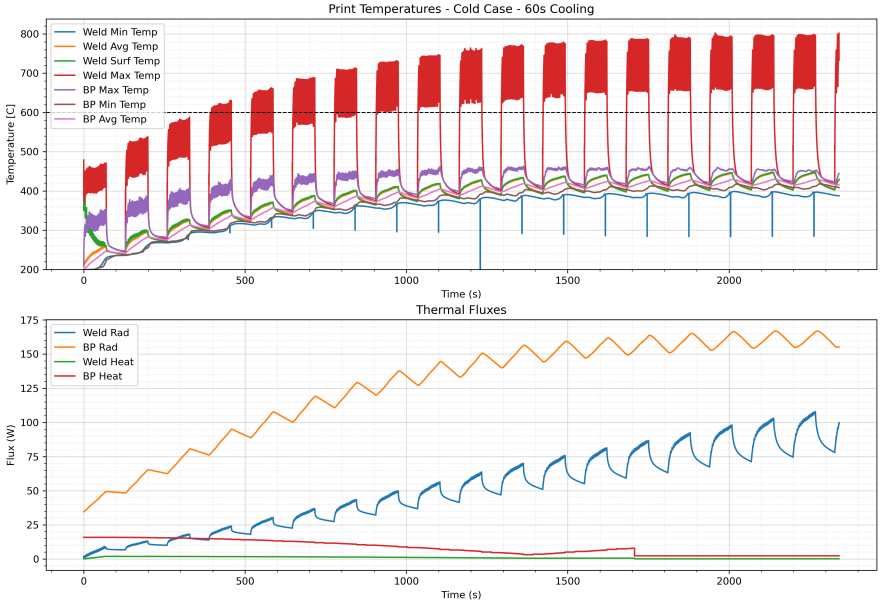


Figure C.11: Full orbit simulation results for the cold case with 60 seconds of cooling

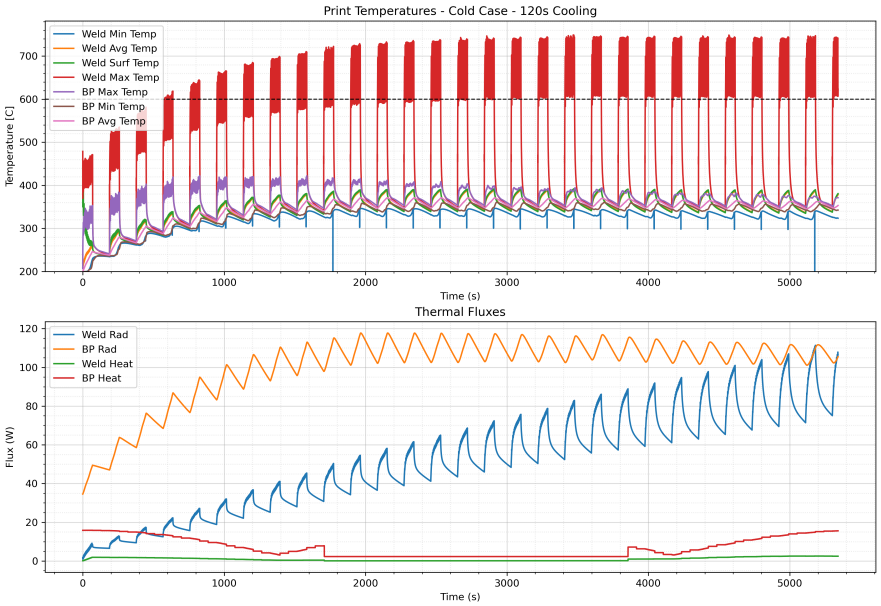


Figure C.12: Full orbit simulation results for the cold case with 120 seconds of cooling

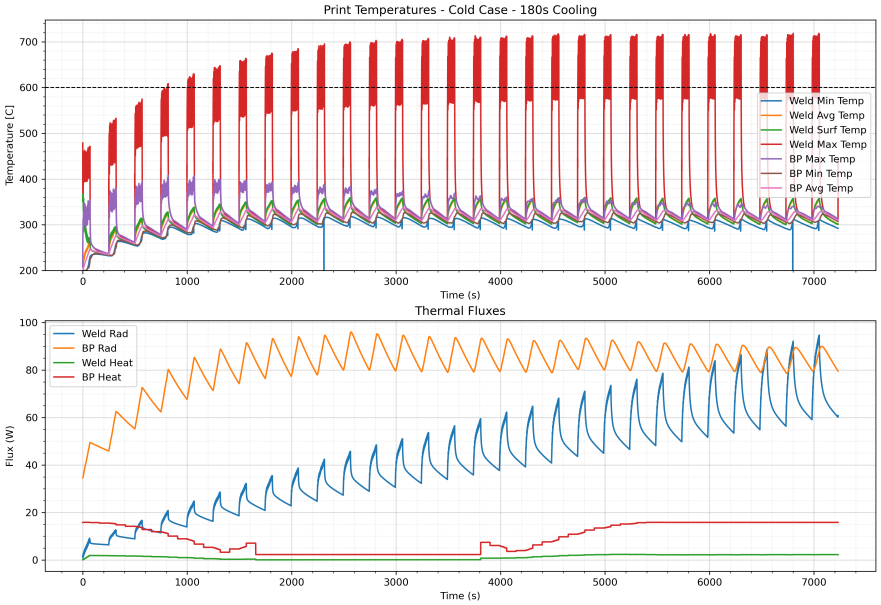


Figure C.13: Full orbit simulation results for the cold case with 180 seconds of cooling

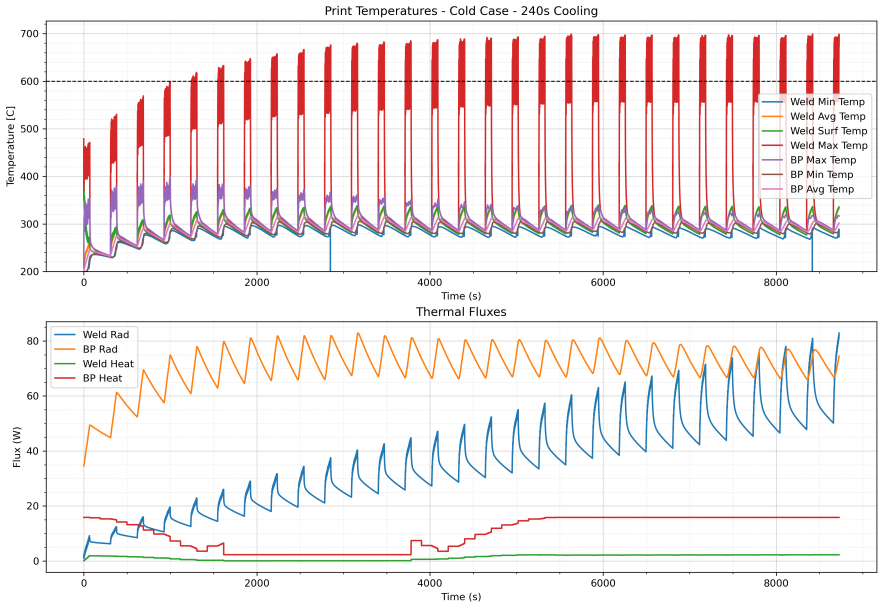


Figure C.14: Full orbit simulation results for the cold case with 240 seconds of cooling

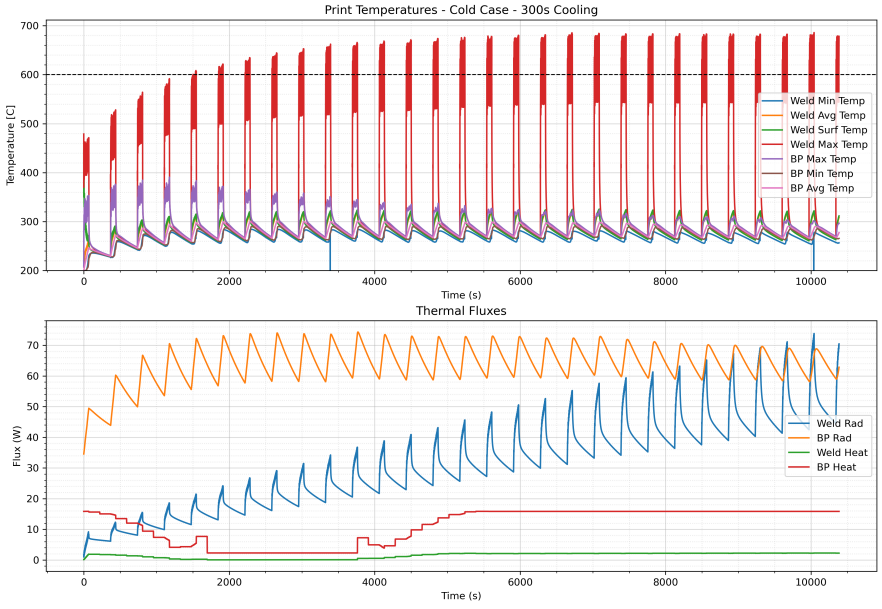


Figure C.15: Full orbit simulation results for the cold case with 300 seconds of cooling

C.2. Large Lab Simulation Results

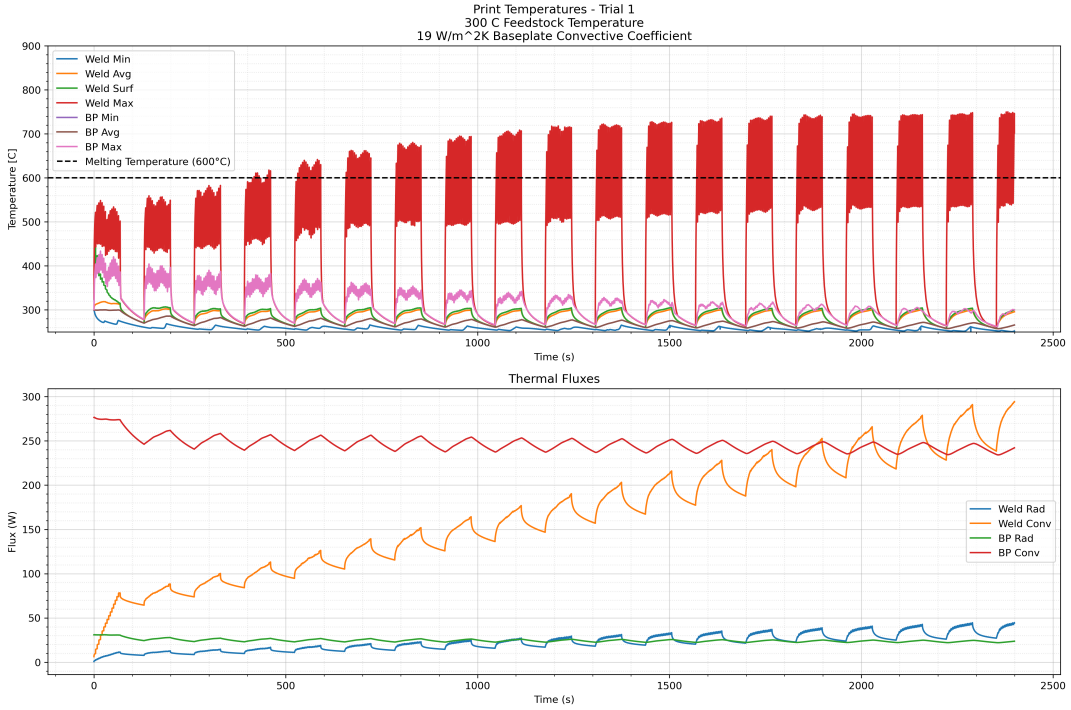


Figure C.16: Full lab simulation results for trial 1

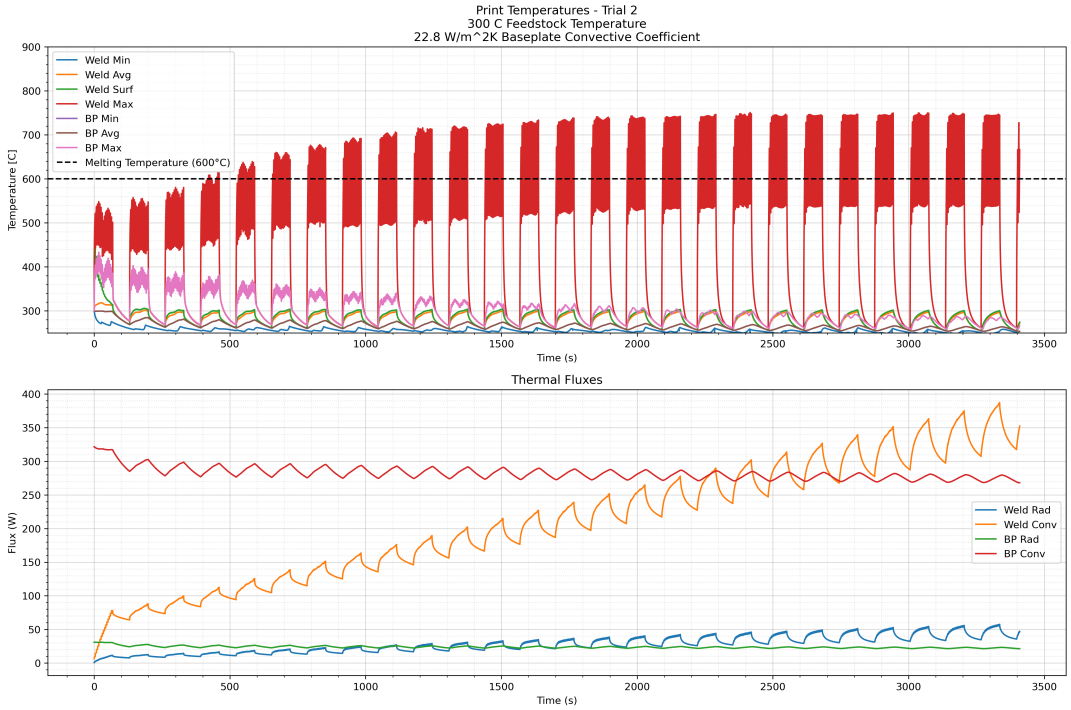


Figure C.17: Full lab simulation results for trial 2

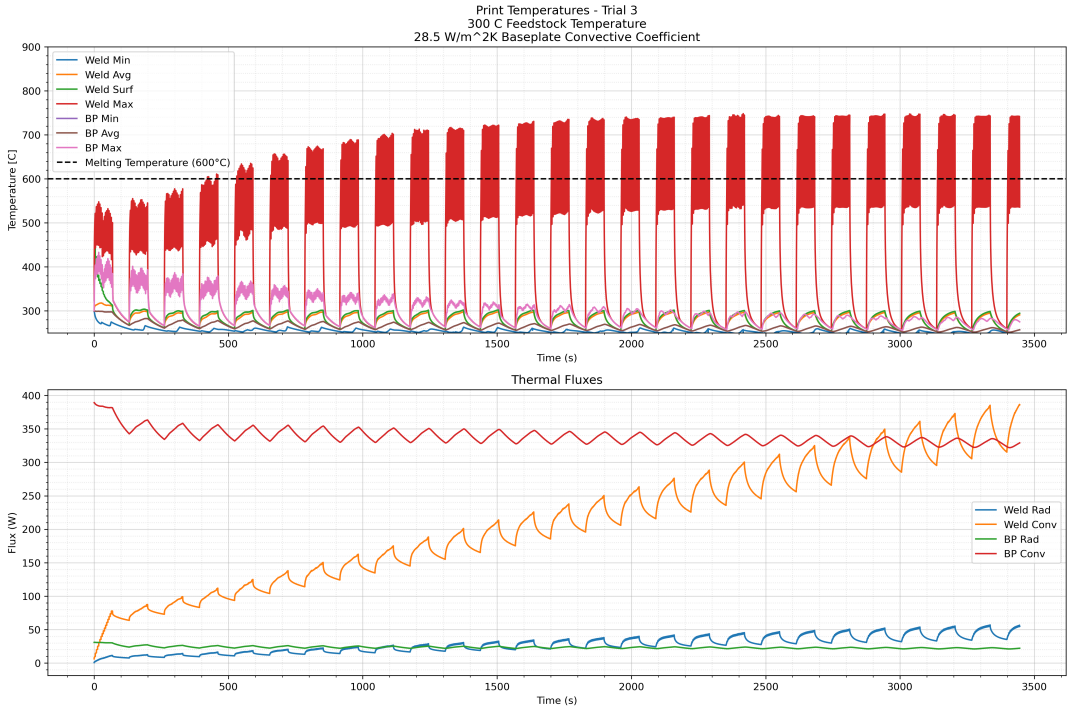


Figure C.18: Full lab simulation results for trial 3

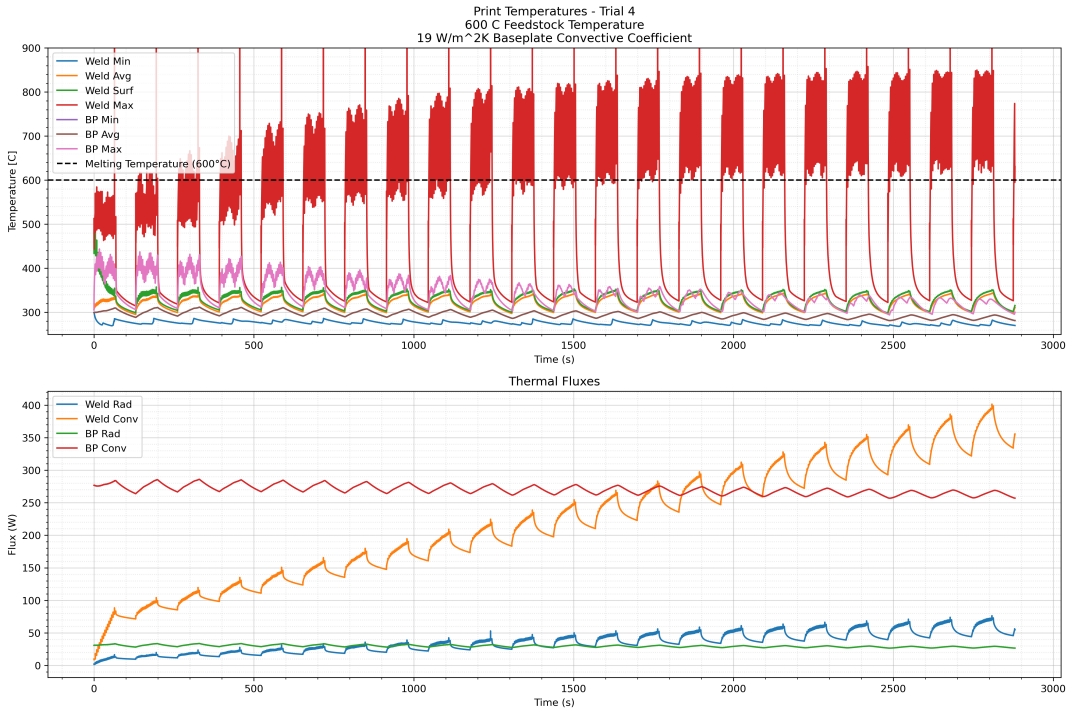


Figure C.19: Full lab simulation results for trial 4

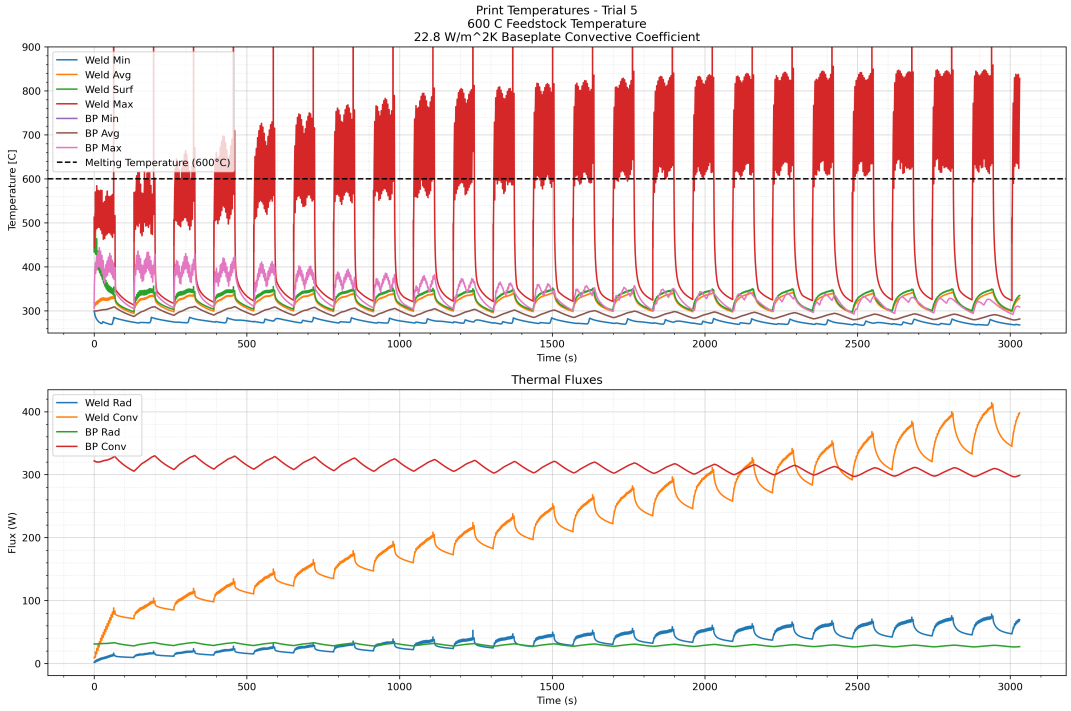


Figure C.20: Full lab simulation results for trial 5

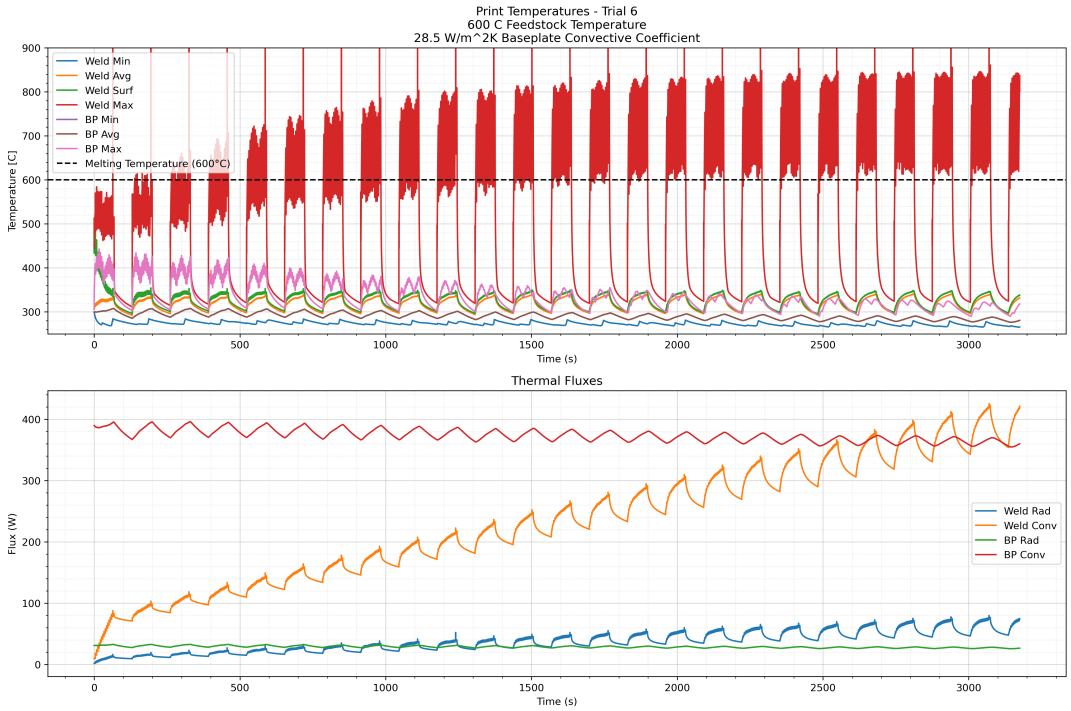


Figure C.21: Full lab simulation results for trial 6